

ELECTROMAGNETICALLY INDUCED ALTERATION OF HYDRAULIC  
CONDUCTIVITY OF COARSE-GRAINED SOILS FOR GEOTECHNICAL  
APPLICATIONS

by

Rakesh Acharya

A thesis

submitted in partial fulfillment

of the requirements for the degree of

Master of Science in Civil Engineering

Boise State University

December 2016

© 2016

Rakesh Acharya

ALL RIGHTS RESERVED

BOISE STATE UNIVERSITY GRADUATE COLLEGE

**DEFENSE COMMITTEE AND FINAL READING APPROVALS**

of the thesis submitted by

Rakesh Acharya

Thesis Title: Electromagnetically Induced Alteration of Hydraulic Conductivity of Coarse-Grained Soils for Geotechnical Applications

Date of Final Oral Examination: 24 October 2016

The following individuals read and discussed the thesis submitted by student Rakesh Acharya, and they evaluated his presentation and response to questions during the final oral examination. They found that the student passed the final oral examination.

Arvin Farid, P.E., Ph.D. Chair, Supervisory Committee

Bhaskar Chittoori, Ph.D. Member, Supervisory Committee

Jim Browning, Ph.D. Member, Supervisory Committee

The final reading approval of the thesis was granted by Arvin Farid, Ph.D., Chair of the Supervisory Committee. The thesis was approved by the Graduate College.

## DEDICATION

This thesis is dedicated to my mother and father, Pramila Acharya and Dhruba Acharya. Their faith, belief, and endless support have instilled the importance of hard work and the value to pursue higher education.

## ACKNOWLEDGEMENTS

I would like to thank my advisor Dr. Arvin Farid for giving me an opportunity to participate in this research. His shrewd advice, insightful criticisms, and patient encouragement helped me in the writing of this thesis in numerous ways. I would also like to thank Dr. Jim Browning and Dr. Bhaskar Chittoori for their participation as members in the thesis supervisory committee. Special thanks to Pam Aishlin (Research Scientist, Department of Geosciences) for her help in providing equipment for pore-pressure measurement.

## ABSTRACT

Electromagnetic (EM) waves of various power levels and frequencies can be used to alter the hydraulic conductivity of soil with minimal heat generation. The result can lead to a number of potential applications such as contamination remediation and liquefaction mitigation. In this research, the possibility of radio-frequency (RF) waves' effect on the excess pore-water pressure (EPWP) generation and hydraulic conductivity of coarse-grained soils has been investigated.

Impact tests were performed on glass beads to examine the effect on the generation of EPWP due to RF waves. These tests were performed on a rigid box made of Plexiglas. The impacts were produced by shaking the box with periodic impacts, and the generated EPWP was measured using a pore-water pressure (PWP) transducer. A loop antenna was installed inside the specimen to launch RF-waves. The RF-stimulated impact tests were performed at a constant frequency of 498 MHz and input power levels of 10, 25, 40, and 50 Watts. There were no noticeable changes observed in the EPWP generation within the glass-bead sample due to the application of RF waves.

In order to better understand the above-mentioned potential of using RF waves to mitigate liquefaction, a different set of experiments, hydraulic-conductivity measurements, were performed on two types of samples: (i) glass beads and (ii) natural sand. These tests were conducted using a customized, rigid-wall, cylindrical permeameter placed inside a box made of Plexiglas. Constant-head (D2434, ASTM, 2010) tests were performed to measure the hydraulic conductivity of these samples. The soil samples were

placed within a cavity made of Plexiglas covered with transparent conductive film (resonant cavity). A chlorinated polyvinyl chloride (CPVC)-cased monopole antenna sharing the same electric ground as that of the cavity was placed within the soil sample at its center and used to launch RF waves. Various sets of tests were conducted to evaluate the effect of the power of RF waves on the change in the hydraulic conductivity. For both samples, the tests were conducted at a constant frequency of 726 MHz and input power levels of 10, 25, and 40 Watts. The hydraulic conductivity of both natural sand and glass-bead samples increased with the RF stimulation, and the increase was larger at higher RF power. At the input power of 40 Watts, the hydraulic conductivity of glass-bead sample increased by 8.7% of the unstimulated value, whereas the increase in natural-sand sample was only measured to be 25.4%.

Measurement of the electric-field component of RF waves was performed and plotted to verify the pattern of the electric field to evaluate both the impact and the hydraulic-conductivity tests. The electric field was simulated using COMSOL Multiphysics and validated against the experimentally measured electric field. In the case of the hydraulic-conductivity tests, a finite-difference numerical model was developed in MATLAB interface to analyze the seepage flow. This numerical model was also validated against experimentally measured hydraulic conductivity. This numerical model was then used to find the spatial variation of the hydraulic head within the soil specimen.

## TABLE OF CONTENTS

DEDICATION .....	iv
ACKNOWLEDGEMENTS .....	v
ABSTRACT .....	vi
LIST OF TABLES .....	xi
LIST OF FIGURES .....	xii
CHAPTER ONE: INTRODUCTION.....	1
Motivation.....	1
Objectives .....	3
CHAPTER TWO: BACKGROUND .....	5
Hydraulic Conductivity.....	5
Constant-Head Test.....	9
Falling-Head Permeability Test .....	10
Liquefaction .....	10
Electromagnetic Waves and Propagation .....	13
Waveguides.....	15
Resonant Cavities.....	15
Possible Mechanisms of RF Stimulation .....	16
Electromagnetic Effects on Hydrogen Bonding .....	16
CHAPTER THREE: MATERIALS AND METHODS .....	17



RF Waves' Launching Setup .....	18
Loop and Monopole Antenna .....	22
Laboratory Setup, Series I.....	23
Pore-pressure Measurement.....	26
Impact Test.....	26
Saturated-Sample Preparation.....	29
Laboratory Setup, Series II .....	30
Sample Preparation .....	35
Electric-Field Mapping .....	35
Electric-Field Mapping for Impact Tests, Series I.....	37
Electric-Filed Mapping for Hydraulic-Conductivity Tests, Series II .....	38
3D Numerical Forward Model of Seepage Flow for Series-II Tests .....	39
Seepage flow .....	39
CHAPTER FOUR: RESULTS .....	46
Series 1: Impact Tests .....	46
Electric-Field Measurement and Validation of Numerical Simulation .....	53
Series 2: Hydraulic-Conductivity Tests .....	57
Electric-Field Measurement and Comparison .....	65
Seepage-Flow Numerical Simulation .....	68
CHAPTER FIVE: CONCLUSIONS .....	81
Impact Tests, Series I.....	81
Hydraulic-Conductivity Tests, Series II .....	82
Future research.....	84

REFERENCES .....	85
APPENDIX A.....	88
Simulation of Experimental Setup in COMSOL Multiphysics .....	88
Simulation of Experimental Setup in COMSOL Multiphysics .....	89
Hydraulic-Conductivity Test .....	89
APPENDIX B.....	96
M. File Written in MATLAB Interface to Numerically Calculate Hydraulic Head...	96
M. File Written in MATLAB Interface to Numerically Calculate Hydraulic Head...	97
(Unstimulated) .....	97
Natural Sand.....	97
M. File Written in MATLAB Interface to Numerically Calculate Hydraulic Head.	104
(RF-Stimulated) .....	104
Natural sand .....	104

## LIST OF TABLES

Table I.	Ranges of intrinsic permeability and hydraulic conductivity for unconsolidated sediments (Fetter, 2001) .....	8
Table II.	Properties of glass beads (Najafi, 2014) .....	29
Table III.	$\Delta$ PWP for three different tests at various RF-power levels .....	51
Table IV.	Initial effective stress and excess pore-pressure ratio .....	52
Table V.	Hydraulic-conductivity measurements of glass-bead sample at a frequency of 726 MHz and different RF-power levels .....	60
Table VI.	Hydraulic-conductivity measurements of natural-sand sample at a frequency of 726 MHz and different RF-power levels .....	64
Table VII.	Experimentally measured and numerically computed flow discharge in the natural sand at various RF-power levels .....	73
Table A.2	<i>Dielectric Properties</i> .....	93

## LIST OF FIGURES

Figure 1.	Horizontal pipe filled with sand to demonstrate Darcy's experiment (Fetter, 2001).....	6
Figure 2.	Schematic of a constant-head test (Das, 1982) .....	10
Figure 3.	Schematic of behavior of a saturated-soil specimen during earthquake...	12
Figure 4.	Cross section of a waveguide with long dimension, a, and short dimension, b.....	15
Figure 5.	Outline of methodology .....	18
Figure 6.	Schematic of impedance-matching network.....	20
Figure 7.	Variable capacitors in the matching network.....	20
Figure 8.	Schematic of the setup used for launching RF waves into the DUT .....	21
Figure 9.	Loop and monopole antenna.....	23
Figure 10.	RF-launching setup .....	23
Figure 11.	Schematic of the impact-test box with dimension .....	24
Figure 12.	Schematic of the impact-test box with saturated specimen, loop antenna, and wire mesh covering PWP transducer .....	25
Figure 13.	Pore-pressure transducer, CS451, and data-acquisition device, CR800...	26
Figure 14.	Schematic of the laboratory setup for impact tests on the box filled with saturated specimen of glass beads.....	28
Figure 15.	Setup for RF-stimulated impact tests .....	28
Figure 16.	Grain-Size distribution chart of natural sand .....	30
Figure 17.	Schematic of the RF-stimulated hydraulic conductivity tests.....	31
Figure 18.	Setup for RF-stimulated hydraulic-conductivity tests .....	32

Figure 19.	Schematic of customized, rigid-wall, cylindrical permeameter designed to conduct RF-stimulated hydraulic-conductivity tests on Sand (Azad, 2013) .....	34
Figure 20.	Schematic of the top view of the resonant cavity showing the location of depth slices for the impact test, Series I.....	38
Figure 21.	Schematic of top view of the customized permeameter showing the location of the depth slices for hydraulic-conductivity tests, Series II.....	39
Figure 22.	Schematic of (a) top view of the discretized rectangular cubical domain with circular cross section of the specimen, (b) 3D view of the rectangular cubical domain and cylindrical region within the sample. ....	42
Figure 23.	Pore-water pressure head (cm) versus time (sec.) in glass-bead sample during unstimulated impact tests. ....	48
Figure 24.	Pore-water pressure head (cm) versus time (sec.) in glass-bead sample during RF-stimulated impact tests (vertical dashed line: time of RF stimulation) at frequency of 498 MHz and power level of: a) 10 Watts; and b) 25 Watts .....	49
Fig 24 (Contd.).	Pore-water pressure head (cm) versus time (sec.) in glass-bead sample during RF-stimulated impact tests (vertical dashed line: time of RF stimulation) at frequency of 498 MHz and power level of: c) 40 Watts; and d) 50 Watts .....	50
Figure 25.	Mean EPWP at various RF-power inputs at the RF frequency of 498 MHz .....	51
Figure 26.	Mean generated EPWP at different RF frequencies (RF-power input into the resonant cavity= 40 Watts) .....	53
Figure 27.	Schematic of the location of depth of (vertical) slices in 3-D view.....	54
Figure 28.	Electric field: experimentally measured (right) and numerically simulated using COMSOL Multiphysics (left) at 498 MHz on within glass-bead sample: a) Depth Slice1; and b) Depth Slice 2 .....	55
Figure 28 (Contd.).	Electric field: experimentally measured (right) and numerically simulated using COMSOL Multiphysics (left) at frequency 632 MHz within glass-bead sample: c) Depth Slice 1; and d) Depth Slice2 .....	56
Figure 29.	Measured unstimulated hydraulic conductivity of glass-bead sample .....	58

Figure 30.	Measured RF-stimulated hydraulic conductivity of glass-bead sample at a frequency of 726 MHz and RF-power levels of: a) 10 Watts; and b) 25 Watts .....	59
Figure 30 (Contd.).	Measured RF-stimulated hydraulic conductivity of glass-bead sample at a frequency of 726 MHz and RF-power level of c) 40 Watts ..	60
Figure 31.	Measured unstimulated hydraulic conductivity of natural-sand sample...	62
Figure 32.	Measured RF-stimulated hydraulic conductivity of natural-sand sample at a frequency of 726MHz and RF-power levels of: a) 10 Watts .....	62
Figure 32 (Contd.).	Measured RF-stimulated hydraulic conductivity of natural-sand sample at a frequency of 726MHz and RF-power levels of: b) 25 Watts; and c) 40 Watts .....	63
Figure 33.	Schematic of the location of Slices 1 and 2 in 3D view .....	65
Figure 34.	Electric field, experimentally measured (right) and numerically simulated using COMSOL Multiphysics (left) within glass bead sample on: a) Depth Slice 1, frequency = 710 MHz; b) Depth Slice 2, frequency = 710 MHz	66
Figure 34(Contd.).	Electric field, experimentally measured (right) and numerically simulated using COMSOL Multiphysics (left) within glass bead sample on: c) Depth Slice 1, frequency = 726 MHz; d) Depth Slice2, frequency = 726 MHz .....	67
Figure 35.	Schematic of top-view of the discretized rectangular cubical domain .....	69
Figure 36.	Contour/color maps of hydraulic head (m) within natural-sand specimen for unstimulated flow on depth slices: a) 1 and 15, and 2 and 14; b) 3 and 13, and 4 and 12 .....	70
Figure 36 (Contd.).	Contour/color maps of hydraulic head (m) within natural-sand specimen for unstimulated flow on depth slices: c) 5 and 11, and 6 and 10; d) 7 and 9, and Slice 8.....	71
Figure 37.	Velocity vector plot within natural-sand specimen on Slice 7 for unstimulated test .....	72
Figure 38.	RF power vs RF-stimulated flow rate in the natural-sand specimen at a frequency of 726 MHz .....	74
Figure 39.	Contour/color maps of hydraulic head (m) for natural-sand specimen on depth slices: a) 1 and 15, and 2 and 14, at a frequency of 726 MHz and	

	RF-power level of 25 Watts; b) 3 and 13, and 4 and 12, at a frequency of 726 MHz and RF-power level of 25 Watts. ....	75
Figure 39 (Contd.).	Contour/color maps of hydraulic head (m) within the natural-sand specimen on depth slices: c) 5 and 11, and 6 and 10, at a frequency of 726 MHz and RF-power level of 25 Watts; d) 7 and 9, and 8, at a frequency of 726 MHz and RF-power level of 25 Watts. ....	76
Figure 40.	Vector plot for the numerically simulated RF-stimulated flow velocity within the natural-sand specimen on Slice 7 at a frequency of 726 MHz and power level of 25 Watts. ....	77
Figure 41.	Contour/color maps of normalized vertical component of numerically simulated RF-stimulated flow velocity within the natural-sand specimen on Slice 7 at a frequency of 726 MHz and power level of 25 Watts. ....	78
Figure 42.	Contour/color map of normalized difference between RF-stimulated hydraulic conductivity computed and unstimulated hydraulic conductivity within the natural-sand specimen along the vertical direction (Z direction) on Slice 7 at a frequency of 726 MHz and power level of 25 Watts. ....	79
Figure 43.	Contour/color map of normalized power density within the natural-sand specimen along the vertical direction (Z direction) on Slice 7 at a frequency of 726 MHz and power level of 25 Watts. ....	80
Figure A.1.	Schematic of the experimental setup .....	90

## CHAPTER ONE: INTRODUCTION

### **Motivation**

This research is aimed at addressing a geohazard – liquefaction. Liquefaction has been the cause of loss of lives and properties around the world. Liquefaction of loose noncohesive soils has been observed in many cases, causing extraordinary amounts of destruction. Earthquakes, such as 1964 Nigata, Japan (Kramer, 1996), 1999 Adapazari, Turkey (Martin et al., 2004), and 2011 Christchurch, New Zealand (Cole et al., 2012) are few examples of this geohazard. The research is focused on whether liquefaction can be mitigated using the application of radio-frequency (RF) waves.

Liquefaction is a result of a sudden increase in the excess pore-water pressure (EPWP) in loose, water-saturated noncohesive soils during earthquakes. This results in a reduction of the effective stress and a decrease in the contact force among soil grains. This phenomenon leads to the loss of the bearing capacity of foundations, differential settlement of foundations, slope instability, and lateral spreading of the surface soil. Liquefaction is responsible for significant damage to infrastructures and lives.

Researches on soils susceptible to liquefaction, such as sand and silty sand, show that liquefaction depends upon parameters such as peak ground acceleration, groundwater level, soils' grain size, relative density, cyclic shear strength (measured using SPT, standard-penetration tests and CPT, cone-penetration tests), soil's plasticity, and degree of water saturation (Kramer, 1996). All of these parameters are, however, linked to the phenomenon of water dissipation rate. The inability of fluid to dissipate from the soil



medium, within a short period of time during earthquakes, is the reason behind the quick buildup of EPWP, leading to liquefaction. On the other hand, the permeability of soil, when all properties of soil remain constant, depends upon fluid properties. The permeability of soils is different to fluid of different viscosities. Using a viscous fluid ( $k = 0.0021$  cm/s) and water ( $k = 0.105$  cm/s) in a centrifuge test, Sharp et al. (2003) have successfully demonstrated a smaller thickness of the liquefied layer and settlement in the case of water than viscous fluid. The study carried out by Ganainy et al. (2012) obtained a lower EPWP ratio ( $r_u$ ), which is the ratio between the excess pore-water pressure and initial effective stress. There also was a smaller thickness of liquefied soil and shear strain when the tests were conducted using water than the ones that were conducted using more viscous fluids (hydraulic conductivity 25 times lower than water).

Furthermore, electrostatic sources can align individual water molecules, and magnetic fields can float droplets of water (Ikezoe et al., 1998). This means water dipoles oscillate in the alternating electric-field component of electromagnetic (EM) fields. The vibration of these water molecules enhances different transport mechanisms inside the soil and, hence, can alter the hydraulic conductivity.

In a study conducted by Azad et al. (2014), radio-frequency (RF) waves were used to alter the hydraulic conductivity of soil. Soils with different fines content respond differently to the effect caused by the application of electromagnetic waves. In sandy soils, the hydraulic conductivity of the soil increased as much as 14% when RF waves excited natural sand at a frequency of 153 MHz with an RF-power input of 20 Watts. The increase in the hydraulic conductivity of sandy soils can be justified by the RF energy

absorbed by water molecules, which decreases the water viscosity, in turn, increasing the hydraulic conductivity.

The effect of permeability to water (otherwise known as hydraulic conductivity) on liquefaction leads to a hypothesis that the susceptibility of soil to liquefaction can be reduced using electromagnetic waves. However, this will be useful only if the effect can be initiated fast enough. Regardless of the speed of the increase in the hydraulic conductivity using EM waves, the effect of EM waves on the hydraulic conductivity of soils needs to be studied.

Unlike the results from Sharp et al. (2003) where the fluid viscosity was altered as much as 50 times and those by Ganainy et al. (2012) where the permeating fluid's viscosity was changed by 25 times, the result from Azad et al. (2014) showed that the alteration of the hydraulic conductivity by RF waves is comparatively small. However, no further study on the alteration of the hydraulic conductivity at various RF frequencies and power levels was carried out. Further understanding of the effect of RF waves on hydraulic conductivity can lead to a number of potential applications such as liquefaction mitigation and contamination remediation. Hence, a more thorough understanding is necessary.

### **Objectives**

As mentioned, the main aim of this research is to evaluate the effect of RF waves on the hydraulic conductivity of sandy soils. RF waves were launched into a permeameter to inspect any change in the hydraulic conductivity. The secondary objective is to evaluate whether this change can be sufficiently large and fast to reduce the EPWP generation during earthquakes to mitigate liquefaction. During earthquakes, EPWP is

generated within fine sands or silty sands due to low dissipation rate. A reduction of even a small amount in the generated EPWP can prevent soil from liquefying. The main objective of this research is to understand the effect of RF waves at varying power levels and frequencies on the hydraulic conductivity of noncohesive soils. Another objective of this research is to measure the increase in the EPWP within noncohesive soils during unstimulated and RF-stimulated tests performed at different RF waves' frequencies and power levels.

## CHAPTER TWO: BACKGROUND

Before evaluating the effects of radio-frequency (RF) fields on hydraulic conductivity, there is a need for a description of background on hydraulic conductivity and RF waves. Moreover, a basic understanding on hydraulic conductivity's effects on the generation of EPWP and its dissipation as well as liquefaction is necessary. These topics are covered and discussed in this chapter.

### Hydraulic Conductivity

Soils allow seepage of water through their voids that form interconnected paths. The seepage flow and its velocity are measured by and depend on a parameter called hydraulic conductivity. Water flows through soil from one point to another when there is a difference in the total head (also known as hydraulic head). For a given soil, the flow velocity is proportional to the total-head difference and inversely proportional to the length of the flow path. This proportionality can be converted into an equality referred to as Darcy's law using a constant called hydraulic conductivity. Darcy experimentally found that for the flow from Point A to Point B,

$$Q \propto (h_B - h_A) \text{ and } Q \propto 1/L \quad (1)$$

$$Q = -kA (h_B - h_A)/L \quad (2)$$

where:  $Q$  = discharge ( $\text{m}^3/\text{s}$ ),  $h$  = total (hydraulic) head (m),  $L$  = flow-path length (m), and  $k$  = hydraulic conductivity of soil (m/s). Equation 2 is known as Darcy's law.

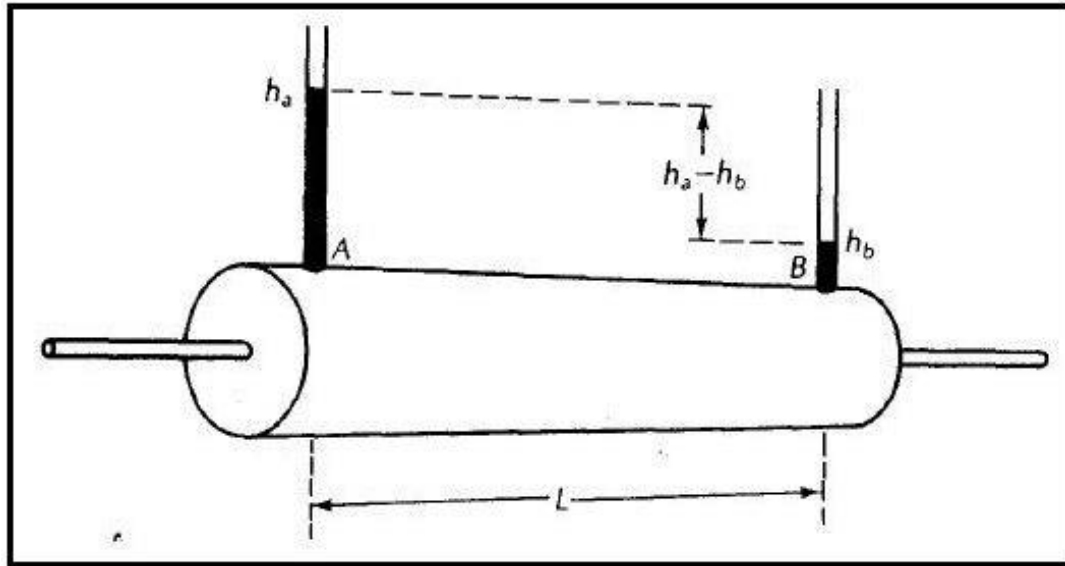


**Figure 1. Horizontal pipe filled with sand to demonstrate Darcy's experiment (Fetter, 2001)**

Total head as shown in Equation 3 is the total energy per unit weight of water at a point. From Bernoulli's equation,

$$h = h_e + h_p + h_v = z + \frac{P}{\rho g} + \frac{v^2}{2g} \quad (3)$$

where:  $h$  = total head (m);  $h_e$  = elevation head (m);  $h_p$  = pressure head (m);  $h_v$  = velocity head (m);  $z$  = elevation with respect to a datum (m);  $P$  = pore-water pressure (Pa);  $v$  = flow velocity (m/s); and  $\rho$  = density of water ( $\text{kg/m}^3$ ).

In most soil media, the flow is laminar. The flow velocity is very slow, and the velocity head is hence negligible. Therefore, the total head of water can be simplified as the sum of only elevation head and pressure head as follows:

$$h = h_e + h_p = z + \frac{P}{\rho g} \quad (4)$$

Equation 2 can also be expressed as follows:

$$Q = -kA \frac{dh}{dl} \quad (5)$$

$$v = -k \frac{dh}{dl} \quad (6)$$

where:  $\frac{dh}{dl}$  is the hydraulic gradient, and  $v$  is called discharge (also Darcy's) velocity (m/s). The negative sign indicates that the water flows from the higher total head towards the lower total head. The flow velocity, also known as the flow rate or specific discharge,  $v$ , is the amount of discharge per unit area. As seen in Darcy's law, Equations 2, 5, or 6, the flow rate is dependent upon the hydraulic conductivity ( $k$ ) of soil. This connects to the premise that the dissipation of excess pore-water pressure generated by a variety of sources such as earthquake will be faster in soils with a higher hydraulic conductivity.

Darcy's law is applicable in soil where the resistive force of viscosity is predominating. Slow-moving fluids are under viscous force, which leads to the flow being laminar. However, if the velocity of the flow is high, then the kinetic energy will overcome the viscous force and the flow will no longer be laminar. Hence, in those cases, Darcy's law is not valid. Reynold's number is a parameter that helps to determine whether the flow is laminar or turbulent (Hornberger, 1998). The flow is laminar if the Reynold's number is between 1 and 10 (Fetter, 2001). Reynold's number is defined as follows:

$$R = \rho v d / \mu \quad (7)$$

where:  $R$  is the Reynold number;  $\rho$  is the fluid density in  $\text{kg/m}^3$ ;  $v$  is the discharge velocity in m/s;  $d$  is the diameter of the passageway in m; and  $\mu$  is the viscosity in  $\text{kg/m}\cdot\text{s}$ .

Moreover, the hydraulic conductivity of soils is a function of the property of both the porous medium and fluid (unit weight and viscosity) (Hubbert, 1957). The discharge is directly proportional to the unit weight of the fluid and inversely proportional to the dynamic viscosity of the fluid, where the latter is a measure of the resistance of the fluid

to the flow (Fetter, 2001). Another commonly used term is the intrinsic permeability of a soil ( $K$ ), which is a permeability of the porous medium regardless of the permeant fluid. Intrinsic permeability is a property of the soil through which the fluid passes. Intrinsic permeability of a medium depends upon the shape of openings and the mean-pore diameter (Fetter, 2001). Intrinsic permeability and hydraulic conductivity of a soil can be correlated as follows.

$$k = \frac{K\gamma}{\mu} = \frac{K\gamma}{\mu} = \frac{Kg}{\nu} \quad (8)$$

where:  $k$  = permeability to a permeant fluid , e.g., permeability to water also known as hydraulic conductivity, in m/s;  $K$  = Intrinsic permeability of the medium, in  $m^2$ ;  $g$  = acceleration due to gravity, in  $m/s^2$ ;  $\gamma$  = unit weight of permeant, e.g., water, in  $N/m^3$ ;  $\mu$  = absolute or dynamic viscosity of water, in Pa-s;  $\nu = \mu / \rho =$  kinematic viscosity of water, in St. (Stokes =  $m^2/s$ ); and  $\rho$  = density of water, in  $kg/m^3$ .

Typical values of the intrinsic permeability and hydraulic conductivity of different soils are presented in Table I.

**Table I. Ranges of intrinsic permeability and hydraulic conductivity for unconsolidated sediments (Fetter, 2001)**

Material	Intrinsic Permeability	Hydraulic Conductivity (cm/s)
Clay	$10^{-6} - 10^{-3}$	$10^{-9} - 10^{-6}$
Silt, sandy silts, clayey sands, till	$10^{-3} - 10^{-1}$	$10^{-6} - 10^{-4}$
Silty sand, fine sand	$10^{-2} - 1$	$10^{-5} - 10^{-3}$
Well-sorted sands, glacial outwash	$1 - 10^2$	$10^{-3} - 10^{-1}$
Well-sorted gravel	$10 - 10^3$	$10^{-2} - 1$

Laboratory methods to measure hydraulic conductivity need preparation of samples. These tests can be run in the lab following the guidelines set by standards such as those set by the American Society for Testing and Materials. Laboratory methods to determine hydraulic conductivity are divided as: constant-head method and falling-head method. In this study, constant-head method is used to measure hydraulic conductivity.

#### Constant-Head Test

This method is suitable to measure the hydraulic conductivity of coarse-grained soils where the flow rate of water is high and a constant head can be maintained by a continued supply of water. Flow of water is allowed under a known constant head. At first, flow water is allowed for 10 minutes to saturate the specimen and reach a steady state. Once the flow is steady, the volume of water is collected over a period of time, and the rate of flow is determined. According to ASTM D2434 (ASTM, 2006), hydraulic conductivity of a soil sample having a length  $L$  and a cross-sectional area  $A$  can be obtained using the following equation.

$$k = \frac{V}{t} \times \frac{L}{Ah} \quad (9)$$

where:  $h$  = hydraulic-head loss across the soil medium (m),  $A$  = cross-sectional area of soil specimen ( $m^2$ ),  $L$  = length of the soil specimen (m),  $t$  = time of water collection (s), and  $V$  = volume of water collected ( $m^3$ ). Figure 2 shows the schematic of a constant-head test. As seen in Figure 2, the difference between the total heads of the top and bottom of



the specimen,  $\Delta H$ , is maintained constant.

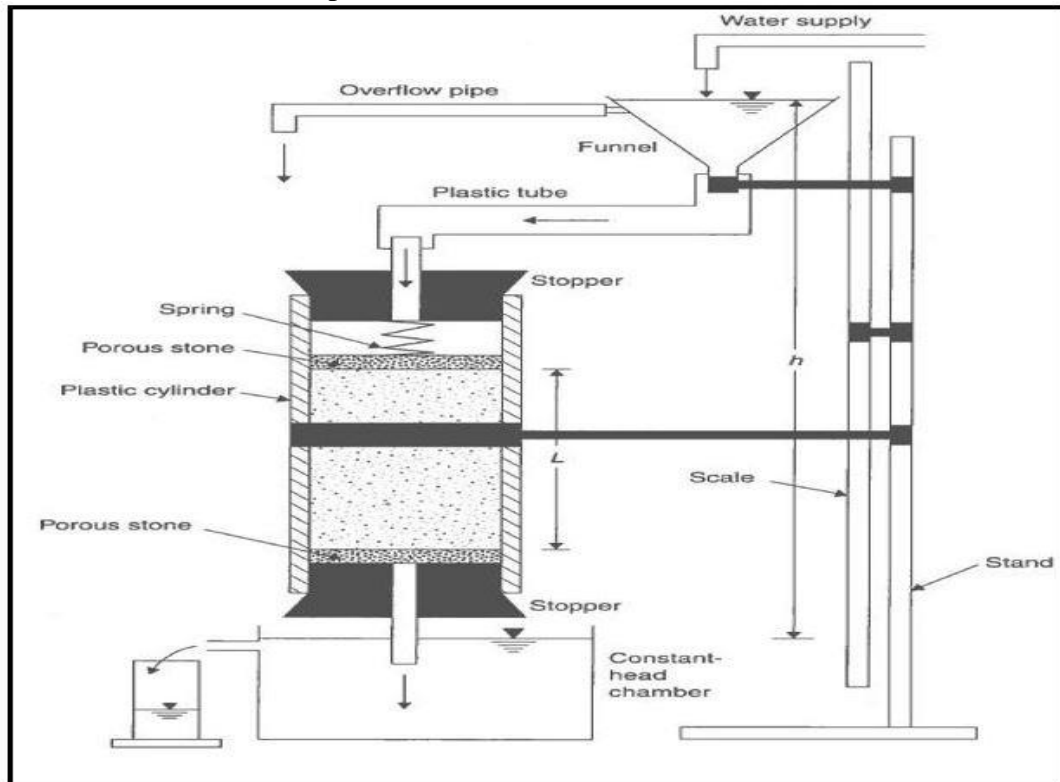


**Figure 2. Schematic of a constant-head test (Das, 1982)**

### Falling-Head Permeability Test

Falling-head test can be performed both on fine-grained and coarse-grained soils. The soil sample is first saturated by allowing water to flow for 10 minutes. As water flows, the total head of input water declines because there is no supply of water to maintain the input head. The test is performed following the guidelines of ASTM D5084 (ASTM, 2006), and the hydraulic conductivity is calculated. Because the samples used in this research are glass bead and natural sand, a falling-head test is not necessary.

### **Liquefaction**

Liquefaction is a phenomenon that occurs when the stiffness of saturated loose soils decreases with a prompt increase in the pore-water pressure (PWP,  $u$ )—referred to as excess pore-water pressure (EPWP,  $u_e$ )—due to a rapid dynamic load as that of

earthquake. A rapid loading creates an undrained condition in saturated cohesionless soils, leading to an increase in the EPWP, obviously in turn an increase in PWP, and thus a decrease in the effective stress. The phenomenon can be observed during earthquakes. Before an earthquake, the PWP ( $u$ ) is hydrostatic, and the total vertical stress ( $\sigma$ ) and, in turn, the effective vertical stress ( $\sigma' = \sigma - u$ ) are positive. With the instant addition of the earthquake load, the PWP ( $u$ ) increases rapidly, and an excess (in excess to the natural hydrostatic) PWP is generated, leading to the reduction in the effective vertical stress. The vanishing effective vertical stress leads to the loss of friction, the sole source of the shear strength in noncohesive soils such as sand. Some water has to dissipate in the wake of the increased EPWP. Within such short time period, water does not have enough time to dissipate. Thus, the decrease in the effective vertical stress and friction leads to the decrease in the shear strength (Kramer, 1996).

From Mohr's Coulomb theory,

$$\tau_f = c' + \sigma' \tan \phi' \quad (10)$$

where:  $c'$  = cohesion of soil ( $\text{N/m}^2$ );  $\tau_f$  = shear strength ( $\text{N/m}^2$ ); and  $\phi'$  = angle of internal friction.

In the case of sandy soils,  $c'$  is 0. As the effective vertical stress approaches zero, the soil loses its shear strength. Figure 3 shows the loosening of the saturated soil due to the increase in the EPWP during the earthquake.

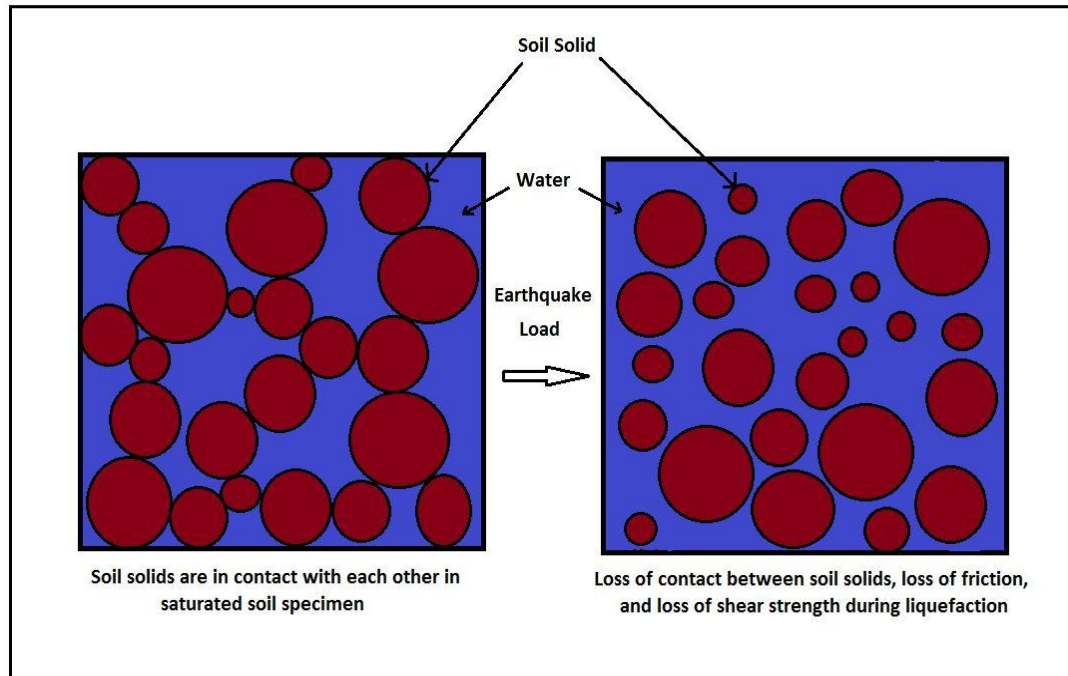


**Figure 3. Schematic of behavior of a saturated-soil specimen during earthquake**

Susceptibility to liquefaction depends upon a number of factors such as geologic and compositional properties and the state of the soil. Liquefaction has been dominant in soils that have low groundwater depth. Moreover, reclaimed lands with loose soils are prone to liquefaction (Kramer, 1996). Possibility of liquefaction depends upon the composition of the soil because a volume-change behavior influences the rise of EPWP. However, the liquefaction phenomenon is not common in all types of soils. Fine-grained soils such as clay have cohesion, which is another source of shear strength independent of friction and effective stress, and are hence less prone to liquefaction. Very coarse-grained soils, even though frictional, are highly permeable and dissipate the pore-water pressure rapidly, thus, also less prone to liquefaction. It is also incorrect that sand is the only type of soil that exhibits liquefaction phenomenon. Liquefaction of nonplastic silts has also been observed (Kramer, 1996). Nonplastic and cohesionless silts having dimensions equal in all directions (bulk shape) are prone to liquefaction (Kramer, 1996). In the case

of Adalpazari earthquake, the layer of sand containing 30% nonplastic fines and classified as silty sand (SM) was considered liquefiable under moderate levels of ground shaking (Martin et al., 2004) and liquefied in areas where soil treatment was not completed. Liquefaction of soil depends upon the gradation as well. Soils that are well-graded are less prone to any increase in the EPWP than poorly-graded or uniformly-graded soils. An increase in the pore-water pressure also depends upon the density of the soil and its initial stress condition (Kramer, 1996).

A parameter  $r_u = \Delta u / \sigma'$  has been defined to illustrate the path toward liquefaction, where  $r_u$  = EPWP ratio;  $\sigma'$  = initial effective stress; and  $\Delta u = u_e$  = EPWP increase during earthquake.

When  $r_u = 1$ , liquefaction occurs; and when  $r_u = 0.25$  to  $0.70$ , partial liquefaction occurs (Ganainy et al., 2012).

The EPWP generation has a significant effect on the shear strength, stability, and settlement characteristics of soil deposit, even if the soil does not completely liquefy (Hazirbaba et al., 2009.). Therefore, an even small decrease in the EPWP can reduce potential hazardous effects of liquefaction.

### **Electromagnetic Waves and Propagation**

This study is conducted to examine the relationship between soil properties (EPWP and hydraulic conductivity) and RF waves. These constraints include the power and frequency of Electromagnetic (EM) waves launched into soil medium. EM waves are formed when an electric field and a magnetic field oscillate perpendicular to each other. These orthogonal oscillations of electric and magnetic fields are governed by four equations, which can be presented in either integral or differential form. These are called

Maxwell's equations. Maxwell unified Faraday's, Ampere's, and two Gauss's laws to form a set of equations governing EM-wave propagation. There are a number of fundamental quantities involved in the Maxwell's equation. These fundamental electromagnetic quantities are the electric-field intensity,  $\vec{E}$  (V/m), electric displacement (electric-flux density),  $\vec{D}$  (C/m<sup>2</sup>), the magnetic-field intensity,  $\vec{H}$  (A/m), the magnetic-flux density,  $\vec{B}$  (Wb/m<sup>2</sup>), the current density,  $\vec{J}$  (A/m<sup>2</sup>), and the electric-charge density,  $\rho$  (C/m<sup>3</sup>) (Najafi, 2014). For general time-varying fields, Maxwell's equations can be written as follows.

$$\vec{\nabla} \times \vec{H} = \vec{J} + \frac{\partial \vec{D}}{\partial t} \quad (11)$$

$$\vec{\nabla} \times \vec{E} = -\frac{\partial \vec{B}}{\partial t} \quad (12)$$

$$\vec{\nabla} \cdot \vec{D} = \rho \quad (13)$$

$$\vec{\nabla} \cdot \vec{B} = 0 \quad (14)$$

The first two equations, Eqns. 11 and 12, are referred to as Ampere's law and Faraday's law, respectively. The third and fourth equations, Eqns. 13 and 14, are electric and magnetic forms of Gauss's law, respectively. An additional fundamental equation is the equation of continuity, which can be written as follows.

$$\vec{\nabla} \cdot \vec{J} = -\frac{\partial \rho}{\partial t} \quad (15)$$

Out of the five above-mentioned equations, Eqns. 11 through 15, only three are independent. The rest are related through continuity equations ( $\vec{D} = \epsilon \vec{E}$ ,  $\vec{B} = \mu \vec{H}$ ,  $\vec{\nabla} \times \vec{B} = \mu \vec{J}$ , where  $\epsilon$  ( $\frac{F}{m}$ ) and  $\mu$  ( $\frac{H}{m}$ ) are the dielectric permittivity and magnetic permeability of the medium, respectively). The first two equations (i.e., Eqns. 11 and 12) are combined

with either the electric form of Gauss' law or the equation of continuity to form such an independent system (Najafi, 2014).

### Waveguides

Conductive waveguides are devices made of hollow metallic tubes that transfer electromagnetic energy from one region to another. Circular and rectangular waveguides are common shapes of waveguides. Figure 4 shows the cross section of a conductive waveguide. A rectangular cavity can be formed by terminating the sending and receiving ends of the waveguide with conductive walls. A forward-moving wave will bounce back and forth from these walls, resulting in a standing-wave pattern along the Z direction.

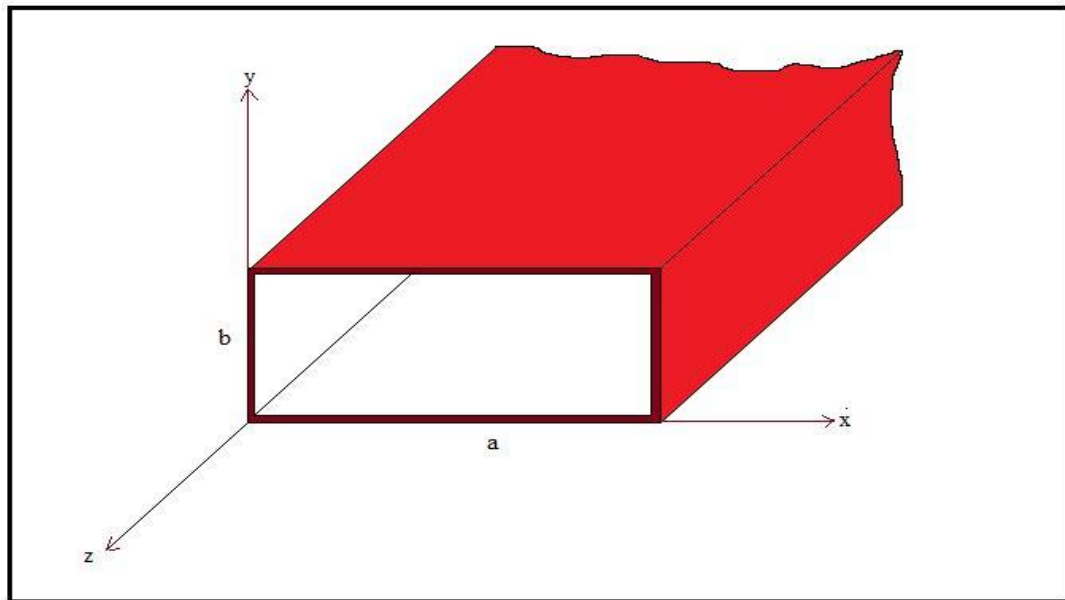


**Figure 4. Cross section of a waveguide with long dimension, a, and short dimension, b**

### Resonant Cavities

Two different sets of experiments (hydraulic-conductivity test and EPWP generation due to shaking; impact test) performed in this study require the experiments to be conducted encased in a resonant cavity. This is conducted to restrict RF waves in the

testing medium. Similar to the oscillation of acoustic energy taking place in a hallway, RF resonant cavities store electromagnetic energy. The device that exhibits this resonant phenomenon is called a resonator. Resonators oscillate at certain frequencies with greater amplitude than others. The basic parameters of an electromagnetic resonator are its resonant frequency,  $f_r$ , the type of the wave inside it, and the quality factor,  $Q$ . The resonant frequency and the type of the wave depend on the resonator shape, size, and excitation (Demarest, 2006).

An RF cavity is a special type of resonator, consisting of a closed metal structure that confines electromagnetic fields in the microwave region of the spectrum. The structure is either hollow or filled with a dielectric material. Electric and magnetic energies are stored within the cavity, and the only losses are due to the finite conductivity of the cavity walls and dielectric losses of the material filling the cavity. The boundary conditions on the cavity walls force the electric and magnetic fields to exist only at certain quantized resonant frequencies. For highly electrically conductive walls, the resonance is extremely sharp, having a very high,  $Q$ , of the order of 10,000.

### **Possible Mechanisms of RF Stimulation**

#### Electromagnetic Effects on Hydrogen Bonding

As water molecules are dipolar, electric fields change the alignment of water molecules. An electric field causes dissociation of liquid water (Bramwell, 1999). The alignment of water molecules with the electric field causes hydrogen bonding to become bent or broken (Sun et al., 2007). Broken hydrogen bonds decrease the viscosity of water. The decreased viscosity may result in an increase in the hydraulic conductivity.

### CHAPTER THREE: MATERIALS AND METHODS

To understand RF waves' effect on the EPWP generation, a series of RF-stimulated impact tests were conducted. Similarly, RF-stimulated hydraulic-conductivity tests were performed to examine the effect on hydraulic conductivity. The first series of lab experiments, i.e., Series I (impact tests), were designed to measure the EPWP generation of a glass-bead sample as soil simulant. In this work, impacts were exerted on a rigid box made of Plexiglas by a shaking mechanism using a pendulum-style impact generator, and the generated EPWP was measured using a PWP transducer. The second series of tests (Series II, hydraulic conductivity) were conducted to measure the hydraulic conductivity of two types of samples: (i) glass beads and (ii) natural sand. Constant-head (D2434, ASTM, 2006) tests were performed to measure the hydraulic conductivity of these samples. The reason behind using glass beads for the impact test and using both glass beads and natural sand for the hydraulic conductivity is explained in Chapter 4. Both of these tests were performed in the presence and absence of RF waves where the latter was used as the control. In both Series I and II, RF stimulation was implemented using similar RF-launching setups. However, in the case of Series I (impact) tests, a loop antenna was installed within the specimen to launch RF waves; whereas in the case of Series II (hydraulic-conductivity) tests, a monopole antenna was placed within the samples at their centers. The electric-field component of RF waves was measured using a vertical-monopole probe. The electric field was also numerically simulated using COMSOL Multiphysics software and validated against experimentally measured electric



fields. In the case of RF-stimulated hydraulic-conductivity study, a finite-difference numerical model was developed in MATLAB interface to analyze the seepage flow and validated against experimentally measured hydraulic conductivity and discharge. Figure 5 shows the outline of the methodology.

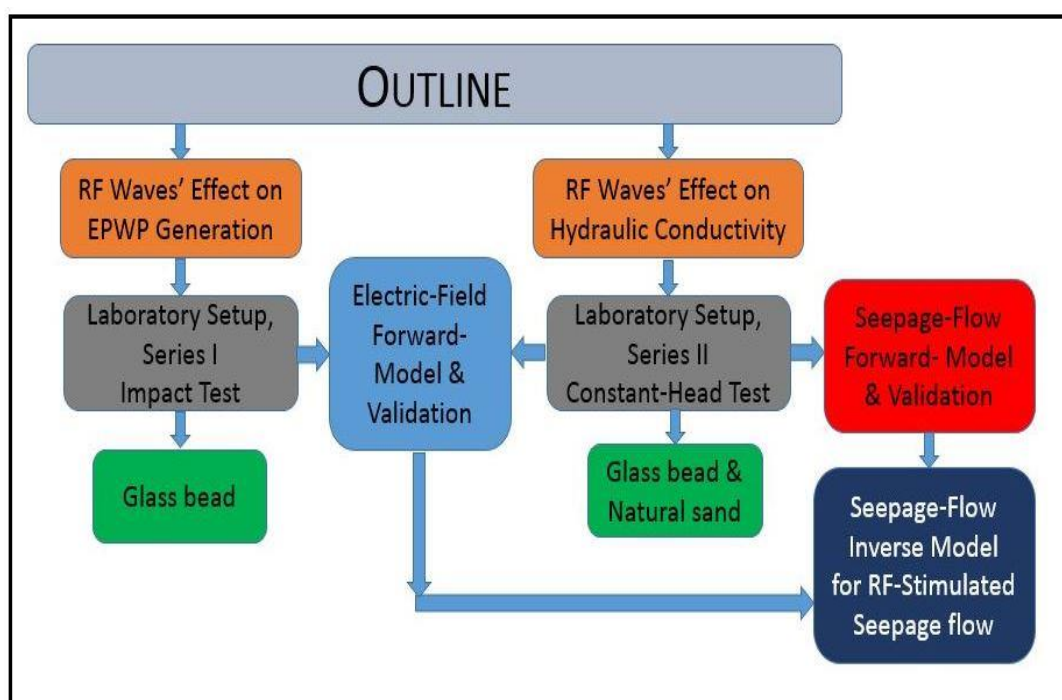


**Figure 5. Outline of methodology**

### RF Waves' Launching Setup

As mentioned in the previous section, similar RF launching setups were used for both the impact and hydraulic-conductivity tests. Therefore, before the discussion of experimental setups, some information about RF launching setups and procedures for both tests are discussed.

A signal generator is a device that generates RF signal. Amplifiers amplify a signal to the higher power that needs to be launched into the soil medium. The signal generator and amplifier in the lab have impedences of 50  $\Omega$ . The signal generator and

amplifier are termed as the source of the network. They are connected to each other by a 50Ω coaxial cable. The amplified RF signal has to be launched into the soil medium, referred to as load or DUT (device under testing). However, every other equipment except for the DUT in the network have a 50Ω impedance. When the impedance of the entire network is not 50 Ω, the signal sent by the source is reflected into the source. Therefore, the impedance of the entire network has to be matched. Hence, before launching RF waves into the DUT, the impedance of the DUT was matched using a matching network to that of the source (signal generator and amplifier, 50 Ω) in order to input the maximum power possible into the DUT and minimize the reflection of power back into the source (amplifier). To minimize the reflection back into the source, a matching network was constructed using two two-gang variable capacitors (10 pF to 500 pF) (Azad, 2012). One of the variable capacitors was connected in parallel, and another was connected in series in the network. The variable capacitors have rotating shafts to tune the capacitor and change capacitance. The change in the capacitance changes the impedance of the network. The impedance of the network was matched using trial and error while tuning the two capacitors. The impedance of the entire network should be measured while tuning capacitors. The impedance measurement was performed using an Agilent N9320A, vector network analyzer (VNA). The VNA measures the reflection coming back from the network. The impedance of the network was matched after confirming minimum reflection measured using the VNA. Figure 6 shows the setup of the impedance matching network, and Figure 7 shows the variable capacitors in the matching network.

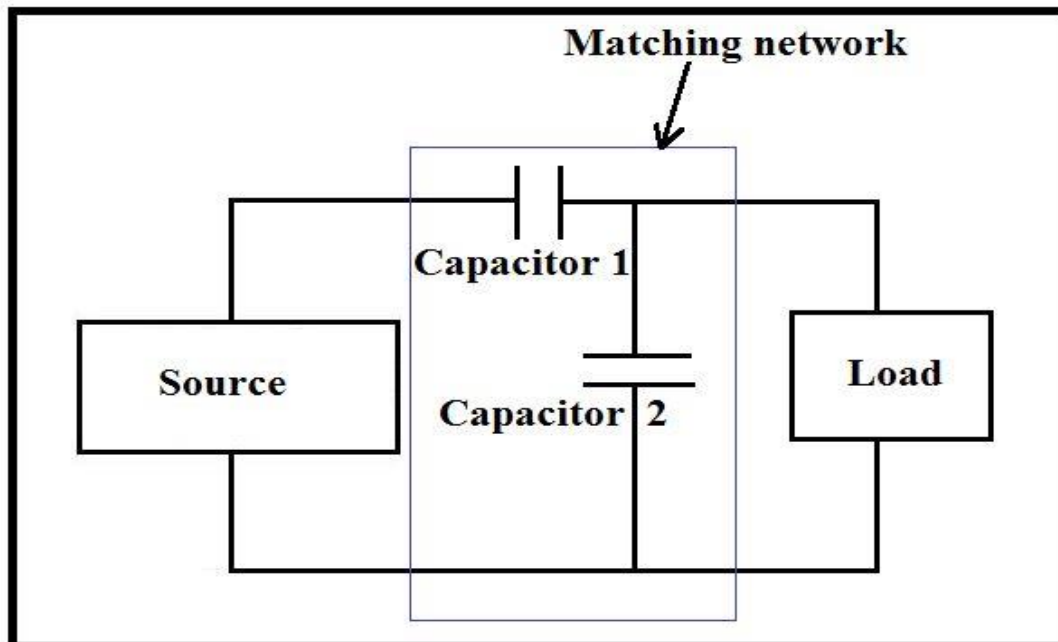


Figure 6. Schematic of impedance-matching network

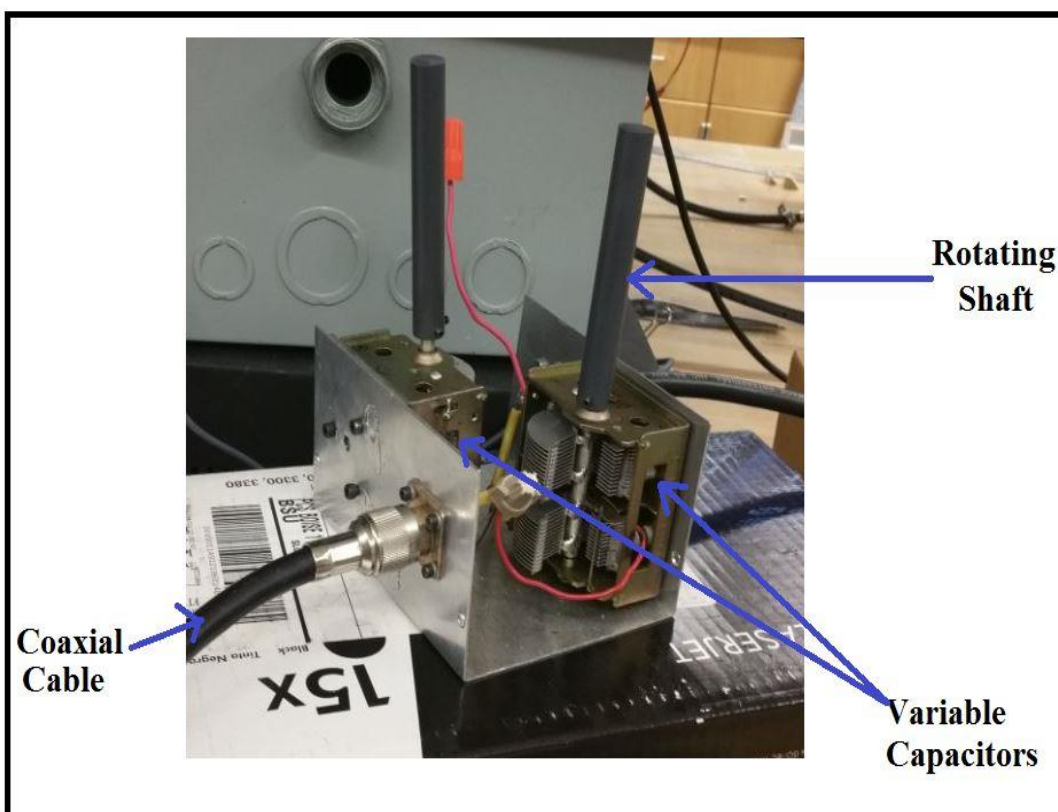
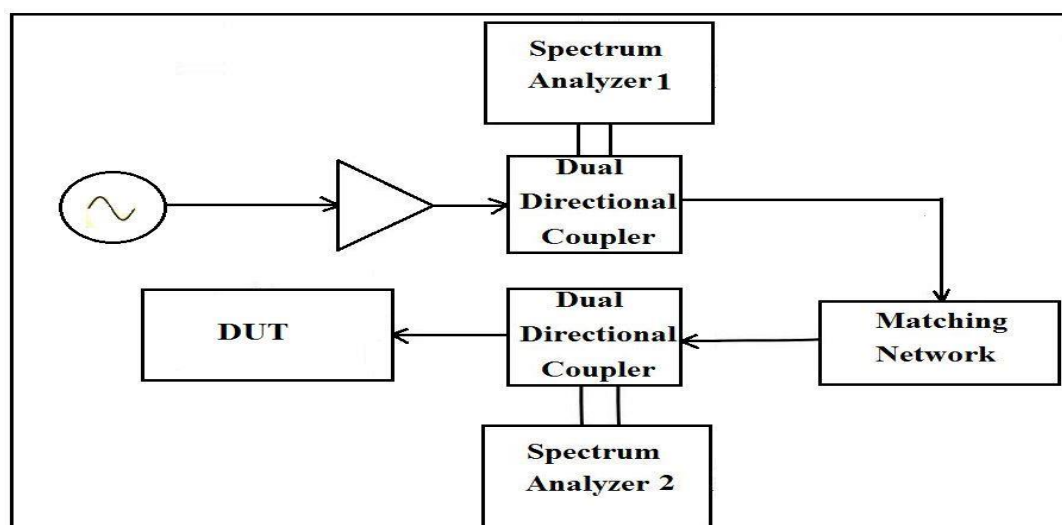


Figure 7. Variable capacitors in the matching network

After impedance matching, an Agilent Model # E4400B, signal generator was used to generate RF signals at 0 dBm. The 0dBm signal generated using the signal generator was amplified using an amplifier to a higher power than the received 0dBm signal. The amplifier helps to send signals at different power levels at the same frequency and study the effect of the RF power level and frequency. Two dual-directional couplers were used in the network. These dual directional couplers were connected to spectrum analyzer to measure the forward power into the DUT and reflected power back into the amplifier.

One of the two dual-directional couplers was used between the matching network and the amplifier, and the other one between the matching network and the load. The dual-directional couplers have two measuring ports to monitor the forward and reflected power, respectively. These two ports are connected to the spectrum analyzer with an RG8 (50 $\Omega$ ) coaxial cable. This helps to eliminate the loss of power (if any) within the network. Cables used to connect these devices were RG8 (50 $\Omega$ ) coaxial cable. Figure 8 shows the schematic of the setup used for launching RF waves into the medium.



**Figure 8.** Schematic of the setup used for launching RF waves into the DUT

### Loop and Monopole Antenna

A loop-coupled antenna made of an RG-8 coaxial cable was used to electromagnetically stimulate the DUT in Series I (impact) tests. At specific frequencies, more energy can be transferred into the cavity using loop antennae than a monopole antenna (Azad, 2012). Hence a loop antenna was used in the case of impact tests. In this case, the closed-current loop was used parallel to the magnetic lines within the cavity to excite the magnetic field.

As mentioned, the RF-launching setup for the RF-stimulated hydraulic-conductivity tests (Series II) was very similar to that of Series-I tests except for the use of a different antenna. After the Series-II setup was prepared, a monopole antenna was used to electromagnetically stimulate the DUT. The monopole antenna was made of an RG8 coaxial cable. A monopole antenna was used for Series-II tests because of the difficulty of installing a loop antenna inside the permeameter. Figure 9 shows the schematic of the monopole and loop antenna. Figure 10 shows photographic images of the apparatus used to launch RF waves.

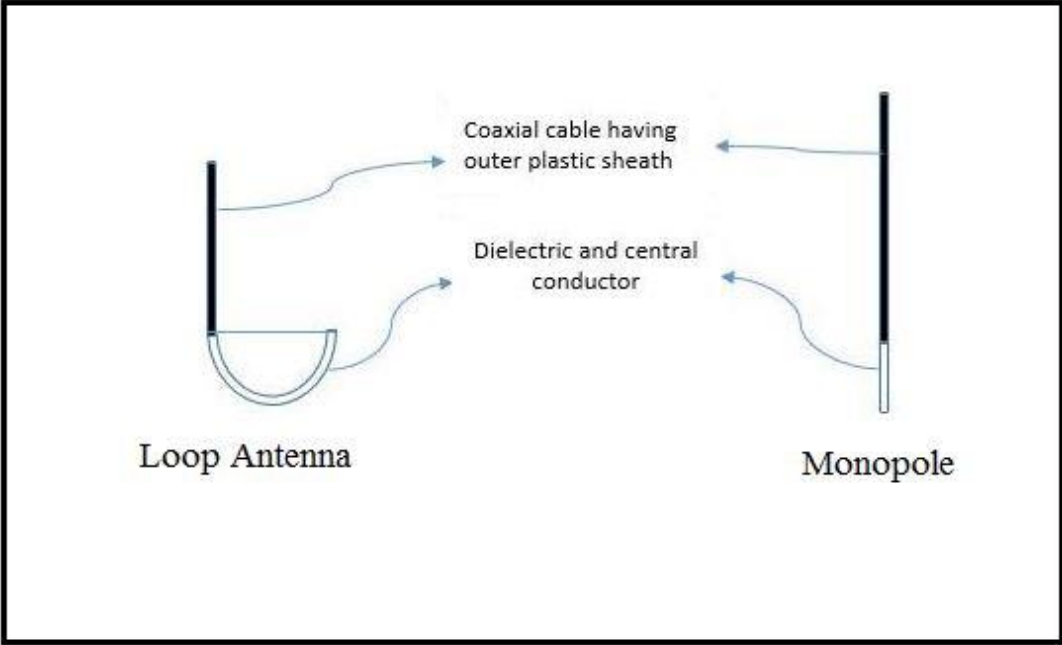


Figure 9. Loop and monopole antenna

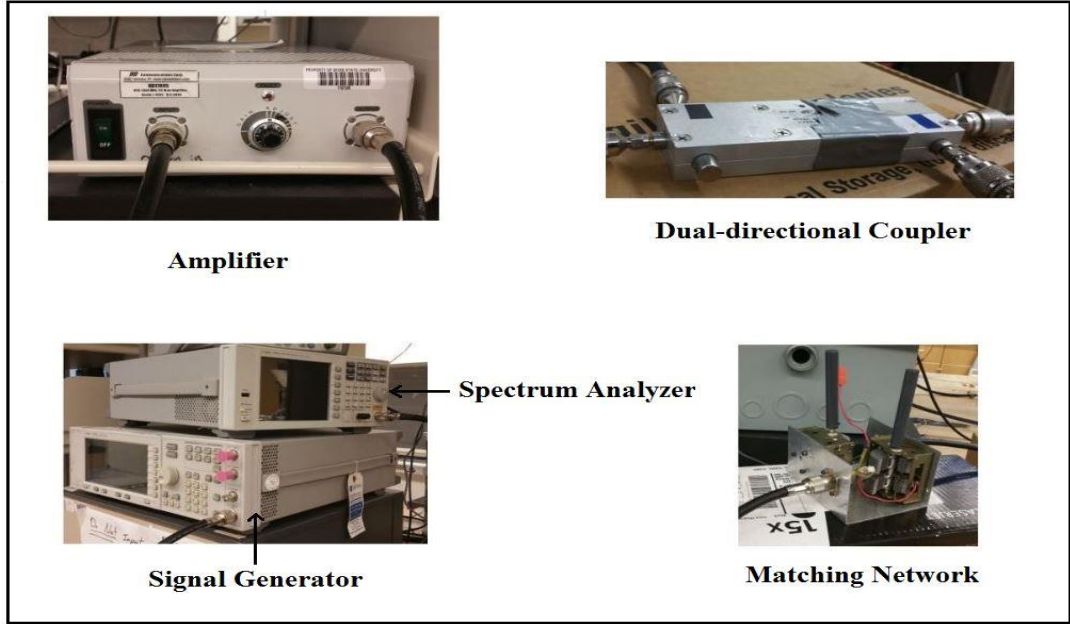
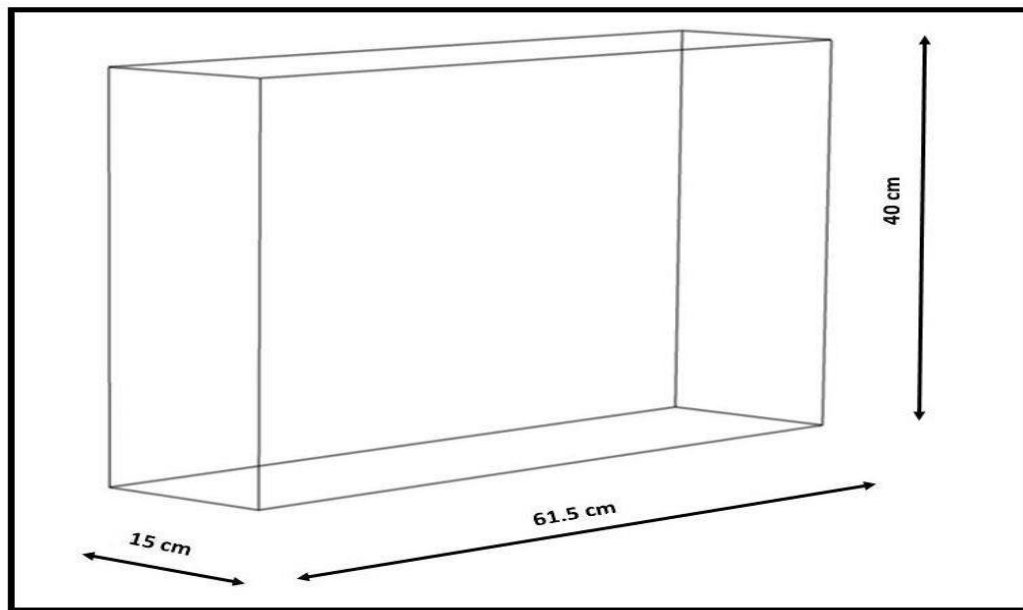


Figure 10. RF-launching setup

Laboratory Setup, Series I

In the first experimental work, impact tests were conducted to generate the EPWP to examine changes in the EPWP of the saturated specimen due to RF waves. The EPWP was generated by striking a rigid box filled with the saturated glass-bead specimen. The

rigid box of size 61.5 cm × 40 cm × 15 cm was made of Plexiglas. The thickness of walls of the box was measured to be 0.6 cm. A loop antenna was installed at the corner of the box. The dimension of the box was selected based on the availability of the material. In addition, the configuration of the size of the box and installation of the antenna at the corner provided maximum electric field at the location where the PWP transducer would be installed. Figure 11 shows the schematic of the box with its dimensions.



**Figure 11. Schematic of the impact-test box with dimension**

The top of the box had a removable cover. A number of holes were drilled on the cover of the box forming a grid with 2cm center-to-center spacing. During the electric-field measurement inside the box, the monopole probe was inserted into the soil through those drilled holes. Also, a 4-cm diameter hole was made at the center (along the length and width of the cover) on the top to allow the PWP transducer to be put inside the glass-bead specimen. The configuration and dimensions of the box and installation of antenna at the corner lead to the generation of maximum electric field at the location where the

PWP transducer was installed. Figure 12 shows the schematic of the impact-test box filled with a saturated specimen, loop antenna, and wire mesh covering the PWP transducer.

To mitigate any electromagnetic interference on the pore-pressure measurement, the transducer was cased within a PVC pipe, which was wrapped with a metallic mesh all the way to the top of the box and grounded to the cavity walls. Multiple holes were drilled into the PVC pipe to allow water flow. The setup helped to reduce any noise due to the RF field on the pore-pressure measurement. A valve was installed at a height of 3cm above the bottom of the box to allow drain and recharge of water in and out of the specimen respectively. As mentioned, sides of the box were covered with the electrically-conductive film and metallic tapes to provide a resonant-cavity structure.

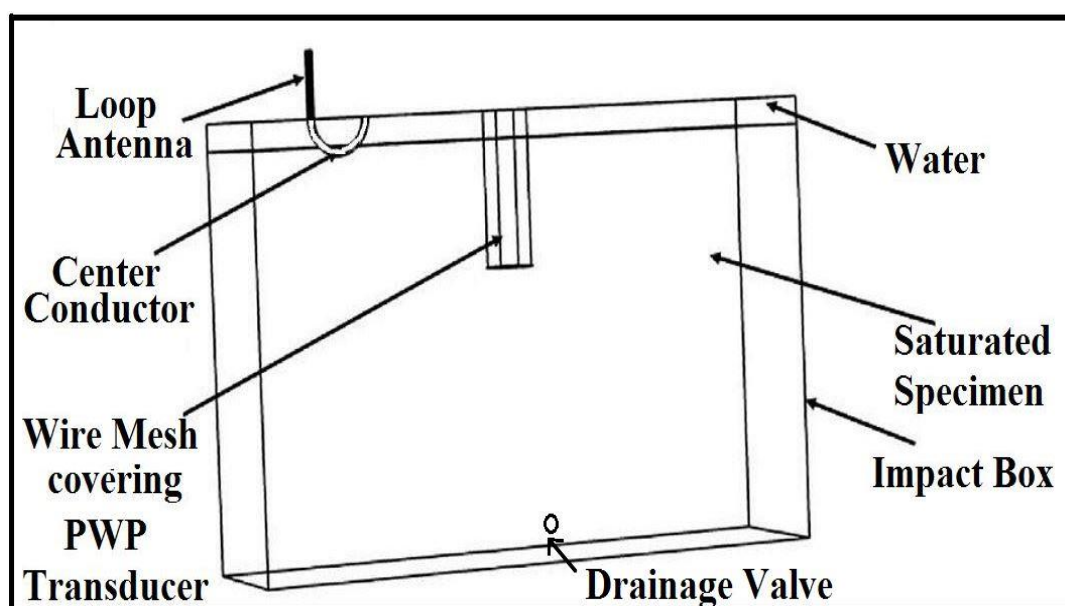


**Figure 12.** Schematic of the impact-test box with saturated specimen, loop antenna, and wire mesh covering PWP transducer



### Pore-pressure Measurement

A pore-pressure transducer was used to measure the PWP within the glass-bead medium before, during, and after impacts, with and without RF waves. The pore-pressure measurement setup consists of a Campbell Scientific, CS-451, pore-pressure transducer having the measurement time of 1.8 seconds, and CR 800, data-acquisition (DAQ) device. The PWP transducer can measure pressure between 0 to 20 kPa, and the accuracy of the transducer is  $\pm 0.1\%$ . The pore-pressure transducer was placed at the depth of 11 cm below the top of the glass-bead medium and 12 cm from the top of the box. Above the glass-bead medium up to the top of the box, there was about 1 cm of layer of water. Hence, the glass-bead specimen was completely submerged inside water. The PWP transducer consists of a piezo-resistive sensor placed inside a metal case, and it outputs a digital SDI-12 signal to provide the observed pressure. The maximum EPWP ratio ( $ru$ ) was calculated based on the pore-pressure data obtained using the transducer.



**Figure 13.** Pore-pressure transducer, CS451, and data-acquisition device, CR800

### Impact Test

After the glass-bead sample was prepared, the impact tests were conducted. The impact tests were conducted both for the RF-stimulated and unstimulated tests to observe the change due to the RF-stimulation. The impact was created by designing a periodic-pendulum mechanism with impact energy generated by the free swing of the pendulum. An object of mass 1.2 lbs. was attached to a hanging PVC pipe of the length 1.96m. Figure 14 shows the schematic detail of the laboratory setup for impact tests, and Figure 15 shows the setup for RF-stimulated impact tests. The mass of the object was selected large enough to cause impacts and generate EPWP, but small enough not to break and overturn the box. PVC pipe was guided using two wooden plates at the top to maintain a consistent path of movement. Another wooden plate was placed at the top to stop the PVC to produce a constant angle of swing of  $10^\circ$ . The configuration allowed the pendulum to hit the box at around 12.5 cm from the top of the box. The PWP transducer was also installed at that depth. The box was subjected to 8 impacts carried out for 25 seconds at a consistent frequency of  $8/25 \text{ Hz} = 0.32 \text{ Hz}$ . Two removable PVC stiffeners were also designed and installed to provide more stiffness to the box. To launch the RF stimulation inside the box, a loop antenna was submerged inside the glass-bead specimen. Tests were run at different power levels of 10, 25, and 40 Watts at a frequency of 498 MHz. Also, a set of tests were performed at different frequencies of 405, 485, 550, and 620 MHz.

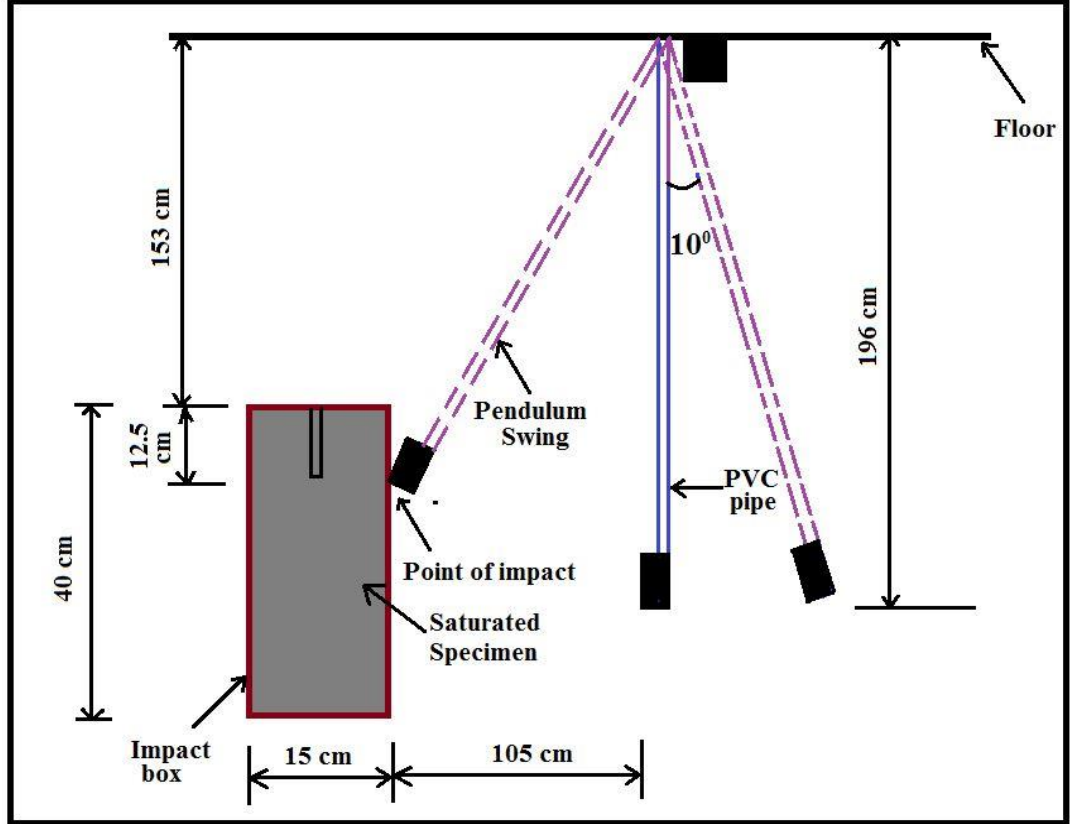


Figure 14. Schematic of the laboratory setup for impact tests on the box filled with saturated specimen of glass beads

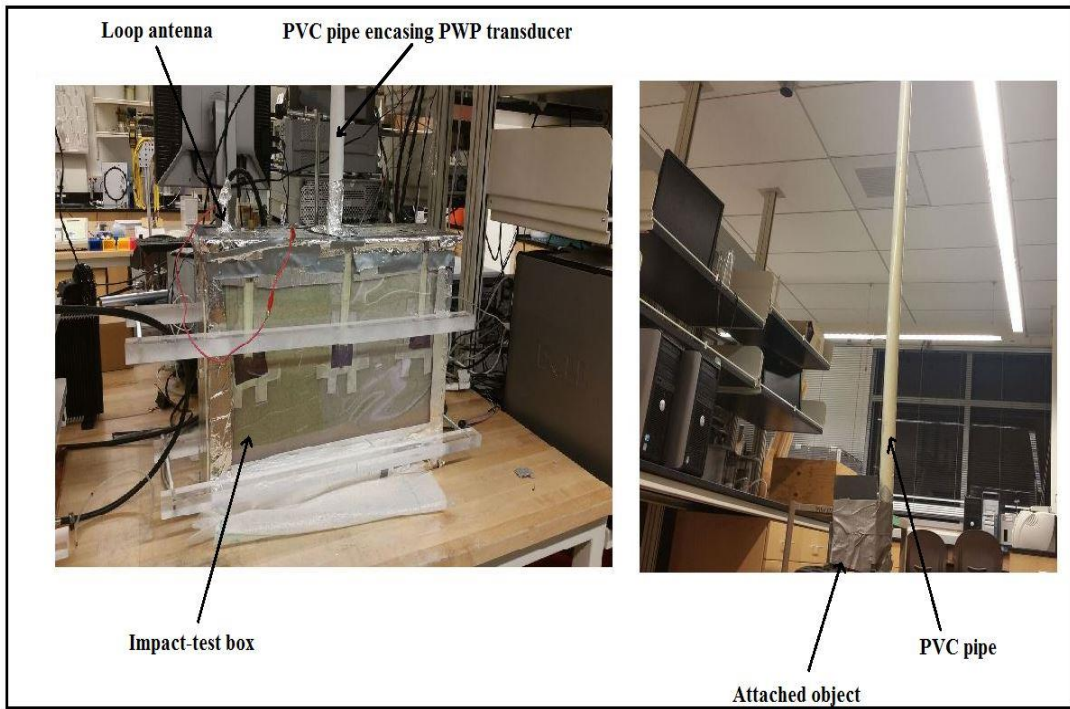


Figure 15. Setup for RF-stimulated impact tests

### Saturated-Sample Preparation

The saturated glass-bead samples were prepared using the wet-pluviation method (Vaid et al. 1988). Glass beads used for this study are Class-A Ballotini impact beads from Potters Company with a specific gravity of 2.46 g/cm<sup>3</sup>. Table II shows properties of glass beads.

The wet-pluviation method is adopted to produce a homogeneous loose specimen. Water was filled in up to a predetermined level of 16 cm (porosity of the saturated sample was measured to be 0.39). The funnel was fixed at 20 cm above the level of water. Glass beads were then smoothly poured over water through the funnel. The top of the glass-bead medium was smoothly levelled and precautions were taken not to have layering of one glass-bead layer over the other. The pouring was continued until the saturated specimen of the desired thickness was achieved. From mass and volume of glass beads and water, the porosity and final density of samples were measured.

**Table II. Properties of glass beads (Najafi, 2014)**

<b>Potters Designation</b>	<b>US Sieve #</b>	<b>Maximum Size (inch.)</b>	<b>Minimum Size (inch.)</b>	<b>Maximum Size (µm)</b>	<b>Minimum Size (µm)</b>	<b>Minimum % of Round Beads</b>
Class A	20-30	0.0331	0.0234	850	600	65

The water used for this test was deaerated and deionized. The purpose of using deionized water is to create a controlled mechanism with a lower conductivity and, hence, low EM loss. Natural water may contain minerals, which can alter the EM field within the medium because of its higher conductivity. The purpose of using the deaerated

water is to eliminate air entrapment within the soil. The deaeration of water was performed using an ELE brand water-deaerating system for at least 45 minutes per batch of water.

### Laboratory Setup, Series II

In the second experimental setup, the hydraulic-conductivity study was carried out. Constant-head tests were performed because samples under the study were coarse grained. Glass beads and natural sand were used as the coarse-grained samples in these tests. The natural sand used is classified as well-graded sand (SW) according to USCS classification system. Properties of glass beads used in these tests are presented in Table II, and Figure 16 shows the gradation curve for the natural sand.

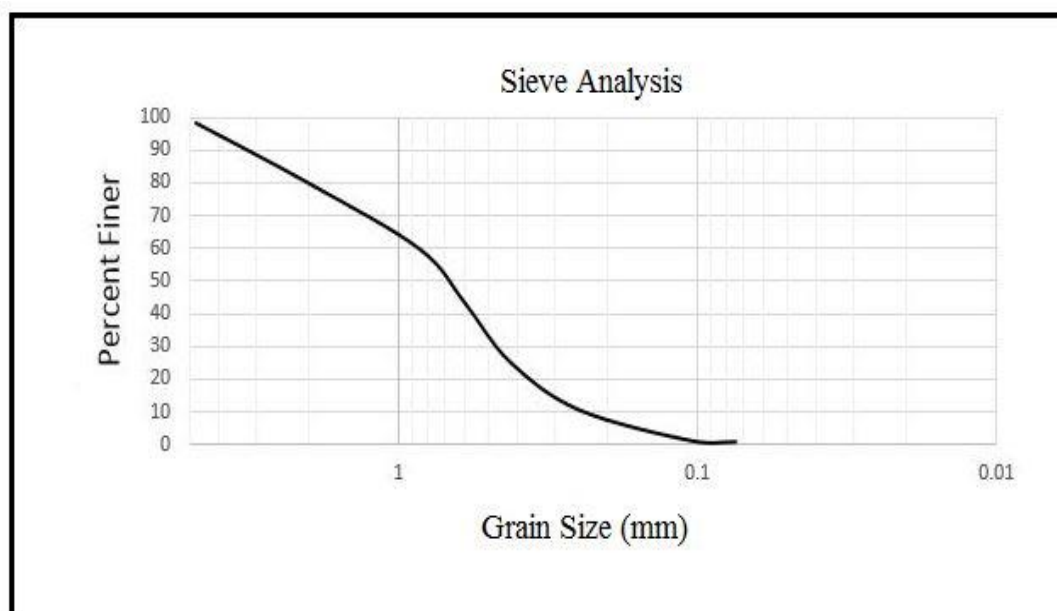


**Figure 16. Grain-Size distribution chart of natural sand**

To perform the hydraulic-conductivity tests, a customized, rigid-wall, cylindrical permeameter was constructed using acrylic material. However, before performing the tests using the customized permeameter, the customized device needed to be calibrated.

Hence, the unstimulated tests were performed using both the standard permeameter (2.5inch diameter and 12inch height) as suggested by D2434 (ASTM, 2006) and the customized permeameter (152mm diameter and 140mm height) to calibrate the customized permeameter. The depth of the soil specimen in the customized permeameter is 110 mm. Figure 17 shows the schematic of the setup and its dimension, and Figure 18 shows the setup for the RF-stimulated hydraulic-conductivity tests.

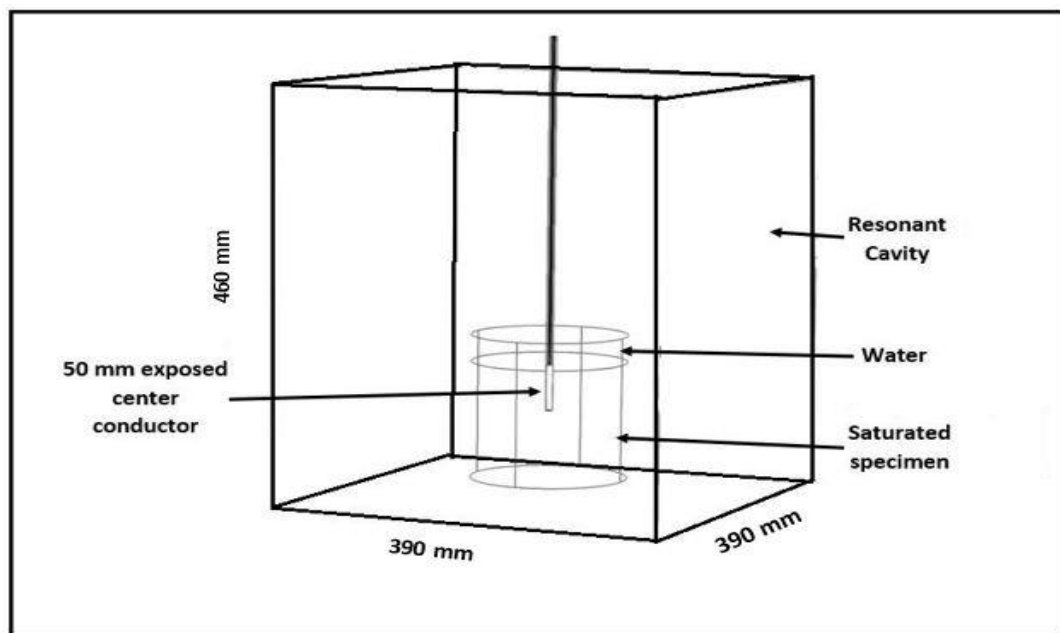


**Figure 17. Schematic of the RF-stimulated hydraulic conductivity tests**



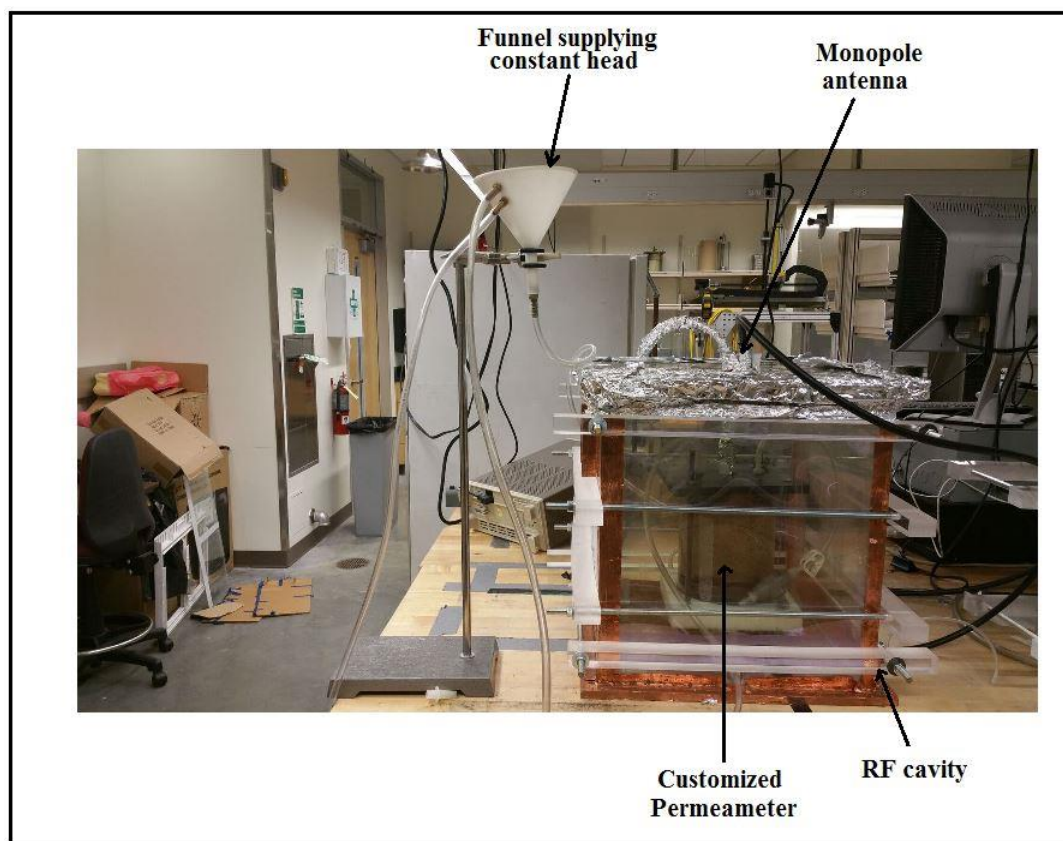


**Figure 18. Setup for RF-stimulated hydraulic-conductivity tests**

The results of the two permeameters were compared to calibrate out the discrepancies. The customized permeameter was placed inside a  $460\text{mm} \times 390\text{mm} \times 390\text{mm}$  RF-resonant cavity similar to the one of Series I experiments (i.e., Plexiglas box with its six walls covered with electrically conductive, grounded, transparent films). Other equipment and devices are two porous stones, two rubber stoppers, springs, a large funnel, a stand, a scale, clamps, and plastic tubes. Both glass beads and natural sand were used as the samples in the hydraulic conductivity tests.

Figure 19 shows the schematic of the customized rigid-wall permeameter. Porous stones were placed on the top and on the bottom of the glass-bead or natural-sand samples. Porous stones help to allow drainage in the vertical direction as well as to prevent the soil from being washed away by the seeping water. Filter papers were also

placed on the bottom of the top porous stone and on the top of the bottom porous stone to avoid clogging of the porous stones. Before preparing samples, the mass of the permeameter (the tube, porous stones, springs, and two rubber stoppers) were measured. Afterwards, oven-dried glass beads were poured into the permeameter using the dry-pluviation method to prepare the glass-bead sample. To prepare the natural-sand sample, natural sand was poured into the permeameter in three layers, and each layer was compacted. The dry-pluviation method was used instead of wet pluviation for glass beads because with the dry-pluviation method, difficulty of leaking and working with watery samples was averted. The total density of the glass-bead sample was measured to be  $14.72 \text{ kN/m}^3$ . In the case of natural sand, each layer was compacted using 50 blows using a standard proctor hammer. Azad (2013) prepared samples with 50 blows compaction per each of three layers. The selection of the number of blows in this research was based on applying a similar level of compaction to the work by Azad (2013) to replicate her test specimens. The density of the sample was measured to be  $18.25 \text{ kN/m}^3$ . The permeameter was filled up to the desired length of 110 mm. Springs were placed above the porous stone on the top of the sample to prevent any volume and effective-stress change due to swelling. After the sample was prepared, the total mass of the permeameter with the sample was measured.



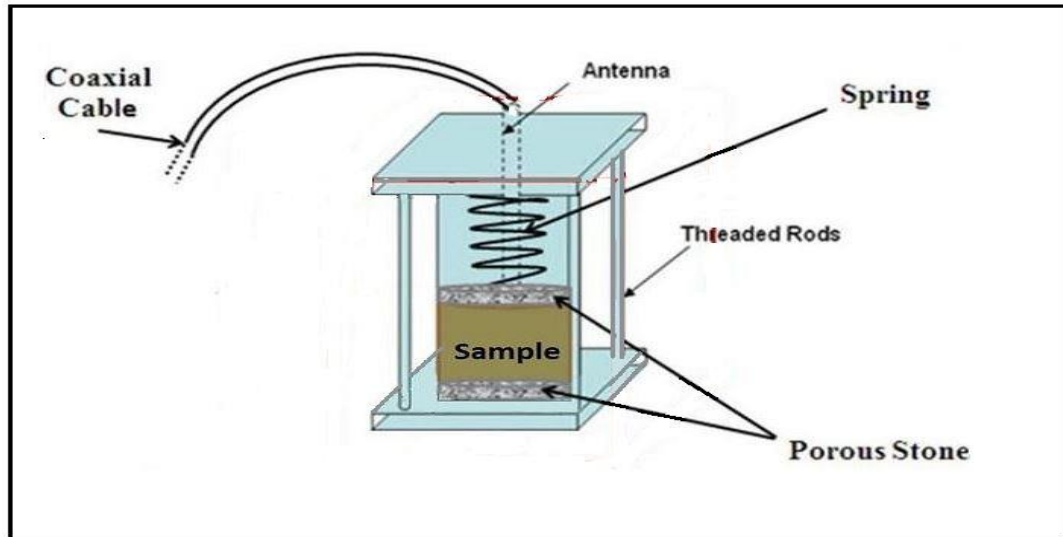


**Figure 19. Schematic of customized, rigid-wall, cylindrical permeameter designed to conduct RF-stimulated hydraulic-conductivity tests on Sand (Azad, 2013)**

The two ends of a plastic tube were connected to a funnel affixed to a stand at a specific height and to the bottom of the permeameter. The funnel is connected to the source of water while there is another outlet in the funnel to drain extra water and maintain the input hydraulic head constant. This will create a constant head and an upward flow of water through the sample, which should help to push any air bubbles entrapped within the sample. For both the glass-bead and natural-sand samples, both unstimulated and RF-stimulated constant-head hydraulic-conductivity tests were performed. As mentioned, in the case of RF-stimulated tests, the setup was prepared, and impedances of the DUT and the RF source were matched. RF stimulation was performed on both the glass-bead and natural-sand samples at a frequency of 726 MHz and power levels of 10, 25, and 40 Watts. Tests were not performed at variable frequencies because at different frequencies, electric-field patterns within the specimen would be different, and the direct correlation between changes observed in the hydraulic conductivity could not be developed with the change in frequencies. In other words, to truly evaluate the

frequency effect, cavities of various sizes are required, which did not fit within the scope and time limits of this project. This is further explained in the “Result” section.

### Sample Preparation

As mentioned, in the case of the natural sand, samples were prepared by compacting soil in three layers. However, in the case of glass beads, the compaction of glass beads is very difficult and ineffective because of the round shape of the beads and uniform (poorly graded) nature of the beads. Hence, the glass-bead samples were prepared using the dry-pluviation method. The natural-sand samples were prepared by filling the permeameter with sand in three layers as each layer was compacted using 50 blows with a standard compaction hammer. The total density and porosity of sand samples was calculated based on the measurements of the mass of the sample and the equipment.

Water used for this test was also deionized. The deaerated water was only used once to evaluate the effect of air entrapment by comparing the discrepancy between the measured hydraulic-conductivity values using both deaerated deionized and deionized water without deaeration. Because the tests were conducted for several hours, it was impractical to prepare enough deaerated water for multiple tests during such a long period of time. The discrepancy was minimal.

### **Electric-Field Mapping**

Verification of the presence and measurement of the RF field inside the cavity was performed using a vertical monopole probe for both impact and hydraulic-conductivity tests. RF-field measurements at a specific location within the cavity are needed to understand the electric- and magnetic-field patterns. The vertically placed

monopole probe is polarized vertically, and its measurements are hence dominated by the vertical component of the electric field (in this case,  $E_z$ ). The measurement of the electric-field component of RF-waves was performed and plotted to evaluate the effect on hydraulic conductivity. Moreover, the electric field was numerically simulated using COMSOL Multiphysics and validated against the experimentally measured electric field.

As mentioned, the monopole probe was made of an RG-402 cable, with 25 mm of its outer conductor stripped at the end. Using an RG-58, 18GHz precision-test cable, the monopole probe was connected to a spectrum analyzer to measure the electric field at the corresponding location of the probe inside the cavity. The cable has an N-type male connector connected to the spectrum analyzer and an SMA male connector connected to the monopole probe. The monopole probe was placed inside a glass-tube casing to provide rigidity and waterproofing. To insert the probe into the specimen, a number of holes were drilled on a 2cm x 2cm grid in the XY plane through the top plate of the resonant cavity. The insertion of the monopole probe in the vertical direction through holes was performed manually. The measurement was conducted by locating the probe in the designated measurement location. The location of the probe on the top would decide the respective X and Y coordinate of the probe, and the depth of the insertion would give the Z coordinate. Thus, the value of the electric field measured using the spectrum analyzer can be tabulated for the corresponding Cartesian coordinates (X, Y, Z) on a two-dimensional (2D) or three-dimensional (3D) grid. Before the measurement, at all points, the probe was stopped for two seconds to allow the measurement of the spectrum analyzer to stabilize. Measurements are the recorded power in dBm using the spectrum analyzer at the frequency generated by the signal generator. As mentioned, after the

collection of electric-field measurements, results were plotted to achieve a contour map of the electric field. The electric field was also numerically simulated using the RF module of COMSOL Multiphysics and validated against the experimentally-measured electric field. More details about the electric-field mapping are described below for Series-I and Series-II tests.

#### Electric-Field Mapping for Impact Tests, Series I

In the case of impact tests, measurements of the vertical component of the electric field were performed near the PWP transducer installed within the cavity. As mentioned, before placing the transducer at the appropriate location, the electric field's pattern was studied directly from the results obtained using the RF module of COMSOL model. The frequencies of RF-stimulated tests were selected such that the maximum intensity of the electric field could be obtained near the PWP transducer. In the case of impact tests, electric-field measurements were performed at the frequencies of 498 MHz and 632 MHz. The location of the measurement along the X direction was fixed at a distance of 4 cm away from the pore-pressure transducer. A total of six points along the Y axis are selected at 2cm intervals. Figure 20 shows the schematic of the top view of the of the resonant cavity with the location of depth slices.

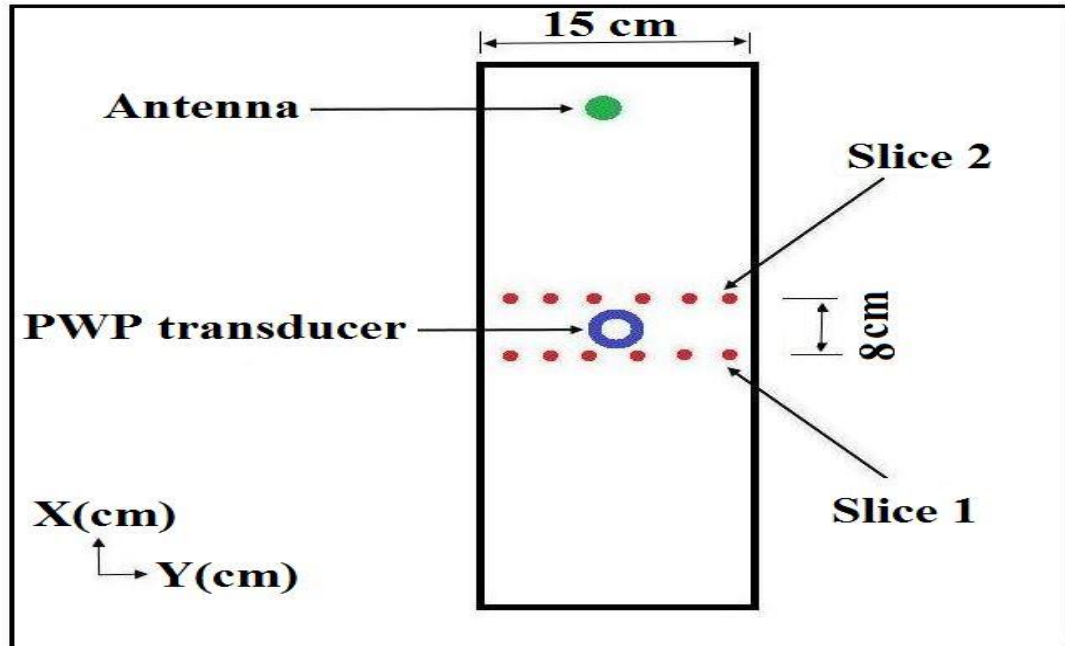
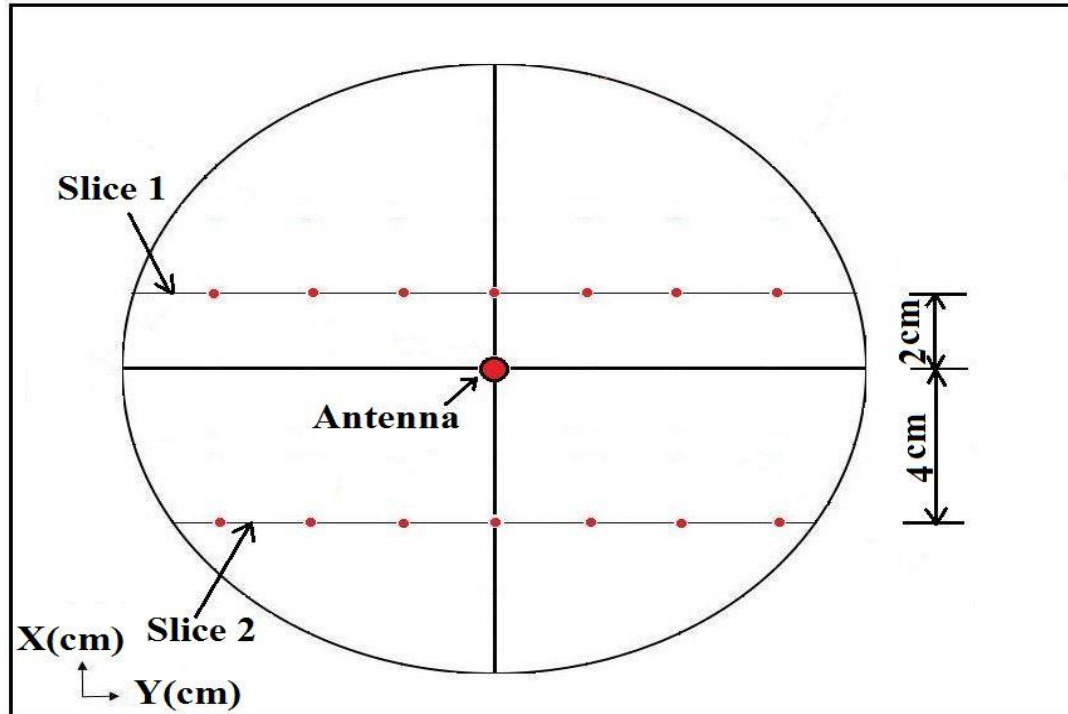


Figure 20. Schematic of the top view of the resonant cavity showing the location of depth slices for the impact test, Series I

#### Electric-Filed Mapping for Hydraulic-Conductivity Tests, Series II

A similar approach was taken to measure the electric field within the customized permeameter for hydraulic-conductivity tests. The frequencies were selected to achieve the maximum electric field within the permeameter. In the case of hydraulic-conductivity tests, electric-field measurements were performed at frequencies of 710 MHz and 726 MHz. The location of the measurement probe along the X direction was fixed at distances of 2 cm and 4 cm from the centrally-placed source (monopole antenna). A total of seven measurement points on grid along the Y axis are selected, which are separated at 2cm intervals. Figure 21 shows the schematic of top view of the customized permeameter with the location of the depth slices.



**Figure 21. Schematic of top view of the customized permeameter showing the location of the depth slices for hydraulic-conductivity tests, Series II**

### 3D Numerical Forward Model of Seepage Flow for Series-II Tests

The aim of numerical seepage modelling is to correlate the RF field with the change in the hydraulic conductivity due to RF stimulation. As mentioned, a finite-difference numerical forward model was developed in MATLAB interface to analyze the seepage flow. The numerical model was also validated against experimentally measured hydraulic conductivity by comparing the numerically simulated value of the discharge with the experimentally measured value. The numerical model was then used to find the spatial variation of the hydraulic head within the soil specimen. The following describes this forward model.

#### Seepage flow

The seepage flow is governed by the mass-continuity equation. The flow velocity can also be modeled using Darcy's law.

According to the mass-continuity equation, the rate at which a mass of water enters a water-saturated system is equal to the rate at which the water mass leaves the water-saturated system.

In differential form, the mass-continuity equation can be written as follows:

$$\frac{\partial \rho}{\partial t} + \vec{\nabla} \cdot (\rho \vec{V}) = 0 \quad (16)$$

where:

$\rho$  = fluid density (m<sup>3</sup>/s)

$t$  = time (s)

$\vec{V}$  = seepage flow velocity vector

In the case of incompressible fluids, the density of the fluid is constant. Hence the mass-continuity equation (Equation 16) can be simplified to a volume-continuity equation, which can be written as follows:

$$\vec{\nabla} \cdot \vec{V} = 0 \quad (17)$$

Then the velocity vector of Equation 17 can be represented in terms of hydraulic conductivity and hydraulic-gradient vectors using Darcy's law. Equation 17 can then be written as follows:

$$\vec{V} = -k\vec{I} \quad (18)$$

where:

$k$  = hydraulic conductivity in m/s

$\vec{I} = \vec{\nabla}h$  = hydraulic-gradient vector

Equation 18 can then be expressed as follows:

$$\vec{V} = -k\vec{\nabla}h \quad (19)$$

Hydraulic gradient,  $\vec{I}$  can be written as follows:

$$\vec{l} = \vec{\nabla}h = \frac{\partial h}{\partial x} \vec{i} + \frac{\partial h}{\partial y} \vec{j} + \frac{\partial h}{\partial z} \vec{k}$$

Equation 17 can be written as follows:

$$\vec{\nabla} \cdot (-k\vec{\nabla}h) = 0 \quad (20)$$

Equation 20 can be written in the matrix/tensor form as follows.

$$\vec{\nabla} \cdot \vec{\nabla} = - \left\{ \frac{\partial}{\partial x} \quad \frac{\partial}{\partial y} \quad \frac{\partial}{\partial z} \right\} \begin{bmatrix} k_{xx} & k_{xy} & k_{xz} \\ k_{yx} & k_{yy} & k_{yz} \\ k_{zx} & k_{zy} & k_{zz} \end{bmatrix} \left\{ \begin{array}{c} \frac{\partial}{\partial x} \\ \frac{\partial}{\partial y} \\ \frac{\partial}{\partial z} \end{array} \right\} h = 0 \quad (21)$$

where:  $k = \begin{bmatrix} k_{xx} & k_{xy} & k_{xz} \\ k_{yx} & k_{yy} & k_{yz} \\ k_{zx} & k_{zy} & k_{zz} \end{bmatrix}$  is the hydraulic-conductivity tensor.

The water-saturated soil specimens under the study have dimensions of 15 cm × 11 cm, where 15 cm is the diameter and 11 cm is the height of the water-saturated soil specimen. The entire grid used to model the flow under study is a rectangular-cubical specimen having dimensions of 15 cm × 15 cm × 11 cm. This rectangular-cubical domain was discretized into 15 nodes along X and 15 nodes along Y axes. The necessary boundary conditions were applied to solve the seepage problem of the cylindrical specimen in the middle of cubical grid while also addressing the discrepancy caused due to modeling a cylindrical boundary on a 3D rectangular grid. The top view of the domain discretized having circular and rectangular cross sections is shown in Figure 22.



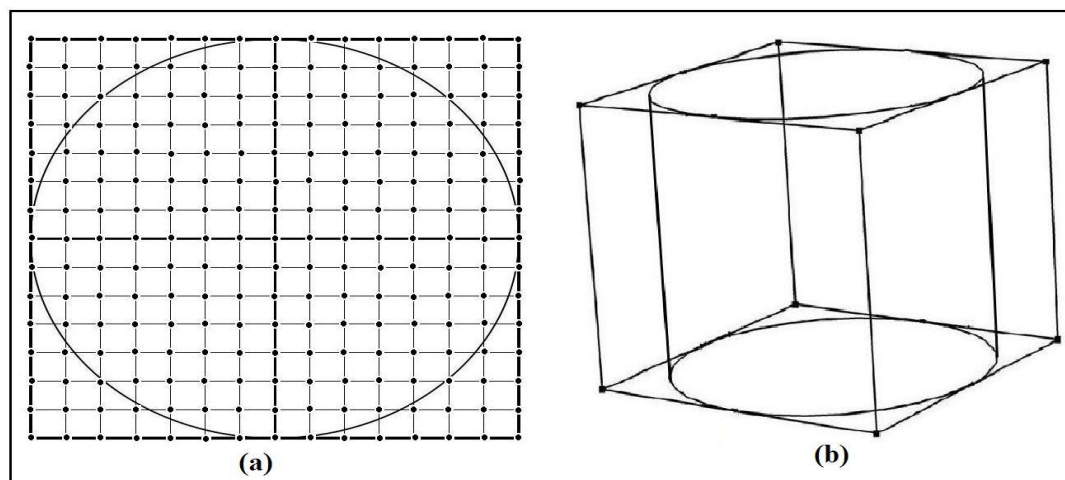


**Figure 22.** Schematic of (a) top view of the discretized rectangular cubical domain with circular cross section of the specimen, (b) 3D view of the rectangular cubical domain and cylindrical region within the sample.

Boundary conditions (BC) specify known values or derivative over the boundaries (Dirichlet and Neuman boundary conditions). Types of boundary conditions used in the analysis of seepage flow are as follows.

(1) Dirichlet BC:

The total head is specified. Either the head ( $H$ ) is a function of time and space or a constant quantity.

(2) Neumann BC:

The discharge, hence, the gradient of hydraulic head is assigned. Either there is no flow on the boundary, or there is a specified flux. When there is a specified flux, discharge ( $Q$ ) varies with space and time. When there is no flow, discharge ( $Q$ ) is zero.

The top and the bottom surface of the cylindrical specimen are modeled as Dirichlet boundary conditions with known hydraulic heads. Since the hydraulic-conductivity tests were conducted with the upward flow of water, the hydraulic head at the bottom of the specimen is the fixed hydraulic head of the constant level of water in the funnel with respect to an arbitrarily selected datum. Similarly, the hydraulic head at

the top of the specimen is calculated based on the position of the outlet pipe with respect to the datum. However, the circumference of the permeameter is an impermeable boundary, modeled as a Neuman BC. In addition, to meet the proper boundary conditions for the seepage analysis of the cylindrical specimen on a rectangular grid, the hydraulic heads of the nodes inside the rectangular domain but outside the circumference of the cylindrical specimen were considered zero. This would only work, if these nodes are isolated from the flow within the cylinder using a BC impermeable to radial flow.

Discretization of the domain and adding necessary boundary conditions lead to the calculation of the hydraulic head at each node. A computational code in MATLAB based on the central finite-difference method was developed and then used to calculate the spatial variation of the hydraulic head within the soil using the hydraulic-conductivity value obtained for the unstimulated tests. Equation 21 was used, and the flow through the soil was considered at the steady state for the unstimulated tests. The flow and discharge rates were also calculated. However, this only solved the hydraulic head inside the specimen while the test was performed in unstimulated condition.

The hydraulic head under RF stimulation was assumed to be  $k'$ , and Equation 20 for the flow can be written as follows.

$$\vec{\nabla} \cdot \vec{V} = - \left\{ \frac{\partial}{\partial x} \quad \frac{\partial}{\partial y} \quad \frac{\partial}{\partial z} \right\} \begin{bmatrix} k'_{xx} & k'_{xy} & k'_{xz} \\ k'_{yx} & k'_{yy} & k'_{yz} \\ k'_{zx} & k'_{zy} & k'_{zz} \end{bmatrix} \begin{Bmatrix} \frac{\partial}{\partial x} \\ \frac{\partial}{\partial y} \\ \frac{\partial}{\partial z} \end{Bmatrix} h = 0 \quad (22)$$

where:  $k' = \begin{bmatrix} k'_{xx} & k'_{xy} & k'_{xz} \\ k'_{yx} & k'_{yy} & k'_{yz} \\ k'_{zx} & k'_{zy} & k'_{zz} \end{bmatrix}$  is the RF-stimulated hydraulic-conductivity

tensor.

Since the application of RF waves have demonstrated to alter the hydraulic conductivity, it can be proposed that the RF-stimulated hydraulic conductivity ( $k'$ ) and the flow discharge ( $Q_{st}$ ) in the RF-stimulated tests are functions of the electric field,  $E$ .

Hence,

$$k' = f(E) \text{ \& } Q_{st} = f(E) \quad (23)$$

In addition,

$$s = \frac{E^2}{Z_0} \text{ Or, } E = \sqrt{sZ_0} \quad (24)$$

where:

$s$  = RF-power density ( $\text{W}/\text{m}^2$ );

$Z_0$  = characteristic impedance of the free space ( $\Omega$ )

$$P = s a \quad (25)$$

where:

$P$  = RF power (Watts)

$a$  = area enclosing the node ( $\text{m}^2$ )

From equation 23, 24, and 25, it can be proposed that the hydraulic conductivity and the flow discharge in the RF-stimulated test are functions of the RF power density and, hence, RF power. The results have shown an increase in the hydraulic conductivity with the increase of power level in coarse-grained media, which will be discussed in the Chapter 4. A nonlinear but proportional relationship is assumed between RF-stimulated hydraulic conductivity,  $k'$ , and power,  $P$ . Based on Equations 23, 24, and 25, the increase in the hydraulic conductivity with the RF power can be correlated as follows.

$$k' = k + \beta\sqrt{P} \quad (26)$$

where:

$\beta$  = a constant value,

$k$  = unstimulated hydraulic conductivity, (cm/s).

Therefore, increase in  $k'$  for each discretized node in the soil-specimen domain could be correlated to the increase in RF power at that node while calculating the hydraulic head at that specific node. Equation 25 can be redefined as follows.

$$k' = k + \beta\sqrt{s a} \quad (27)$$

A similar computational code in MATLAB Interface was developed to solve Equations 22 and 27. The RF-power density at each node was obtained from the RF forward model generated using COMSOL Multiphysics. The RF-power densities in the form of a 3D matrix were exported from the COMSOL model into the MATLAB interface. Afterwards, an optimization scheme was implemented to find  $\beta$  by minimizing a cost function (otherwise known as objective function) equal to the difference between the simulated RF-stimulated discharge,  $Q_{sim,st}$  and the experimental discharge value,  $Q_{exp,st}$ . The computational code was run by exporting RF-power densities at a frequency of 726 MHz at power levels of 10, 25, and 40 Watts.

## CHAPTER FOUR: RESULTS

Results, summarized in this chapter consist of outcomes for the two different experimental setups (Series I and II) presented in two segments. The results of the impact test are presented in the first segment. As mentioned, impact tests were performed on the glass-bead sample. The generated EPWP during the unstimulated and RF-stimulated tests (stimulated at varying RF powers and frequencies) is presented. In addition, the relationship between the effect of the RF power and generated EPWP is demonstrated. The experimentally measured electric field and the numerically simulated electric field using COMSOL Multiphysics are presented and compared to validate the numerical simulation.

The second section consists of the results of the hydraulic-conductivity tests. Results for the unstimulated and RF-stimulated tests performed on the glass-bead and natural-sand sample are then presented. The temporal variations of the hydraulic conductivity are also presented when the RF field is turned on and terminated. In the end, numerically-simulated discharge and experimentally measured discharge are compared. The comparison was used in an optimization scheme to find the governing relation between the RF field and hydraulic conductivity alteration.

### **Series 1: Impact Tests**

Impact tests were performed on the glass-bead sample at varying input powers and frequencies. In addition, an impact test without the presence of RF waves was

performed. For each type of test (i.e., unstimulated and RF-stimulated tests at different power levels and frequencies) within Series I, three sets of tests were performed. For each type of test, for the first run of the test, a new sample was created and the test was conducted. The other two remaining tests out of three were performed without creating a new sample all over again. Those tests were performed by drainage and recharge of water using the valve present on the bottom of the specimen box. The drainage and recharge method was used to facilitate and ease the conduction of the tests. The discrepancy that could occur while using the drainage-recharge method was examined from unstimulated impact tests. Figure 23 shows the relation between the pressure head (cm) of water with time for the unstimulated impact test. The three plots in the figure are the graphs for three trials in succession. The letter 'F' in the figure represents the trial performed at the start or the first test. The second and third tests performed after drainage and recharge are represented with letter 'S' and 'T.' The PWP head before the impact for the three sets were maintained nearly equal.

The specimens were then subjected to 8 cycles of periodic impacts. With the application of impacts, the pore pressure started to buildup. The PWP head in these three samples right after the 8<sup>th</sup> impact reached maximum values of 13.78 cm, 13.82 cm, and 13.8 cm corresponding to an increase in EPWP head of 1.96 cm, 1.93 cm, and 2.02 cm, respectively. The average value of EPWP head was 1.97 cm, and its standard deviation was 0.0374 cm. Hence, the increase in the EPWP can be considered nearly consistent. In addition, the effect due to the drainage and recharge is visibly within the margin of error of pore-pressure measurements.

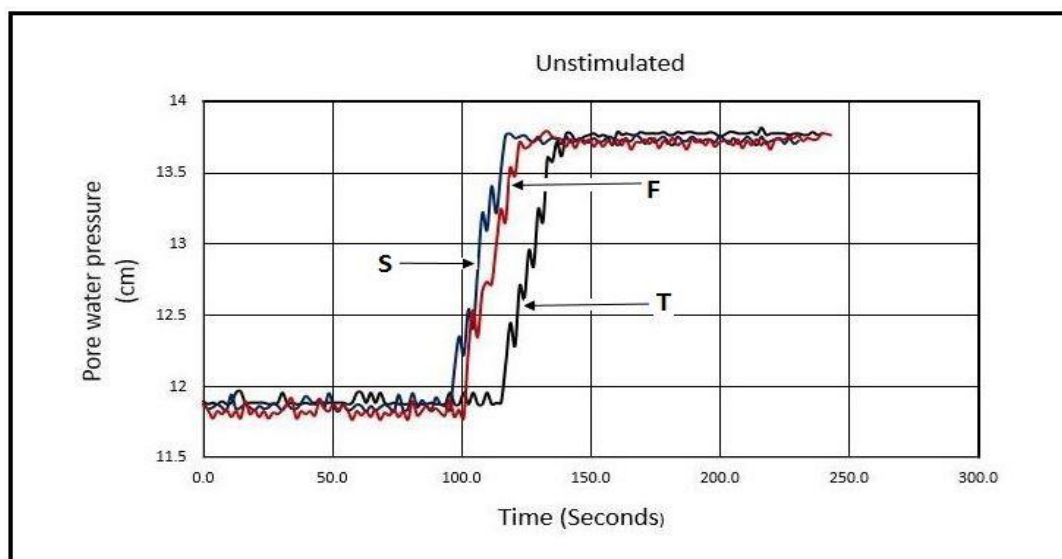
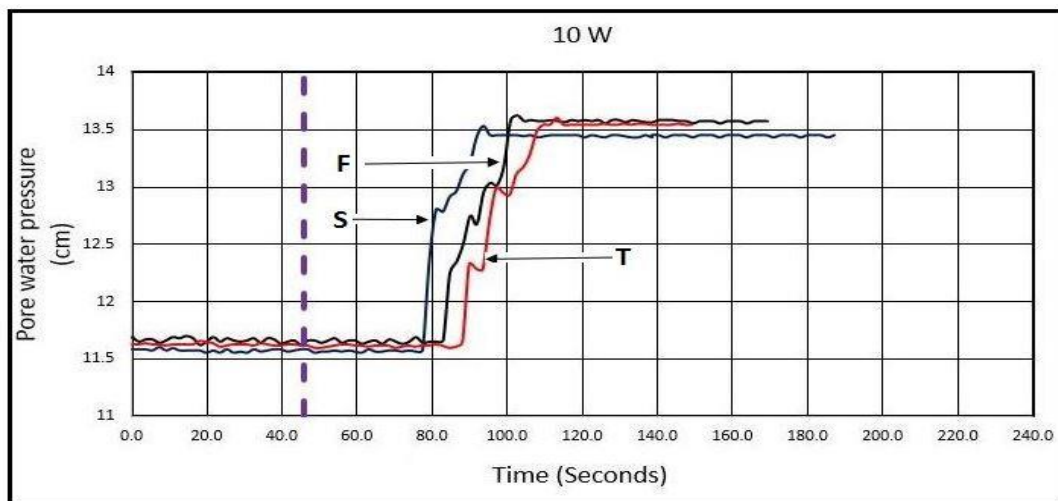
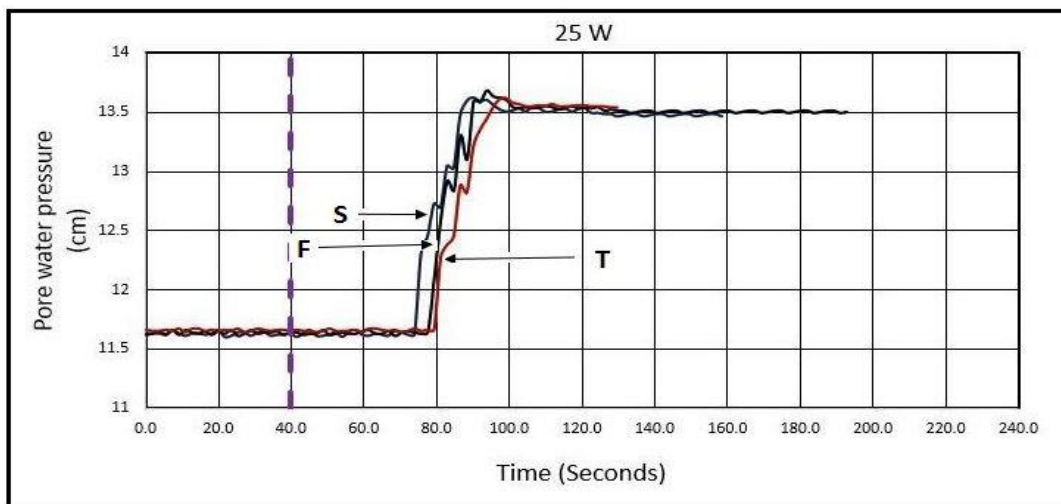


**Figure 23. Pore-water pressure head (cm) versus time (sec.) in glass-bead sample during unstimulated impact tests.**

In the case of varying RF powers, the RF-wave frequency was set to 498 MHz. The tests were performed at power levels of 10, 25, 40, and 50 Watts. Figures 24 a through 24 d show the plot of the pore-water pressure measurement in the glass-bead sample during RF-stimulated impact tests. As mentioned, letters F, S, and T indicate the first, second, and third tests. The second and third tests were performed after the drainage and recharge cycles. The dashed vertical line represents the time RF stimulation started. Before the RF stimulation, the PWP was maintained relatively equal for all three tests. The time between the start of RF stimulation and the start of the impact was between 30 to 45 seconds. As observed in Figure 24, there was a sharp increase in the EPWP (within 1.8 seconds, which is the measurement time) after the impacts. At the end of all impacts, the pore pressure ascended to a maximum value. It can be observed in Figure 24 that all three tests follow similar trends of rising EPWP. In addition, the increase in the PWP for the three sets of tests at each RF-power level is nearly equal.



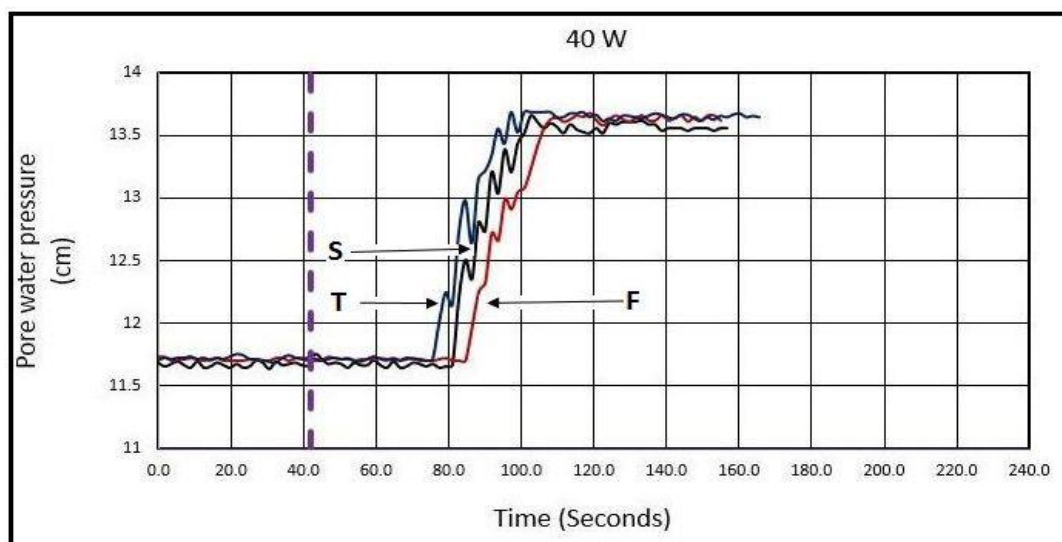
(a)



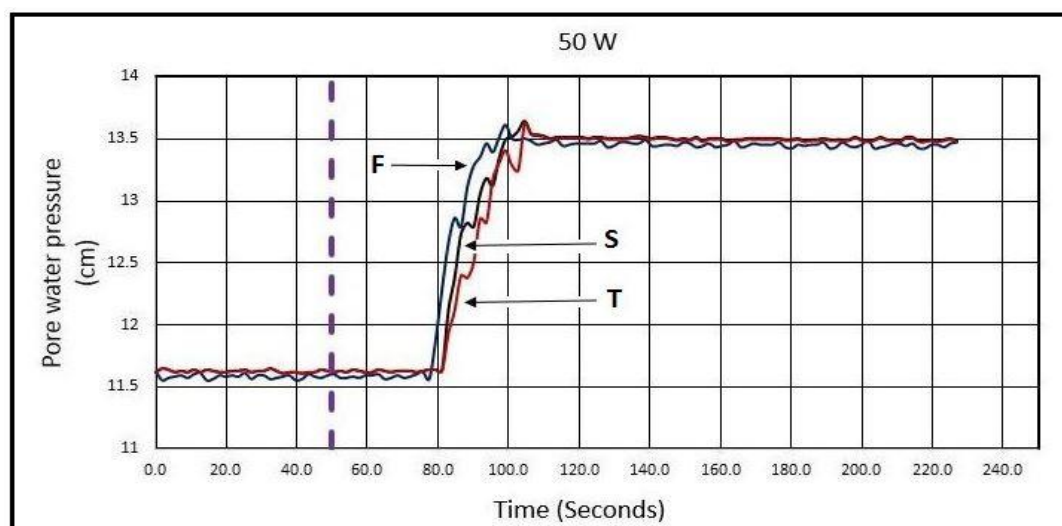
(b)

**Figure 24.** Pore-water pressure head (cm) versus time (sec.) in glass-bead sample during RF-stimulated impact tests (vertical dashed line: time of RF stimulation) at frequency of 498 MHz and power level of: a) 10 Watts; and b) 25 Watts





(c)



(d)

**Fig 24 (Contd.).** Pore-water pressure head (cm) versus time (sec.) in glass-bead sample during RF-stimulated impact tests (vertical dashed line: time of RF stimulation) at frequency of 498 MHz and power level of: c) 40 Watts; and d) 50 Watts

The EPWP values before and after impacts as well as the mean EPWP and standard deviation are shown in Table III. Figure 25 shows the plot of the mean EPWP at different RF-power levels at the frequency of 498 MHz. It can be observed from Table III and Figures 25 that the mean EPWPs during RF-stimulated impact tests at various RF-

power levels are almost equal. The PWP values before the impact at all RF-power levels were maintained nearly equal.

**Table III.  $\Delta$ PWP for three different tests at various RF-power levels**

Pore Water Pressure																
Test No.	1				2				3							
Power	PWP BEFORE (cm)	PWP AFTER (cm)	$\Delta$ PWP (cm)	$\Delta$ PWP (Pa)	PWP BEFORE (cm)	PWP AFTER (cm)	$\Delta$ PWP (cm)	$\Delta$ PWP (Pa)	PWP BEFORE (cm)	PWP AFTER (cm)	$\Delta$ PWP (cm)	$\Delta$ PWP (Pa)	MEAN $\Delta$ PWP (cm)	MEAN $\Delta$ PWP (Pa)	Standard deviation (cm)	Standard deviation (Pa)
0	13.78	11.82	1.96	192.1	13.82	11.89	1.93	189.1	13.8	11.78	2.02	198	1.97	193.1	0.0374	3.6668
10	13.53	11.57	1.96	192.1	13.63	11.66	1.97	193.1	13.6	11.65	1.95	191.1	1.96	192.1	0.0082	0.8002
25	13.68	11.64	2.04	199.9	13.63	11.62	2.01	197	13.62	11.64	1.96	192.1	2.003	196.3	0.0330	3.2338
40	13.68	11.7	1.98	194	13.66	11.67	1.99	195	13.68	11.69	1.96	192.1	1.977	193.7	0.0125	1.2223
50	13.61	11.56	2.05	200.9	13.64	11.63	2.01	197	13.62	11.63	1.99	195	2.017	197.6	0.0249	2.4445

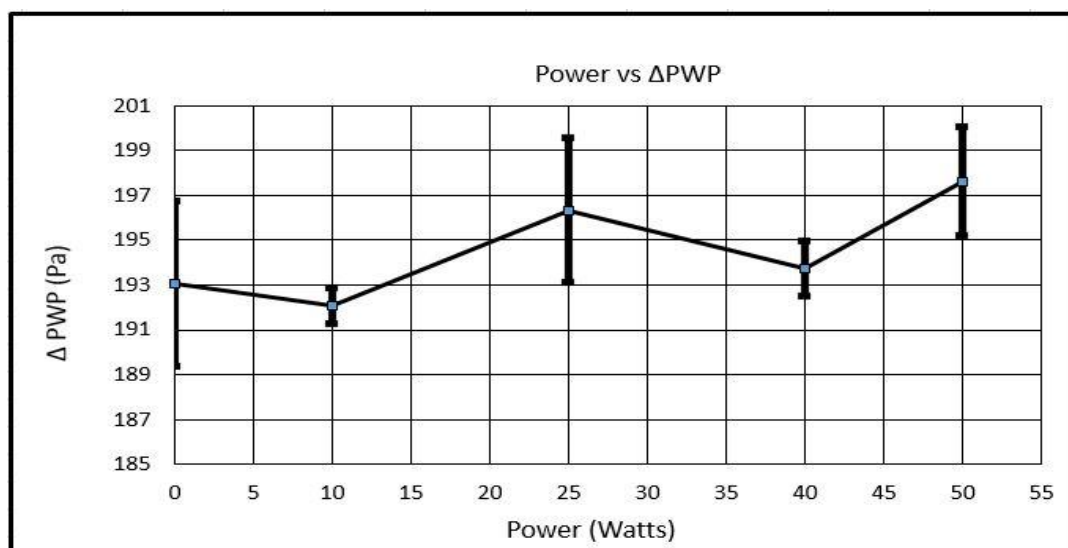


**Figure 25. Mean EPWP at various RF-power inputs at the RF frequency of 498 MHz**

At each power level in Figure 25, error bars are generated to show the variability of data at that power level. The error bars show how large a variability might occur. As seen in Figure 25, the EPWP at one power level is within the error limit of another power level. Hence, mean values at all RF-power levels are within the margin of error.

Table IV shows values of the effective stress at different RF-power levels at the point (at the center of the box, approximately at 11 cm below the top surface) where the pore-pressure transducer was installed. The table also contains the mean EPWP in cm and

Pa. From the EPWP and initial effective stress, excess pore-pressure ratio ( $r_u$ ) was then calculated. The value of  $r_u$  was within a range of 0.211 to 0.217. This means the soil was not completely liquefied because  $r_u$  should be 1 for the soil to completely liquefy at the depth of the pore-pressure transducer. However, partial liquefaction might have occurred at that depth. There was ponding of water on the surface of the soil, indicating that the liquefaction might have occurred near the surface. Though the applied impact did not completely liquefy the sample at the depth, the purpose of the study was to observe the EPWP in the presence of RF waves. As seen in Table IV, the mean EPWPs and  $r_u$  of the unstimulated test and RF-stimulated tests do not have a significant difference in the measurement.

**Table IV. Initial effective stress and excess pore-pressure ratio**

Power (Watts)	Effective stress ( $\sigma'$ ) (Pa)	MEAN EPWP (cm)	MEAN EPWP (Pa)	Excess pore pressure ratio ( $r_u$ )
0	911.75	1.97	193.06	0.212
10	911.75	1.96	192.08	0.211
25	911.75	2.00	196.33	0.215
40	911.75	1.98	193.71	0.213
50	911.75	2.02	197.63	0.217

RF-stimulated impact tests were also performed on the glass-bead sample at other frequencies. The implemented frequencies were 405, 485, 550, and 620 MHz. Figure 26 shows the variations of EPWP at various frequencies. The input RF power for the above-mentioned frequencies were maintained constant at 40 Watts. Results show that the

generation of EPWP is consistent except for the frequency of 620 MHz. The variation of the EPWP is, however, not large enough to be conclusive. The electric-field pattern at different frequencies are not similar within a cavity of constant size, and because of that, the electric field that is strong at one frequency near the place where the PWP transducer is installed may not be strong at other frequencies. In other words, in order to truly study the effect of RF frequency, the radiation pattern needs to be identical at various frequencies; this requires cavities of various sizes such that the same resonant mode (e.g., first resonant mode) is generated at all frequencies to perform the impact tests. This statement is further supported with the electric-field measurement and validation.

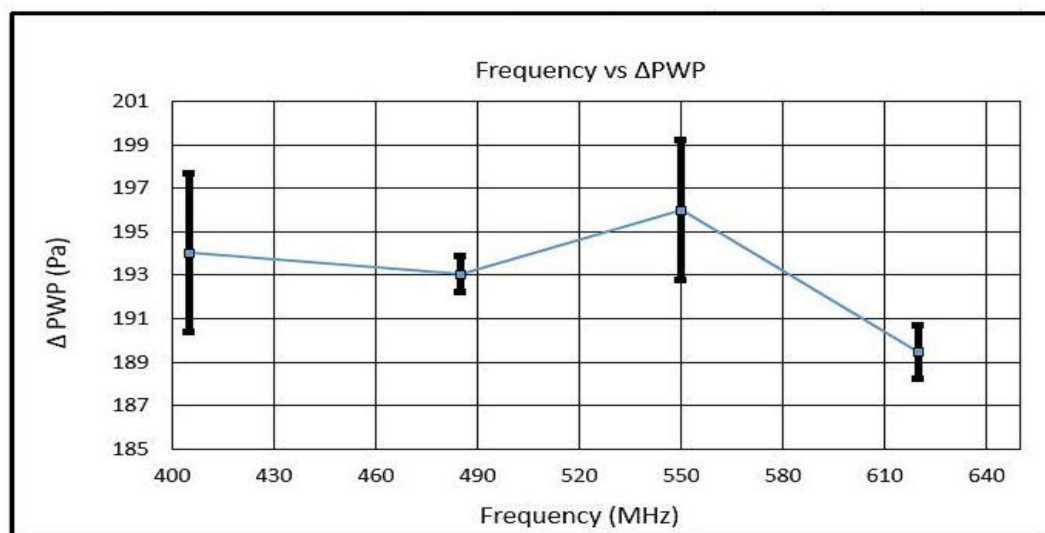


**Figure 26. Mean generated EPWP at different RF frequencies (RF-power input into the resonant cavity= 40 Watts)**

#### Electric-Field Measurement and Validation of Numerical Simulation

Before the start of RF-stimulated experiments, the electric fields' pattern was numerically simulated using the RF module of COMSOL model. However, the presence of the electric field inside the cavity can be validated by comparing experimentally-measured value of the Z component of the electric field to that obtained from COMSOL

model. This is because the vertically located monopole probe is vertically polarized, i.e., its measurement is dominated by the Z component of the electric field.

The experimental measurements were performed at two frequencies, 498 MHz and 632 MHz. As seen in Figure 27, the experimental measurements were performed near where the pore-pressure transducer was installed within the sample. The location of Slice 1 is +4 cm away from the transducer along the X axis, and Slice 2 is -4 cm along the X axis. Electric-field measurements were performed using a monopole probe inserted into the cavity through the top plate down to the desired depth. Figures 28(a) to 24(d) show the maps of the experimentally measured electric field and numerically simulated  $E_z$  on Slices 1 and 2. Electric-field measurements are normalized to the maximum electric field measured on the corresponding slice.

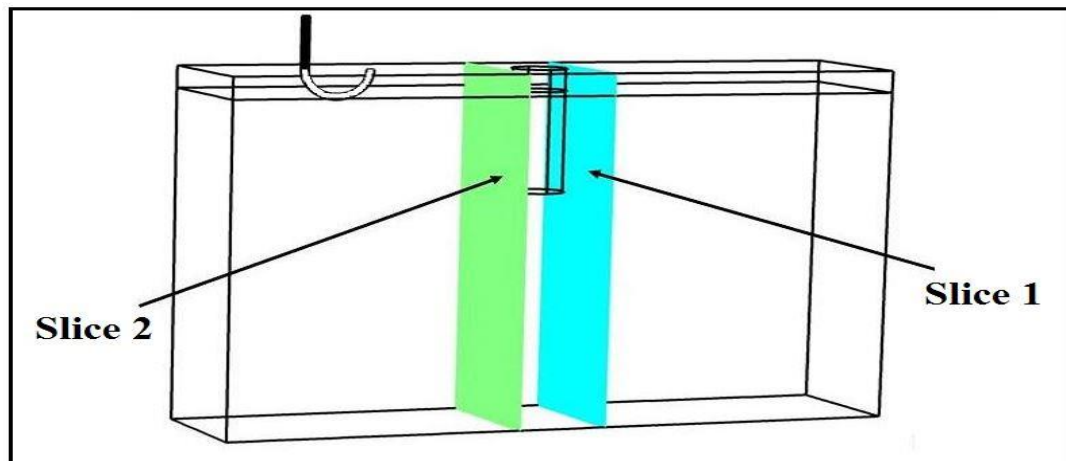


**Figure 27.** Schematic of the location of depth of (vertical) slices in 3-D view

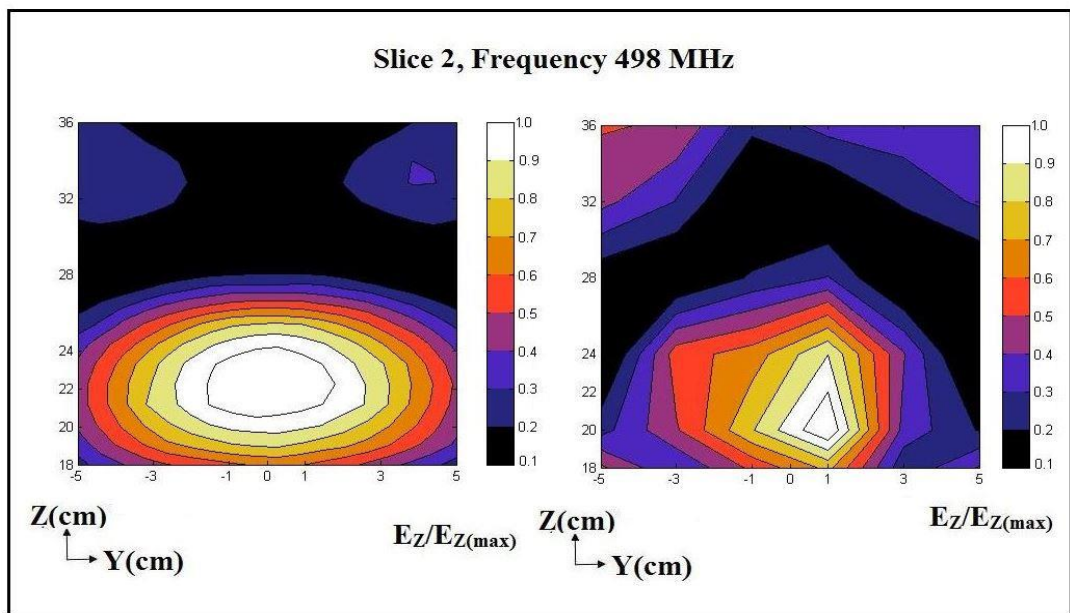
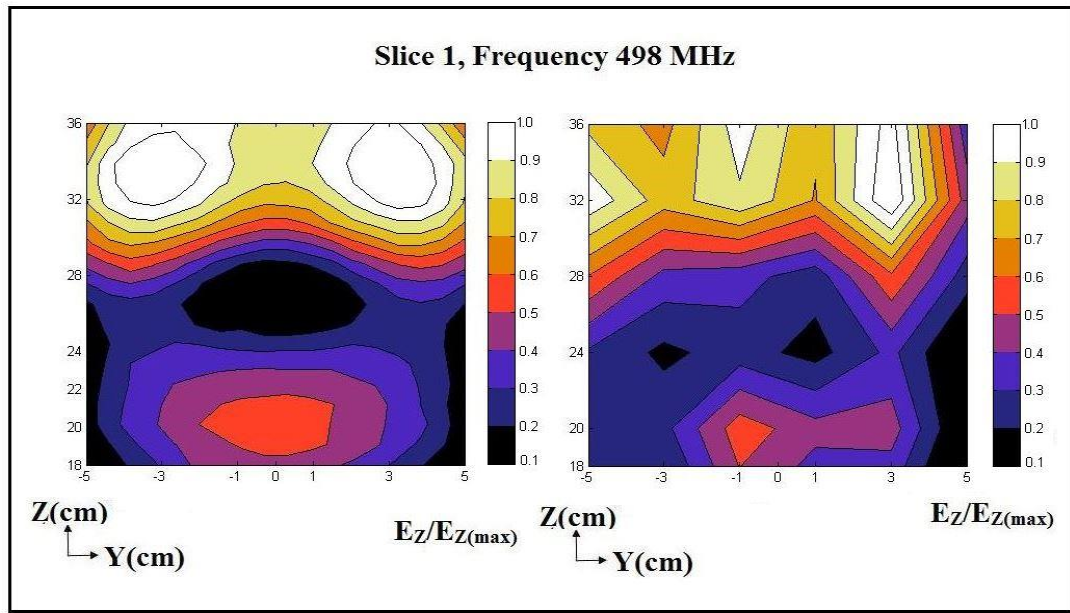


**Figure 28. Electric field: experimentally measured (right) and numerically simulated using COMSOL Multiphysics (left) at 498 MHz on within glass-bead sample: a) Depth Slice1; and b) Depth Slice 2**



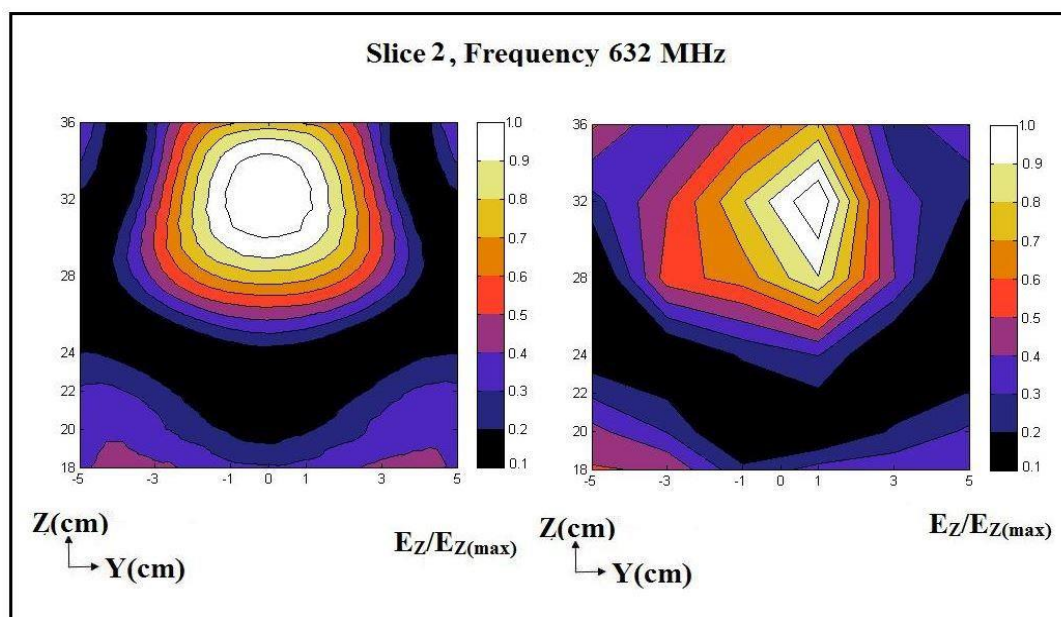
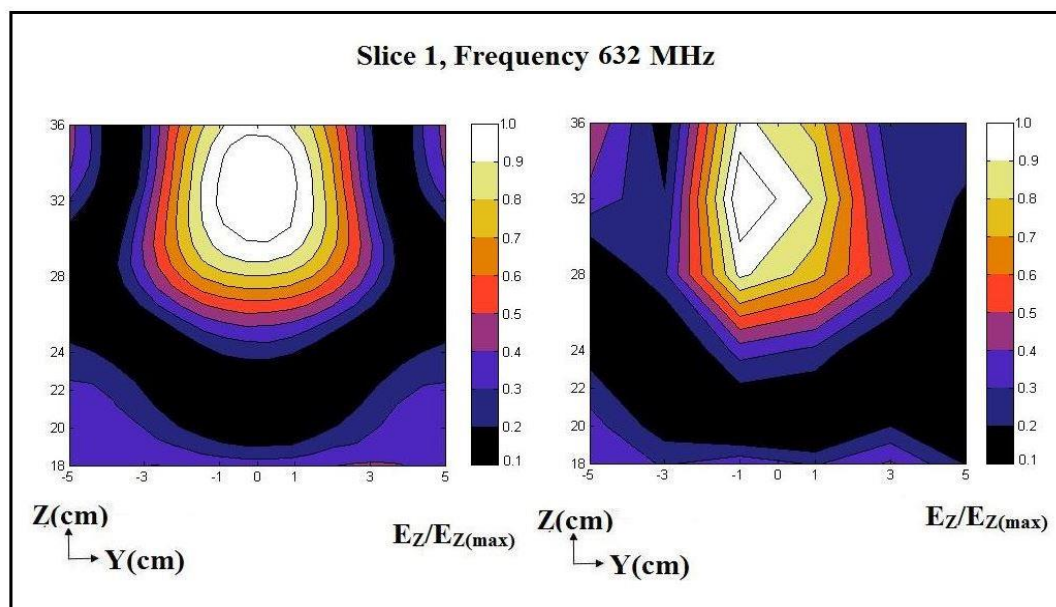


**Figure 28 (Contd.). Electric field: experimentally measured (right) and numerically simulated using COMSOL Multiphysics (left) at frequency 632 MHz within glass-bead sample: c) Depth Slice 1; and d) Depth Slice 2**

It can be observed in Figure 28 that the experimentally measured and numerically simulated electric fields reasonably agree. Since the monopole probe is not calibrated, the

experimentally measured electric field does not represent the actual strength of the electric field within the cavity and just represents the electric field pattern. Both numerically simulated and experimentally measured electric-field patterns have their maximum at similar depths, i.e., the predesigned location of the pore-pressure transducer.

As mentioned, strength of the electric field at any specific location depends on the frequency of RF waves launched. Effects of RF waves on physical properties such as viscosity of water may not be linear due to having different field pattern at different frequencies. Hence, a change in any physical property may not be linearly correlated with an increase or decrease of a frequency.

### **Series 2: Hydraulic-Conductivity Tests**

Because no effect was observed in the EPWP generation due to RF waves' application, RF waves' effect on hydraulic conductivity at different combinations of frequency and powers level needs to be studied. At first, hydraulic-conductivity tests were performed on the glass-bead samples. For each type of sample, both unstimulated and RF-stimulated tests were performed. At first, unstimulated tests were performed using both the standard permeameter and customized permeameter to calibrate the customized permeameter.

Figure 29 shows the measurement of the unstimulated hydraulic conductivity of the glass-bead sample performed using a standard permeameter. The test was run for four hours. Hydraulic-conductivity values remained fairly constant during the entire run of the test. The average unstimulated hydraulic conductivity of the glass-bead sample was measured to be  $1.391 \times 10^{-2}$  cm/s.



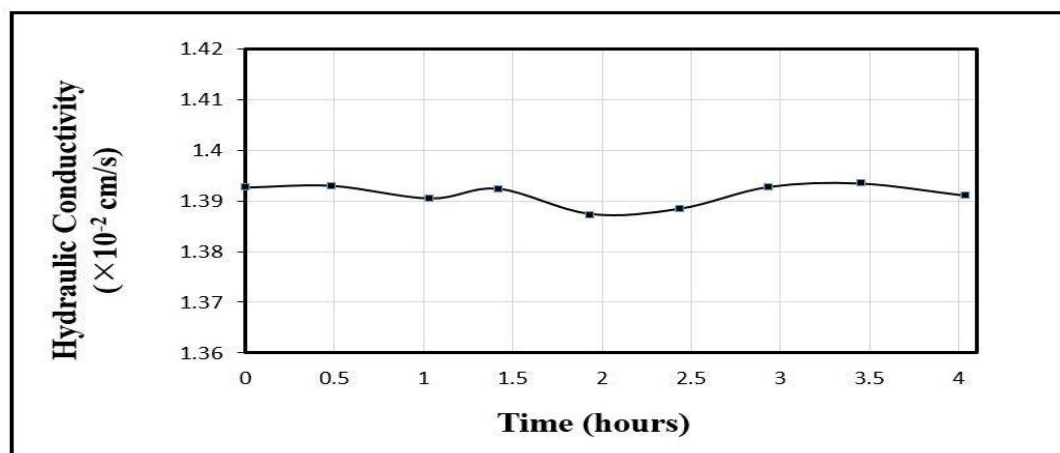
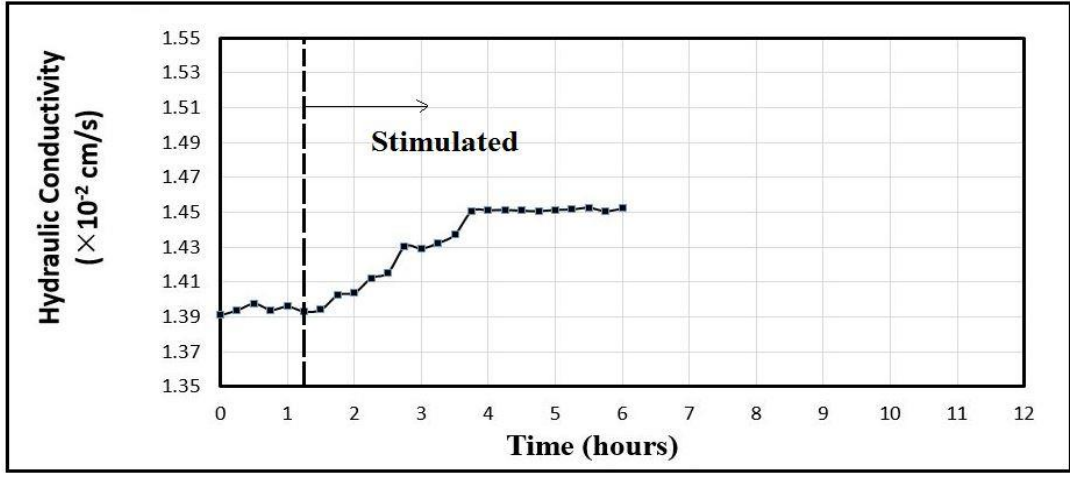


**Figure 29. Measured unstimulated hydraulic conductivity of glass-bead sample**

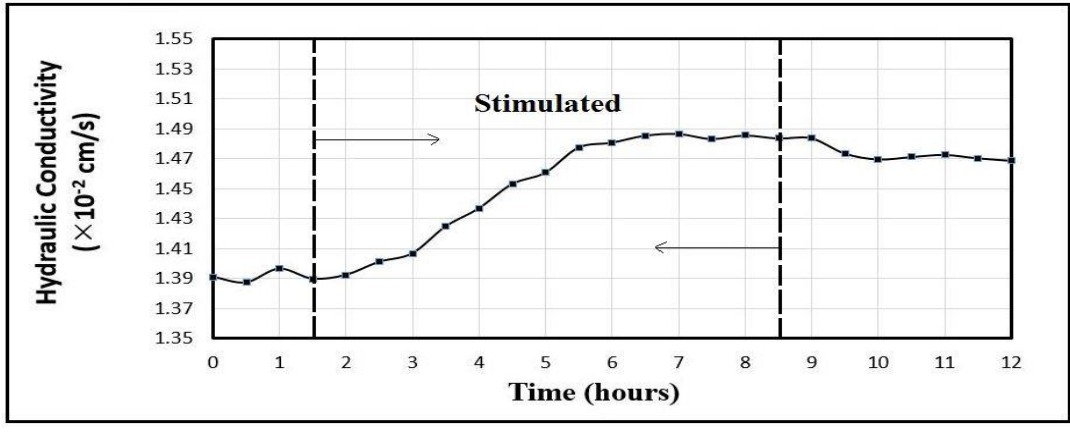
A series of RF-stimulated hydraulic-conductivity tests were conducted on the glass-bead sample in the customized permeameter. There was a discrepancy of 3.5% between the customized permeameter and standard permeameter. The discrepancy was calibrated out. To calibrate the customized permeameter, the hydraulic-conductivity measurements obtained were multiplied with a multiplication factor = 1.035.

The RF-stimulated tests were then conducted at a frequency of 726 MHz and RF-power levels of 10, 25, and 40 Watts. Before the application of RF waves, tests were run for at least one hour to distinguish the trend of hydraulic-conductivity change after the RF stimulation. Figure 30 shows the hydraulic-conductivity measurements at different RF-power levels. There was no sharp increase in the hydraulic conductivity with the RF stimulation. However, the hydraulic conductivity started to increase gradually with time and eventually attained a peak value. As seen in Figure 30(a), at the RF-power level of 10 Watts, hydraulic conductivity started to increase from  $1.3942 \times 10^{-2}$  cm/s to a peak value of  $1.452 \times 10^{-2}$  cm/s after two hours and 30 minutes and remained constant thereafter. Similar changes were observed at other RF-power levels of 25 Watts and 40 Watts. At the RF-power level of 25 Watts, the RF stimulation was terminated once the RF-

stimulated hydraulic conductivity reached its maximum. After the termination of RF waves, the hydraulic conductivity slightly decreased with time and then stabilized at a smaller value, but was still larger than the unstimulated value.

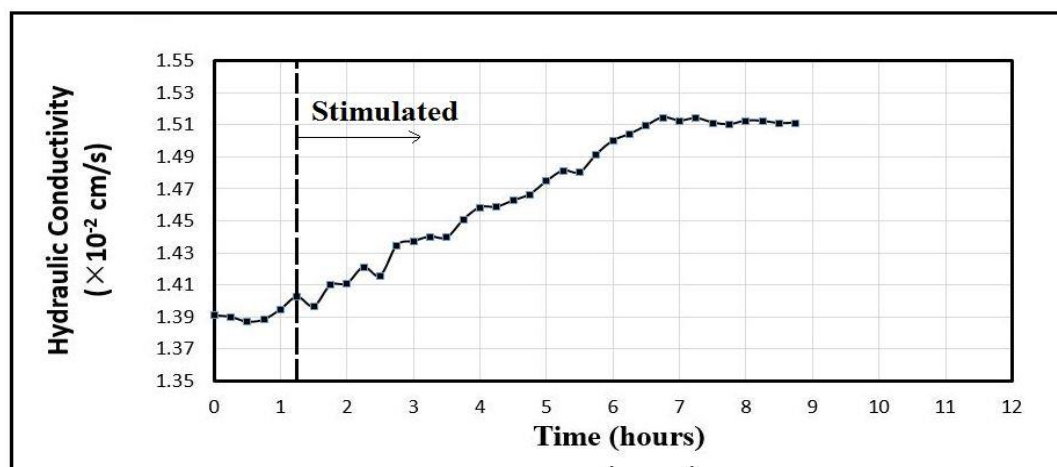


(a)



(b)

**Figure 30. Measured RF-stimulated hydraulic conductivity of glass-bead sample at a frequency of 726 MHz and RF-power levels of: a) 10 Watts; and b) 25 Watts**



(c)

**Figure 30 (Contd.). Measured RF-stimulated hydraulic conductivity of glass-bead sample at a frequency of 726 MHz and RF-power level of c) 40 Watts**

The average unstimulated hydraulic conductivity before the start of RF stimulation and the peak value of the RF-stimulated hydraulic conductivity are compared in Table V. As seen in Table V, the hydraulic conductivity increased with the increase in the RF input power. The increase in the hydraulic conductivity was, however, small compared to the result obtained by Azad (2013).

**Table V. Hydraulic-conductivity measurements of glass-bead sample at a frequency of 726 MHz and different RF-power levels.**

Power (Watts)	Average of unstimulated hydraulic conductivity measured before RF-stimulation, $k$ (cm/s)	RF-Stimulated Hydraulic Conductivity, Peak value, $k'$ (cm/s)	Percent Change (%)
10	$1.3942 \times 10^{-2}$	$1.452 \times 10^{-2}$	(+) 4.190%
25	$1.3911 \times 10^{-2}$	$1.482 \times 10^{-2}$	(+) 6.864%
40	$1.3923 \times 10^{-2}$	$1.514 \times 10^{-2}$	(+) 8.774%

The effect of RF waves on hydraulic conductivity was smaller in glass beads than that of Azad's (2013) for natural sand. Hence, a new set of RF-stimulated hydraulic-conductivity tests were performed on the natural-sand sample. Unstimulated hydraulic-conductivity tests were first performed on the natural-sand sample in the standard permeameter for calibration purposes. Figure 31 shows the measurement of unstimulated hydraulic conductivity of the natural-sand sample performed using the standard permeameter. The average unstimulated hydraulic conductivity of the natural-sand sample was measured to be  $0.7924 \times 10^{-2}$  cm/s.

A series of RF-stimulated hydraulic-conductivity tests were then conducted on the natural-sand sample in the customized permeameter. There was a discrepancy of 5.1% between the customized and standard permeameters, which was later calibrated out. RF-stimulated tests were performed at a frequency of 726 MHz and RF-power levels of 10, 25, and 40 Watts. The conducted tests were similar to the RF-stimulated hydraulic-conductivity tests carried out on glass beads. Figure 32 shows the hydraulic-conductivity measurements at different RF-power levels. The results show a similar pattern of the change in hydraulic-conductivity. After RF stimulation started, the hydraulic conductivity of sand started to increase gradually with the time and attained a peak value. At an RF-power level of 10 Watts, the hydraulic conductivity started to increase from  $0.7933 \times 10^{-2}$  cm/s, reached to a peak value of  $0.881 \times 10^{-2}$  cm/s after four hours, and remained constant thereafter. Similar changes were observed at other input powers, i.e., 25 Watts and 40 Watts. At the RF-power level of 25 Watts, RF stimulation was terminated once the RF-stimulated hydraulic conductivity reached its maximum and stabilized. After the

termination of RF waves, the hydraulic conductivity of sand decreased with time and then stabilized at a slightly smaller value, yet much larger than the original unstimulated one.

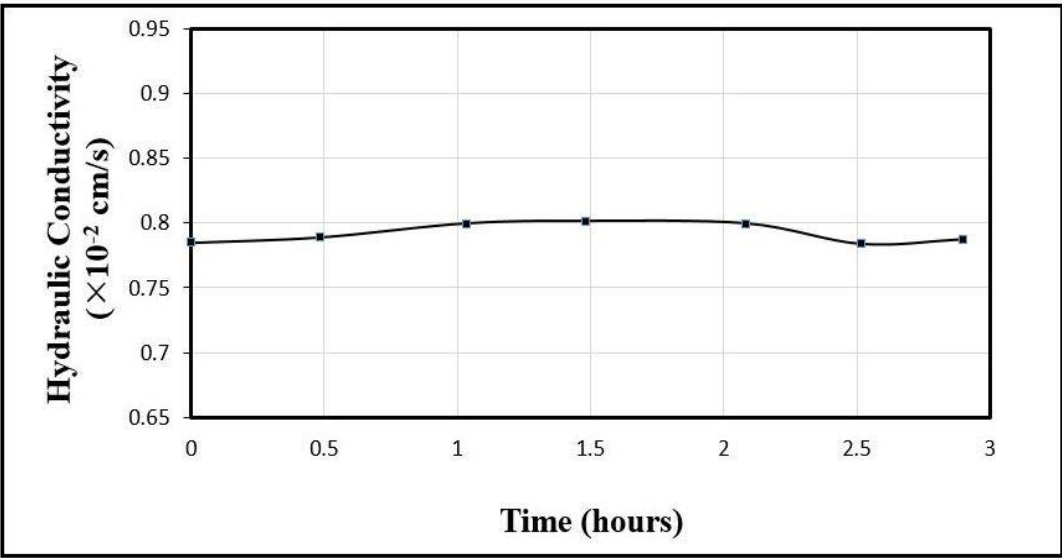
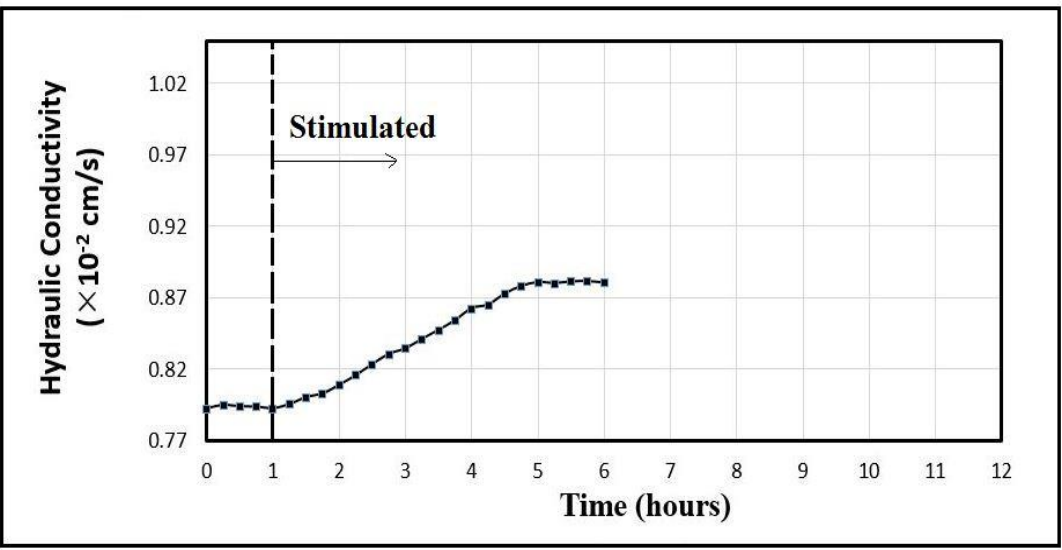
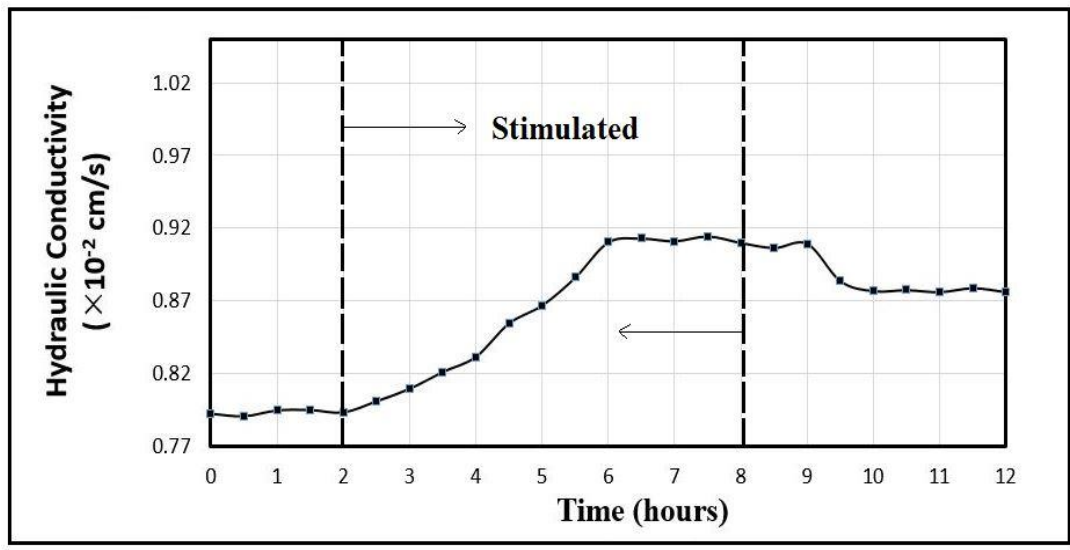


Figure 31. Measured unstimulated hydraulic conductivity of natural-sand sample

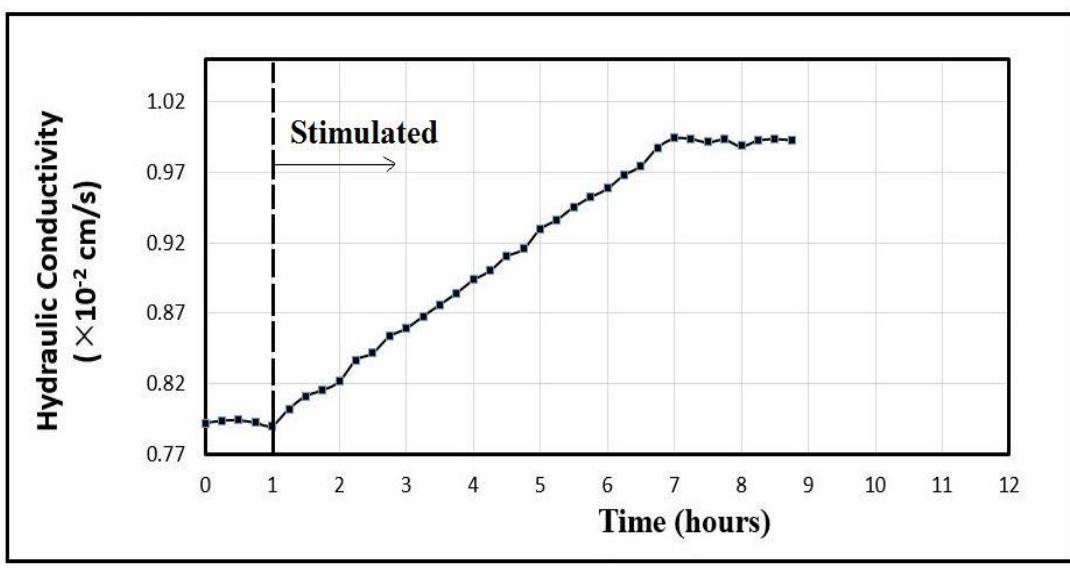


(a)

Figure 32. Measured RF-stimulated hydraulic conductivity of natural-sand sample at a frequency of 726MHz and RF-power levels of: a) 10 Watts



(b)



(c)

Figure 32 (Contd.). Measured RF-stimulated hydraulic conductivity of natural-sand sample at a frequency of 726MHz and RF-power levels of: b) 25 Watts; and c) 40 Watts

**Table VI. Hydraulic-conductivity measurements of natural-sand sample at a frequency of 726 MHz and different RF-power levels.**

<b>RF Power (Watts)</b>	<b>Average of measured unstimulated hydraulic-conductivity values, <math>k</math> (cm/s)</b>	<b>RF-Stimulated Hydraulic Conductivity, Peak Value, <math>k'</math> (cm/s)</b>	<b>Percent change (%)</b>
10	$0.7933 \times 10^{-2}$	$0.881 \times 10^{-2}$	(+) 11.091%
25	$0.7932 \times 10^{-2}$	$0.915 \times 10^{-2}$	(+) 15.287%
40	$0.7928 \times 10^{-2}$	$0.994 \times 10^{-2}$	(+) 25.386%

The percent change in the hydraulic conductivity of natural sand due to RF stimulation is larger than that of the glass bead for all input RF-power levels. The results, however, show the similar pattern of increase and decrease in the hydraulic conductivity of both sand and glass beads during the application and termination of the RF stimulation, respectively.

Even though the effect of RF waves on natural sand was larger compared to glass beads, impact tests were not performed for the natural-sand sample because the peak value of the hydraulic conductivity was observed after several (4-6) hours after the start of the test. Increase in the hydraulic conductivity was also slow and gradual. With the test setup that can only provide up to 50 Watts of RF power, RF stimulation would not be able to change the EPWP promptly, even for natural sand. To observe the effect on EPWP, the increase in hydraulic conductivity has to be abrupt, and with the available test setup, it was improbable to observe such a change. Therefore, the impact test on natural sand was not performed.

### Electric-Field Measurement and Comparison

Similar to impact tests, the experimental measurements of the electric-field pattern for the RF-stimulated tests were performed at two frequencies, 710 MHz and 726 MHz. The location of Slices 1 and 2 along the X axis are  $x_1 = +2$  cm and  $x_2 = -4$  cm. The measurements of the electric field were performed using the monopole probe protruded into the sample down to the desired depth through holes drilled into the top of the smapel. Figure 34 shows the contour maps of the experimentally measured electric filed and numerically simulated  $E_z$  on Slices 1 and 2. The electric field is normalized to its maximum on the corresponding slice.

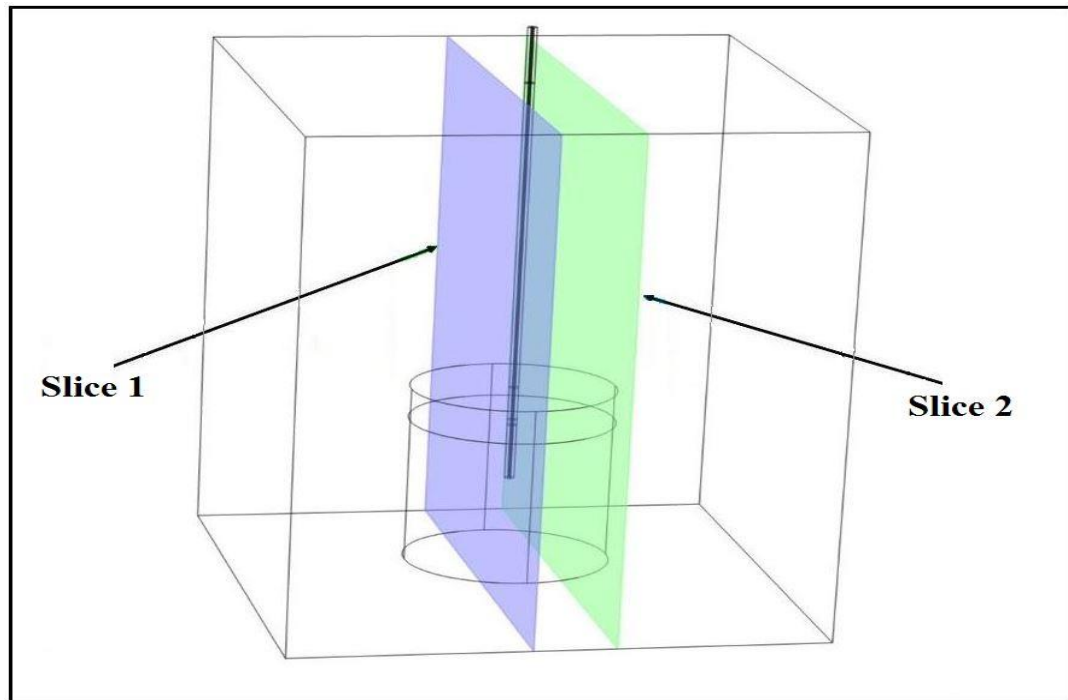
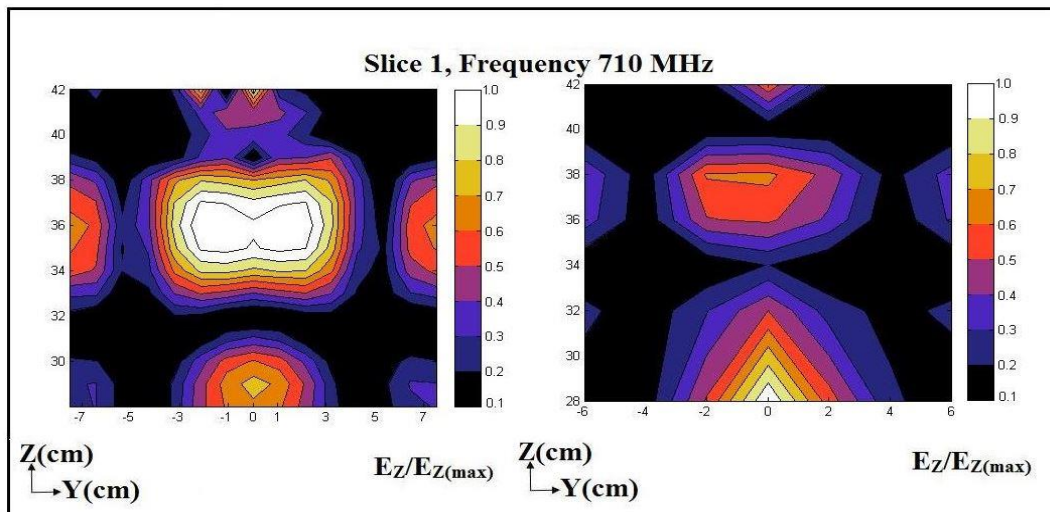
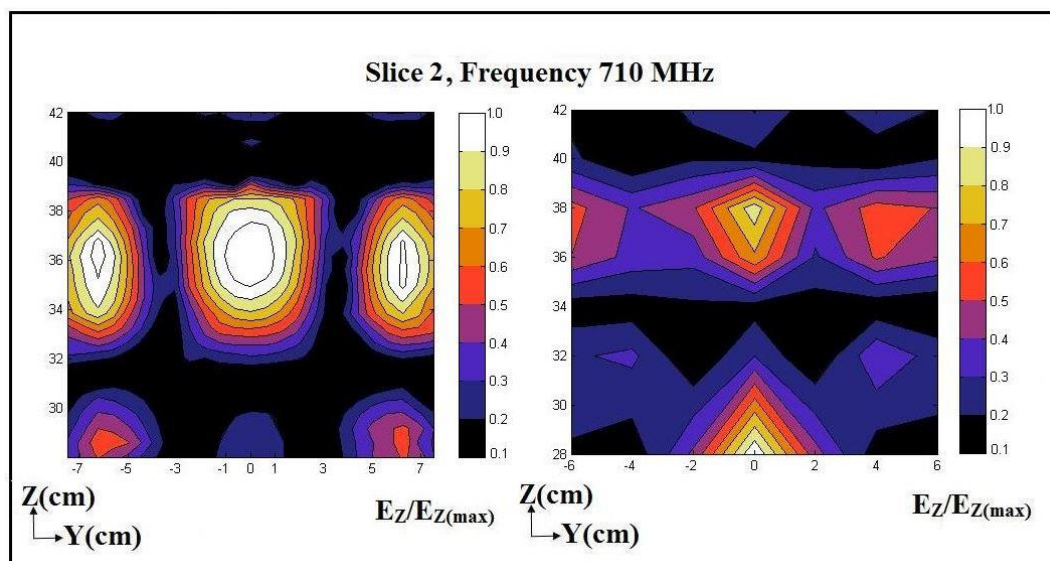


**Figure 33. Schematic of the location of Slices 1 and 2 in 3D view**



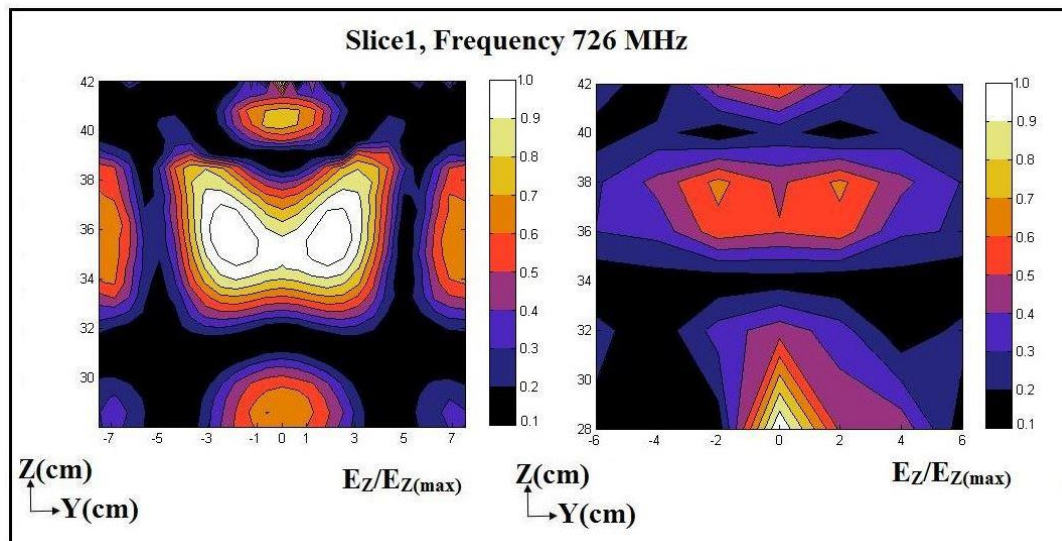


(a)

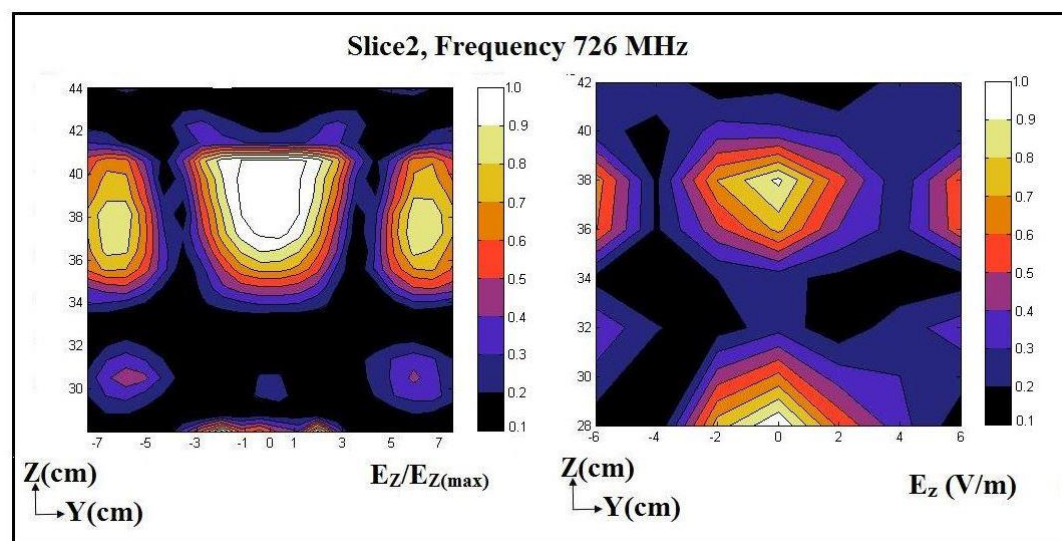


(b)

**Figure 34.** Electric field, experimentally measured (right) and numerically simulated using COMSOL Multiphysics (left) within glass bead sample on: a) Depth Slice 1, frequency = 710 MHz; b) Depth Slice 2, frequency = 710 MHz



(c)



(d)

**Figure 34(Contd.). Electric field, experimentally measured (right) and numerically simulated using COMSOL Multiphysics (left) within glass bead sample on: c) Depth Slice 1, frequency = 726 MHz; d) Depth Slice2, frequency = 726 MHz**

As seen in Figure 34, the patterns of both numerically simulated and experimentally measured electric fields reasonably match each other. As mentioned, since the monopole probe is not calibrated, the experimentally measured electric-field measurements do not represent the actual intensity of the electric field within the cavity.

The intensity of the electric field at any specific location depends on the frequency of RF waves launched. The effect of RF waves on physical properties such as viscosity of water may not be linear due to having different electric-field pattern at different frequencies. Hence, the change in any physical property may not be linearly correlated with the change in the frequency.

### **Seepage-Flow Numerical Simulation**

The aim of this section is to understand the effect of RF waves on hydraulic conductivity. The section consists of the development of a forward model (i.e., a finite-difference numerical simulation developed in MATLAB) of seepage flow for the unstimulated and RF-stimulated hydraulic-conductivity tests. After the forward model was developed, it was validated against experimental results by comparing the computed and measured total discharge values. The theory behind seepage flow, its boundary conditions, and domain discretization were presented and explained in Chapter 3.

The unstimulated seepage-flow model was developed based on the hydraulic-conductivity value of the unstimulated test performed in the lab. The model in MATLAB interface was used to compute the spatial variations of hydraulic head within the soil. As mentioned in Chapter 3, to address the discrepancy due to the assumption of the rectangular domain, the heads of the nodes outside the circumference of the circle were considered to be zero, and an impermeable wall was modeled surrounding the cylindrical domain of the soil. Moreover, numerically computed flow discharge was obtained and compared to the experimental value. Figure 35 shows the schematic of the top view of the forward-model domain, discretized nodes, and the location of slices where the hydraulic

head was computed. The forward model (i.e., MATLAB programming code) for the unstimulated seepage flow is included in Appendix B.

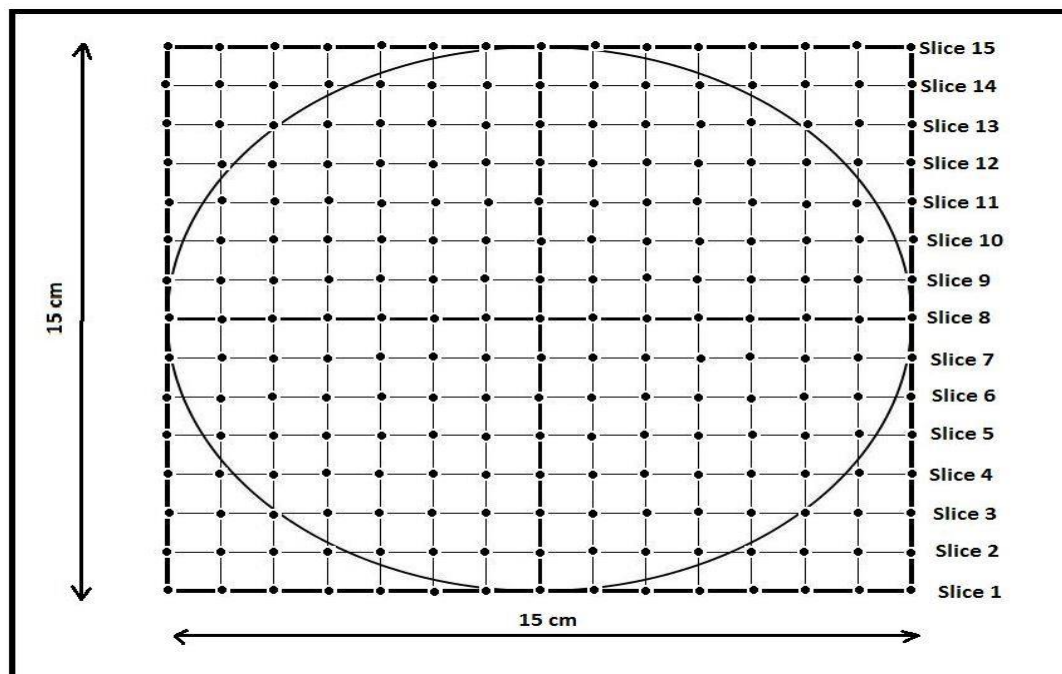
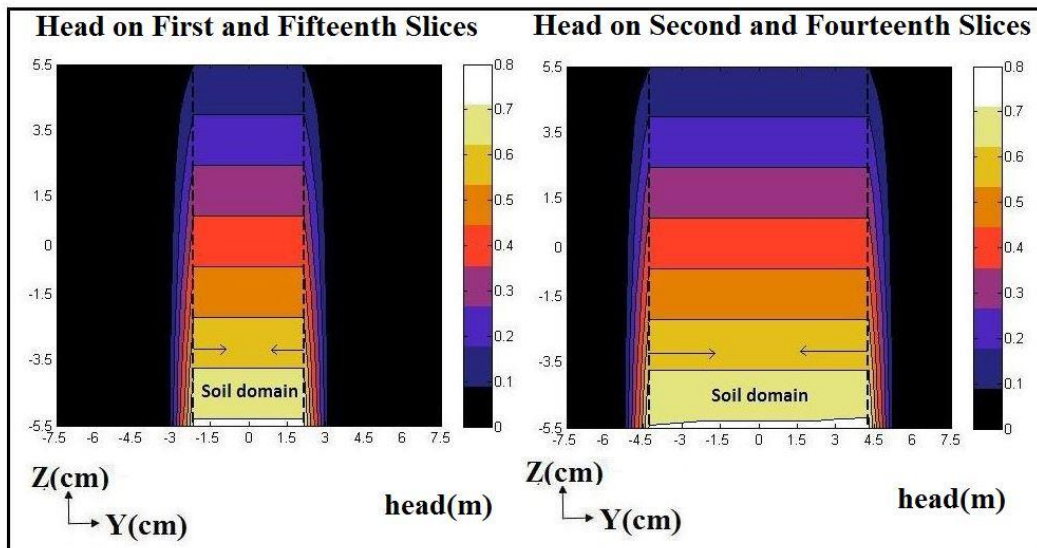
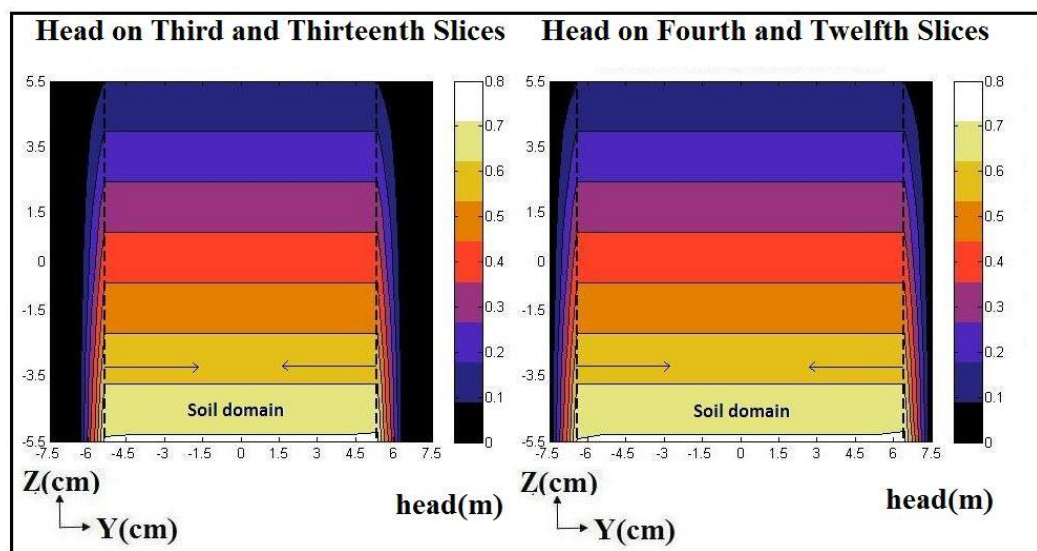


**Figure 35. Schematic of top-view of the discretized rectangular cubical domain**

Figure 36 shows the contour maps of the hydraulic head on 15 different vertical slices within the sandy sample obtained using the forward model for the unstimulated test. As seen in Figure 36, the hydraulic head decreased gradually and uniformly from the bottom to the top indicating the existence of uniform gradient along the soil specimen and an upward uniform flow within the homogeneous sand sample.



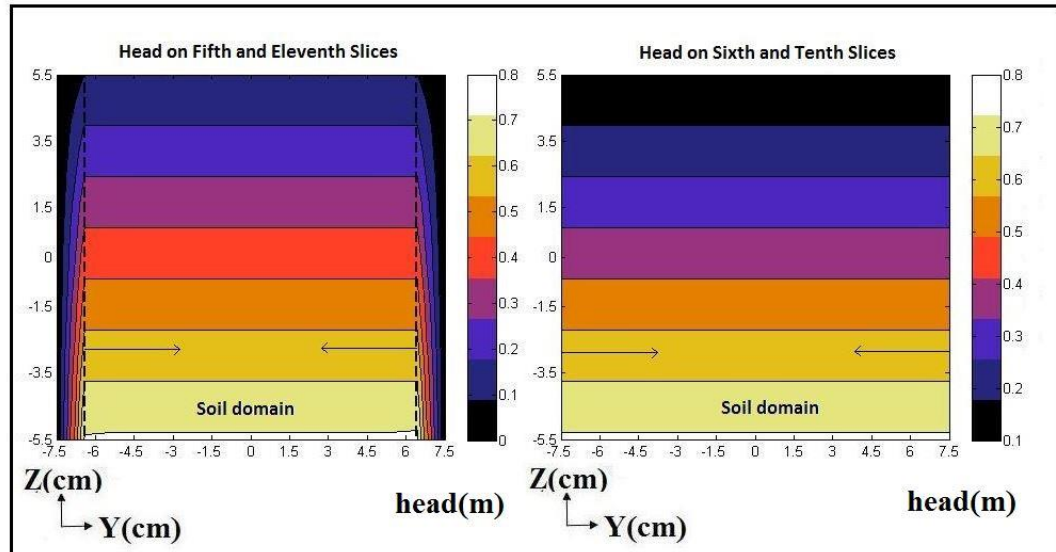
(a)



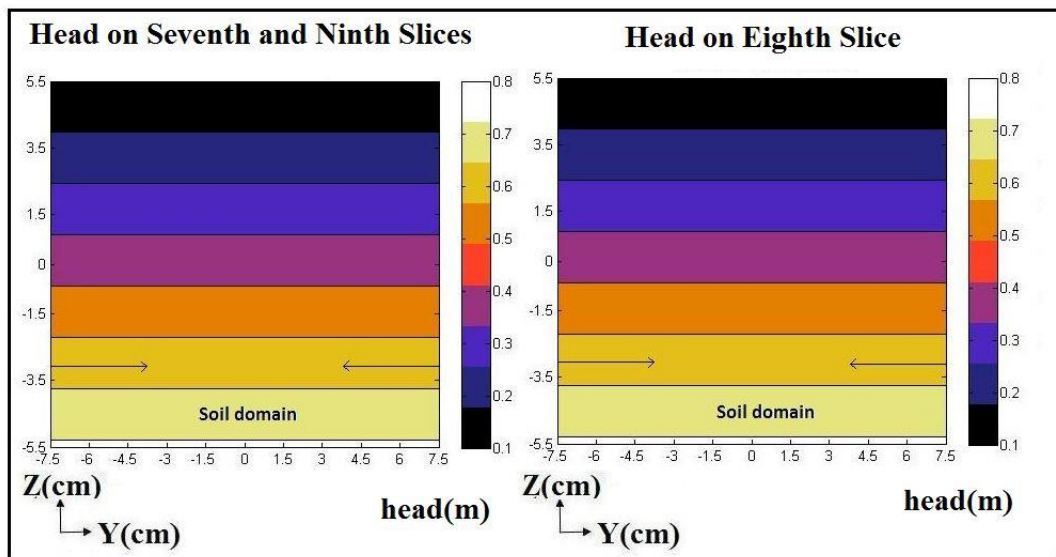
(b)

Figure 36. Contour/color maps of hydraulic head (m) within natural-sand specimen for unstimulated flow on depth slices: a) 1 and 15, and 2 and 14; b) 3 and 13, and 4 and 12





(c)



(d)

**Figure 36 (Contd.).** Contour/color maps of hydraulic head (m) within natural-sand specimen for unstimulated flow on depth slices: c) 5 and 11, and 6 and 10; d) 7 and 9, and Slice 8

To observe the flow-velocity vector field within the soil specimen, velocity vectors on Slice 7 are plotted in Figure 37. As seen in Figure 37, the horizontal component of the flow velocity is zero, while its vertical component is nonzero. The flow

along the horizontal direction within the soil specimen was not restricted except at the boundaries. In addition, the equal length of these vectors indicates the uniform flow of water through the specimen.

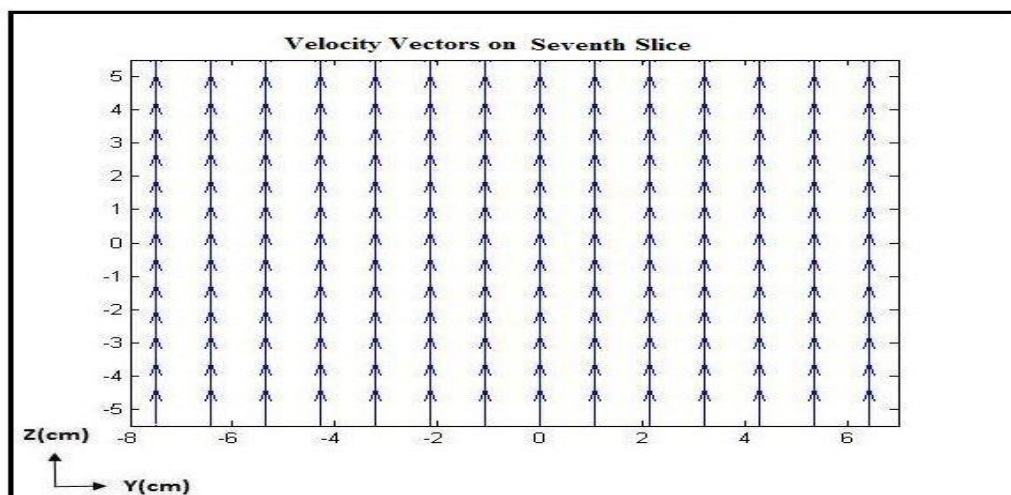


**Figure 37. Velocity vector plot within natural-sand specimen on Slice 7 for unstimulated test**

The experimentally measured flow discharge in the natural-sand sample during unstimulated tests was  $9.34 \times 10^{-6} \text{ m}^3/\text{s}$ . In addition, the finite-difference forward model was used to compute the flow discharge to be  $9.23 \times 10^{-6} \text{ m}^3/\text{s}$ . There is a small discrepancy of 1.18% between the experimental and numerical value, and the difference is due to the approximation of the cylindrical walls of the permeameter using a stepwise rectangular cubical wall.

In order to understand the RF stimulation effect on hydraulic conductivity, the increase in the hydraulic conductivity due to RF waves should be correlated with the RF-power level. The RF-power density at each node was obtained from the RF forward model generated using COMSOL Multiphysics. The RF power densities in the form of a 3D matrix were exported into MATLAB interface. Afterwards, an inverse model was

developed to solve the inverse problem of finding the relation between RF power and hydraulic conductivity. The inverse model uses an optimization scheme developed in this thesis to find the presumed relation ( $k' = k + \beta \cdot \sqrt{P}$ ) between RF power and hydraulic conductivity. The optimization scheme was used to find the slope ( $\beta$ ) of the linear relation that minimizes a cost function (also known as objective function) equal to the difference between the numerically simulated and experimentally measured RF-stimulated discharge,  $Q_{sim,st}$  and  $Q_{exp,st}$ , respectively. Table VII shows the experimental flow discharge, numerically computed flow discharge, and slope ( $\beta$ ) at a frequency of 726 MHz and RF-power levels of 10, 25, and 40 Watts. Similarly, the experimentally measured and numerically computed flow discharge with respect to the RF-power levels are plotted in Figure 38. Using the optimization scheme, the cost function was minimized to less than 3%, indicating the numerically computed values reasonably matching the experimental values. In addition, the value of  $\beta$  at all three power levels are nearly identical.

**Table VII. Experimentally measured and numerically computed flow discharge in the natural sand at various RF-power levels**

RF Input Power (Watts)	$Q_{exp,st}$ ( $m^3/s$ ) (Experimental)	Slope ( $\beta$ ) (Numerical simulation)	$Q_{sim,st}$ ( $m^3/s$ ) (Numerical value based on optimized $k'$ )	Cost Function ( $(Q_{exp,st} - Q_{sim,st}) / Q_{exp,st} \times 100\%$ )
0	$9.34 \times 10^{-6}$	None	$9.23 \times 10^{-6}$	1.18%
10	$10.39 \times 10^{-6}$	$3.65 \times 10^{-8}$	$10.11 \times 10^{-6}$	2.77%
25	$10.78 \times 10^{-6}$	$3.25 \times 10^{-8}$	$10.52 \times 10^{-6}$	2.47%
40	$11.71 \times 10^{-6}$	$3.25 \times 10^{-8}$	$11.42 \times 10^{-6}$	2.54%



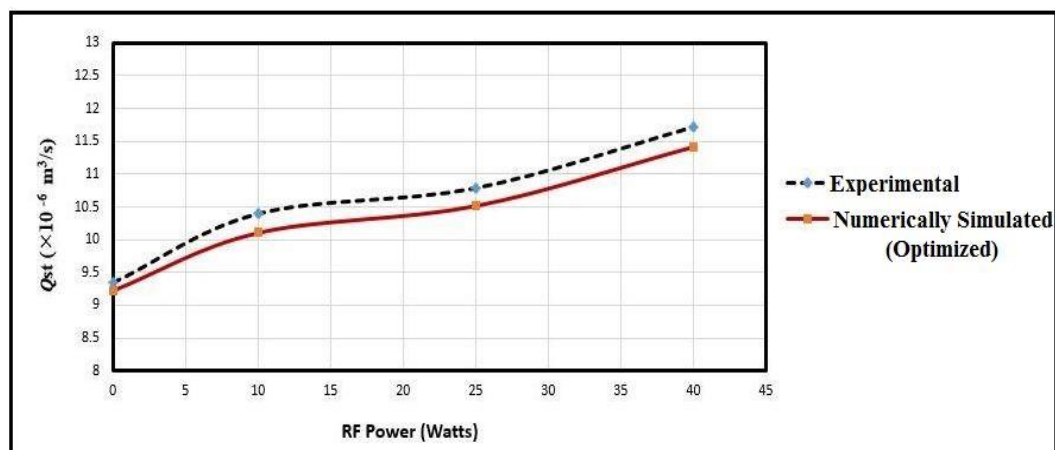
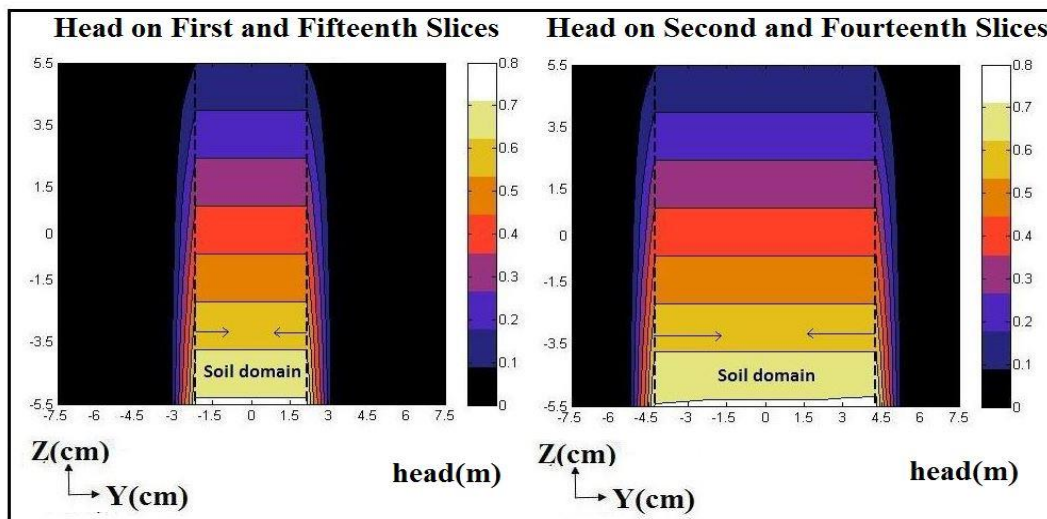


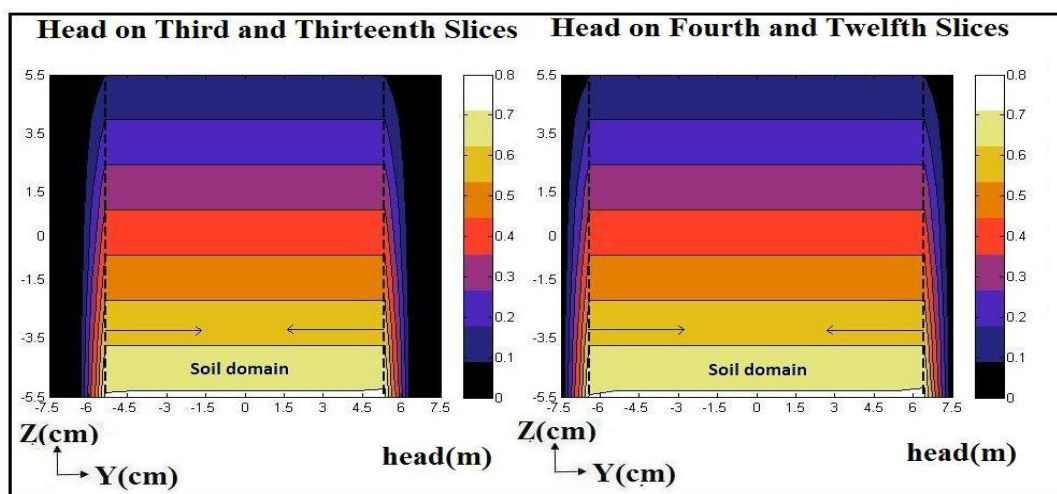
**Figure 38. RF power vs RF-stimulated flow rate in the natural-sand specimen at a frequency of 726 MHz**

Similar to unstimulated tests, hydraulic heads were computed for RF-stimulated tests. The hydraulic heads were computed using the inverse model after the optimization was completed. As the optimization was completed, the optimized flow discharge, optimized hydraulic conductivity, and optimized hydraulic heads were obtained. Figure 39 shows the contour/color maps of the hydraulic heads obtained from the inverse model at a frequency of 726 MHz and RF-power level of 25 Watts. Similar to the unstimulated case, the contour/color maps show the uniform decrease in the hydraulic head from the bottom to the top, indicating an upward flow. There was a spatially variable alteration in the hydraulic conductivity in X, Y, and Z directions, which is a function of the spatially variable electric-field power density in X, Y, and Z directions. This resulted in a change in the hydraulic head within the soil specimen due to RF-waves application, which is uniform along X and Y directions and only varies along Z direction. However, the change is uniform and does not manifest as a distortion in the contour/color maps of the hydraulic head. In other words, even though the spatially variable electric field in X, Y, and Z directions results in a spatially variable hydraulic conductivity field in X, Y, and Z

directions, the hydraulic head variation is only in the Z direction, and the pattern of variations of the hydraulic head looks similar to the unstimulated case.

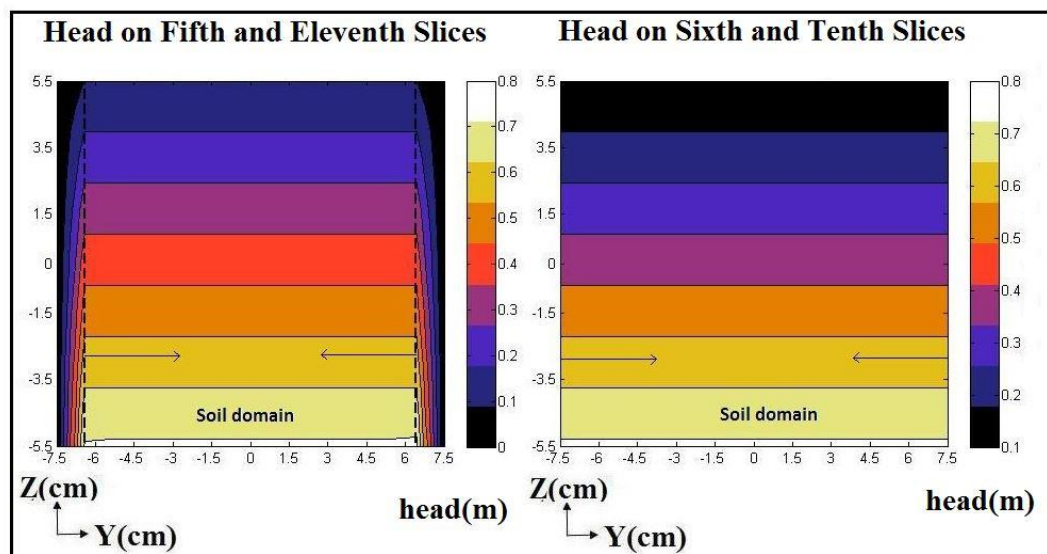


(a)

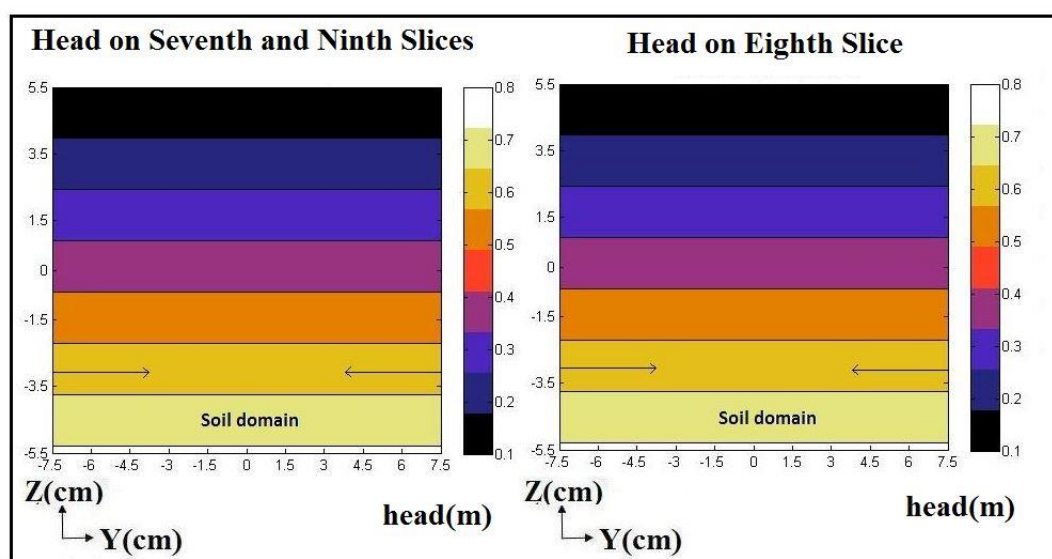


(b)

**Figure 39.** Contour/color maps of hydraulic head (m) for natural-sand specimen on depth slices: a) 1 and 15, and 2 and 14, at a frequency of 726 MHz and RF-power level of 25 Watts; b) 3 and 13, and 4 and 12, at a frequency of 726 MHz and RF-power level of 25 Watts.



(c)



(d)

**Figure 39 (Contd.).** Contour/color maps of hydraulic head (m) within the natural-sand specimen on depth slices: c) 5 and 11, and 6 and 10, at a frequency of 726 MHz and RF-power level of 25 Watts; d) 7 and 9, and 8, at a frequency of 726 MHz and RF-power level of 25 Watts.

Velocity vectors on Slice 7 are also plotted for the RF-stimulated case in Figure 40. As seen in Figure 40, the velocity along the horizontal direction is still zero and has only a vertical component. The flow along the horizontal direction within the soil

specimen was not restricted except at the boundaries. In addition, as seen in Figure 40, the length of velocity vectors is spatially variable and not uniform everywhere. This is because—despite the uniform change in hydraulic head—the RF-stimulated hydraulic conductivity follows the same spatially variable pattern as that of the electric-field power density. This, in turn, results in a flow-velocity vector field that has the same spatially variable pattern as that of the electric field. The spatial variations in the lengths of velocity vectors are small and visible but not clearly visible in Figure 40. The contour map of the flow velocity in Figure 41 confirms the spatial variation of the flow velocity on the seventh slice. It follows the same pattern as that of the electric-field power density shown in Figure 39.

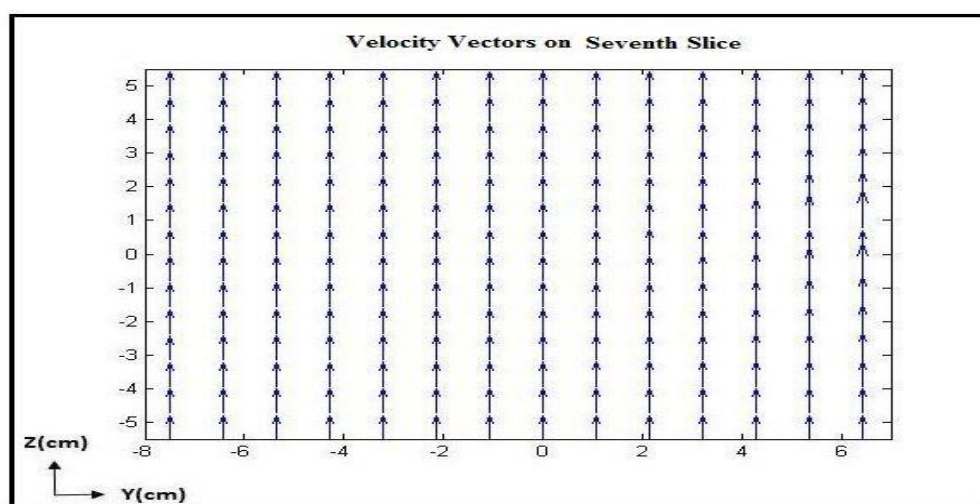


**Figure 40.** Vector plot for the numerically simulated RF-stimulated flow velocity within the natural-sand specimen on Slice 7 at a frequency of 726 MHz and power level of 25 Watts.

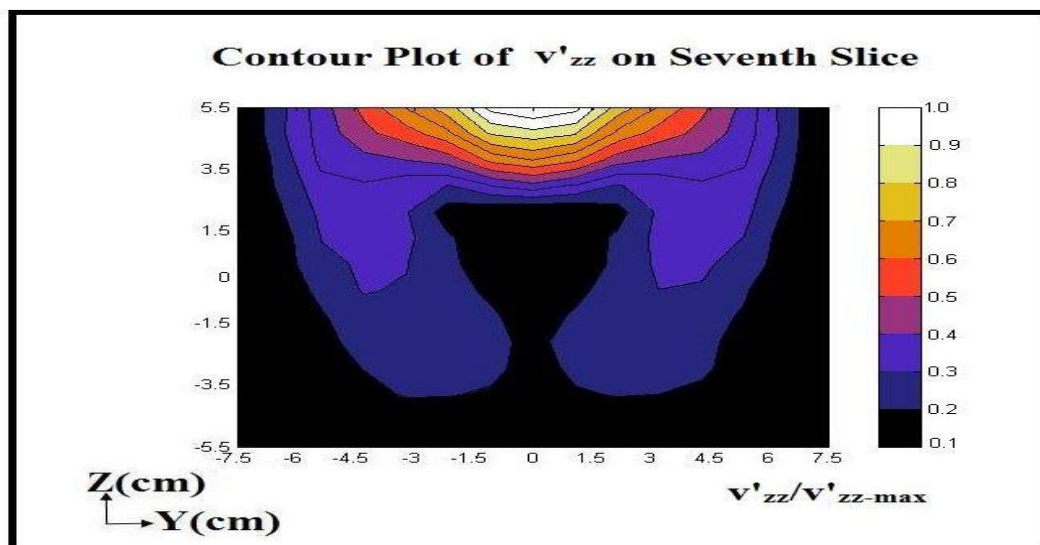


**Figure 41.** Contour/color maps of normalized vertical component of numerically simulated RF-stimulated flow velocity within the natural-sand specimen on Slice 7 at a frequency of 726 MHz and power level of 25 Watts.

As mentioned, the value of the hydraulic conductivity and flow discharge changed due to RF stimulation. The model assumes that the scalar value of the RF power governs the alteration in the hydraulic conductivity, hence, the variation will be same for all components of the hydraulic conductivity tensor (i.e., the same slope ( $\beta$ ) in all directions). Figure 42 shows the contour/color map for  $k'_{zz}$  (Z component of the RF-stimulated hydraulic conductivity) computed using the inverse model on Slice 7 at a frequency of 726 MHz and RF-power level of 25 Watts. Other components of the  $k'$  tensor can also be plotted. However, since other components than the Z component of hydraulic conductivity was never experimentally measured and the  $k$  of the soil was assumed isotropic and  $\beta$  was assumed the same in all directions,  $k'$  will be isotropic. Figure 43 shows the contour/color map of the RF-power density at a frequency of 726 MHz and RF-power level of 25 Watts on Slice 7. The RF-power density at each node was obtained from the RF forward model generated using COMSOL Multiphysics.

As seen in Figure 42, the hydraulic conductivity along the Z direction changed due to the application of RF waves. As expected and mentioned, due to the linear relationship between the power densities at each node and RF-stimulated hydraulic conductivity, the contour plot of the hydraulic conductivity corresponds to the variation in the power densities.

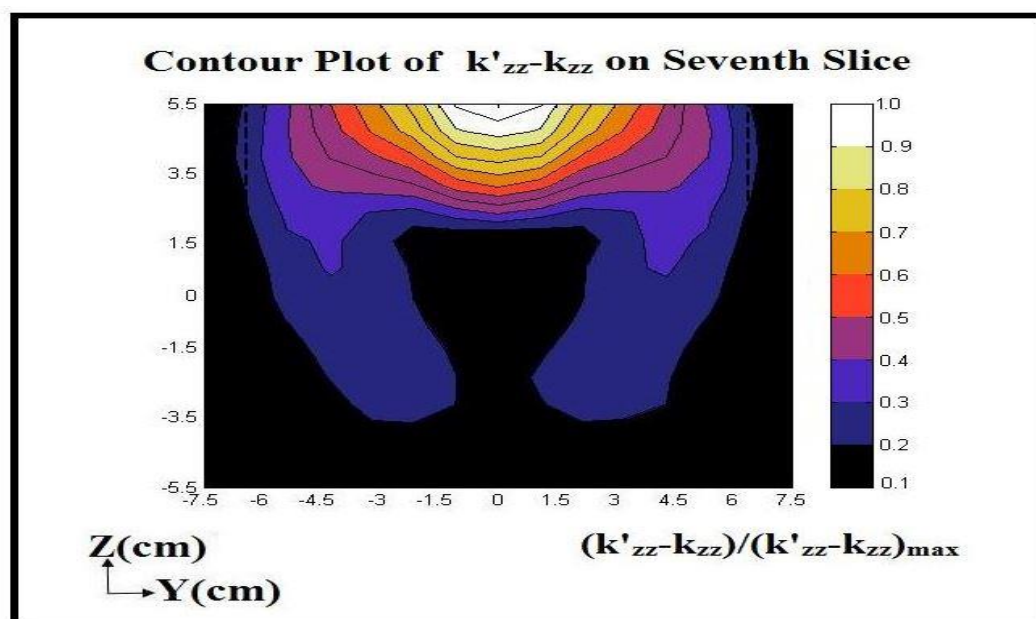


**Figure 42.** Contour/color map of normalized difference between RF-stimulated hydraulic conductivity computed and unstimulated hydraulic conductivity within the natural-sand specimen along the vertical direction (Z direction) on Slice 7 at a frequency of 726 MHz and power level of 25 Watts

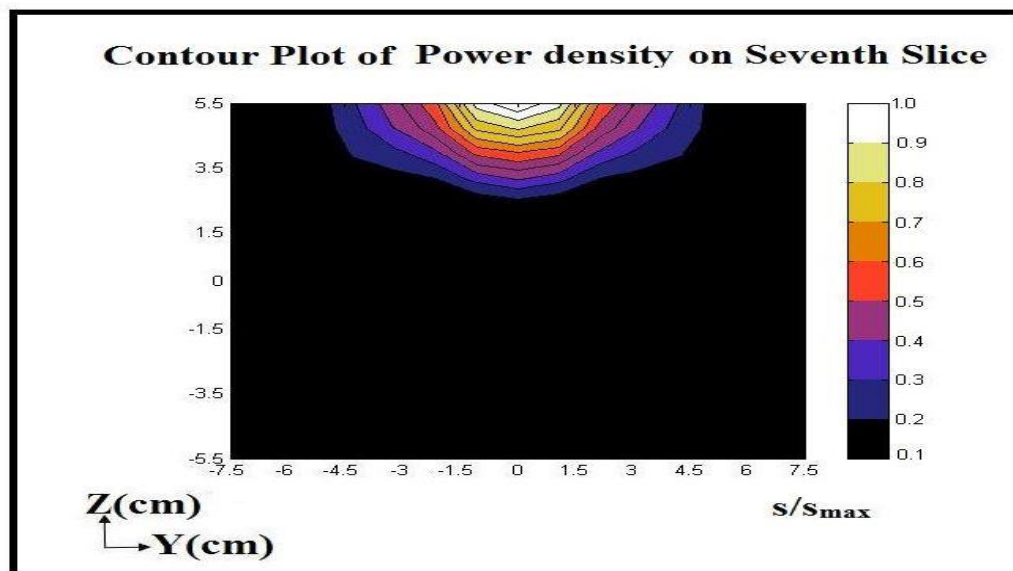


Figure 43. Contour/color map of normalized power density within the natural-sand specimen along the vertical direction (Z direction) on Slice 7 at a frequency of 726 MHz and power level of 25 Watts.



## CHAPTER FIVE: CONCLUSIONS

The conclusions are divided into two sections for two series of tests, Series I and Series II.

### Impact Tests, Series I

- The impact caused a prompt increase in the EPWP.
- The mean EPWP during RF-stimulated impact tests at all power levels are almost equal. The mean-value changes were within the margin of error.
- The value of effective-stress ratio ( $r_u$ ) was within a narrow range of variation at a constant depth below the ground surface. The value of effective-stress ratio indicated the soil did not liquefy completely because its value was less than 1. However, partial liquefaction might have occurred at that depth. Hence, the impact was not strong enough to liquefy soil completely and stronger impact is needed for a full liquefaction.
- When RF-stimulated impact tests were also performed at various frequencies at a constant RF-power level, the generated EPWP was nearly consistent except for one frequency (620 MHz). However, the result of the generation of EPWP cannot be linearly correlated with the frequency because the electric-field pattern at different frequencies are not similar within a cavity of constant size.
- The measurement of electric field inside the cavity was performed at various frequencies. The numerically simulated electric field using COMSOL Multiphysics



was then validated against the measured electric field. The measured and numerically simulated electric fields agree reasonably.

### **Hydraulic-Conductivity Tests, Series II**

- The unstimulated hydraulic conductivity of the glass-bead sample was greater than that of the natural-sand sample.
- At all RF-power levels, in the case of both glass beads and natural sand, RF waves cause an increase in hydraulic conductivity.
- The increase in hydraulic conductivity was not sharp. The hydraulic conductivity increased gradually with time. The gradual increase in the hydraulic-conductivity measurements could be due to the accumulative effects on soil and on water because of the absorption of the RF energy during RF stimulation. The hydraulic conductivity eventually attained a peak value.
- In both glass-bead and natural-sand samples, RF-stimulated hydraulic conductivity increased with increasing RF-power level. However, the percentage increase was observed more in the case of the natural sand than the glass bead. The difference in the effects of RF waves on glass bead and on natural sand could be due to the influence of the silt content within the natural sand.
- When RF stimulation was terminated after the hydraulic conductivity stabilized at its peak value, the hydraulic conductivity slightly decreased with time and stabilized at a smaller value, yet larger than the initial unstimulated value. These tests were terminated in the interest of time and were not continued further to allow the hydraulic conductivity to reach the initial unstimulated value.
- The measured electric field and numerically simulated electric field reasonably agree.

- Results from numerical model of seepage flow showed a uniform decrease in the hydraulic head from the bottom to the top because of the upward seepage flow thorough the sample. In the case of RF-stimulated tests, hydraulic heads were computed using an inverse model based on an optimization scheme.
- A model was assumed to be governing the RF effect on hydraulic conductivity. As mentioned, an optimization scheme was used to find the slope ( $\beta$ ) of this relation. The optimization scheme finds this optimum slope by minimizing a cost/objective function. The optimization scheme acceptably minimized the cost function.
- After optimization, optimized RF-stimulated numerically-calculated hydraulic conductivity and corresponding flow velocity along the Z direction showed a similar spatially variable pattern to that of the power density. The contour/color maps plotted for the hydraulic conductivity, flow velocity, and power density validated the statement.

One of the limitation of this research was not using deaerated water during the entire run of RF-stimulated tests. The deaerated water was used only once to compare the discrepancy between the measured hydraulic-conductivity values using the deaerated and non-deaerated water. The tests were run for several hours, and resources were not available to prepare enough deaerated water for elongated tests that ran multiple hours.

Liquefaction mitigation should be applied throughout the period that the destructive surface waves of earthquake are experienced at the site. Hence, the increase in the hydraulic conductivity should occur throughout the earthquake. If information becomes available about an upcoming earthquake (detecting faster, less destructive pressure or shear waves), then hydraulic conductivity can be increased rapidly before

destructive surface waves arrive to minimize the EPWP generation. The response of the hydraulic conductivity to the RF stimulation at the experimented power and frequency was not fast enough to be considered for liquefaction mitigation during the earthquake where EPWP buildup is very rapid.

### **Future research**

Understanding the correlation between RF waves and change in hydraulic conductivity requires further analysis. With the existing setup, maximum RF power that could be launched was 50 Watts. Future research requires the use of a higher RF-power level to observe more distinct effects. In addition, further study is also required to evaluate the effect of RF waves at different combination of influencing variables such as the RF-power levels, soil properties, RF frequencies, size of resonant cavity, etc. For the liquefaction mitigation study, any future test setup should apply a more consistent and stronger vibration using shaking table.

Apart from liquefaction mitigation, the altering effect of RF waves on hydraulic conductivity can be applied to examine the effect on EM-induced contamination remediation. Water molecules vibrate in alternating EM field and can, therefore, enhance various transport mechanisms. By altering the hydraulic conductivity, the contamination remediation process may speed up.

The change in any transport mechanism due to the change in hydraulic conductivity could be equally helpful in the bio-geochemical processes such as microbially-induced calcite precipitation by easing and creating a uniform distribution of nutrients and oxygen.

## REFERENCES

- ASTM D5084-10, 2006, “Standard Test Methods for Measurement of Hydraulic Conductivity of Saturated Porous Materials using a Flexible Wall Permeameter,” *Book of Standard*, Vol. 04.08, DOI: 10.1520/D5084-10.
- ASTM D2434-68, 2006, “Standard Test Method for Permeability of Granular Soils (Constant Head),” Vol. 04.08, DOI: 10.1520/D2434-68R06.
- Azad, Sahba; Najafi, Atena; Farid, Arvin; Browning, Jim; Barney Smith, Elisa. 2014. “Study of Mechanisms Governing Electromagnetic Alteration of Hydraulic Conductivity of Soils.” In *Geotechnical Special Publication*, 1693–1702. American Society of Civil Engineers (ASCE). doi:10.1061/9780784413272.166.
- Azad, Mahsa. 2012. “ANALYSIS OF ELECTROMAGNETIC STIMULATION OF TRANSPORT IN WATER FOR GEOENVIRONMENTAL APPLICATIONS.” Boise State University.
- Azad, Sahba. 2013. “ELECTROMAGNETIC ALTERATION OF HYDRAULIC CONDUCTIVITY OF SOILS.” Boise State University.
- Bramwell, Steven T. 1999. “Condensed-Matter Science:ferroelectric Ice.” *Nature* 397 (6716): 212. doi:10.1038/16594.
- Cole, Gregory L., Rajesh P. Dhakal, and Fred M. Turner. 2012. “Building Pounding Damage Observed in the 2011 Christchurch Earthquake.” *Earthquake Engineering & Structural Dynamics* 41 (5): 893–913. doi:10.1002/eqe.1164.
- Das, Braja M. 1982. “Soil Mechanics Laboratory Manual.” Oxford University Press New York, 2016.
- Demarest, Kenneth R. 2006. “Waveguides and Resonators.” In *Fundamentals of Engineering Electromagnetics*, edited by Rajeev Bansal, 432–56.

- Fetter, C.W. 2001. "Applied Hydrogeology." 4th ed. Pearson.
- Ganainy, Hesham El, Tarek Abdoun, and Ricardo Dobry. 2012. "Centrifuge Study of the Effect of Permeability and Other Soil Properties on the Liquefaction and Lateral Spreading of Dense Sand." In GeoCongress.
- Hazirbaba, Kenan, and Ellen M Rathje. 2009. "Pore Pressure Generation of Silty Sands due to Induced Cyclic Shear Strains." Journal of Geotechnical and Geoenvironmental Engineering. doi:10.1061/ASCEGT.1943-5606.0000147.
- Hornberger, George M. 1998. Elements of Physical Hydrology. Edited by George M. Hornberger. 2nd ed. JHU Press.
- HUBBERT, M. KING. 1957. "Darcy's Law and the Field Equations of the Flow of Underground Fluids." International Association of Scientific Hydrology. Bulletin. doi:10.1080/02626665709493062.
- Ikezoe, Y.; Hirota, N.; Nakagawa, J.; Kitazawa, K. 1998. "Making Water Levitate." Nature 393 (6687): 749. doi:10.1038/31619.
- Kramer, Steven L. 1996. "Geotechnical Earthquake Engineering." Pearson, 2013.
- Martin, James R., C. Guney Olgun, James K. Mitchell, and H. Turan Durgunoglu. 2004. "High-Modulus Columns for Liquefaction Mitigation." Journal of Geotechnical and Geoenvironmental Engineering. doi:10.1061/(ASCE)1090-0241(2004)130:6(561).
- Najafi, Atena. 2014. "THE EFFECT OF ELECTROMAGNETIC WAVES ON AIRFLOW DURING AIR SPARGING." Boise State University.
- Sharp, Michael K, M Asce, Ricardo Dobry, Tarek Abdoun, and A M Asce. 2003. "Liquefaction Centrifuge Modeling of Sands of Different Permeability." Journal of Geotechnical and Geoenvironmental Engineering. doi:10.1061/ASCE1090-02412003129:121083.
- Sun, Wei1; Xu, Xiaobin2; Xu, Chuanxiang1. 2007. "Effects of H2O Dipole Polarization on Ice Formation Process under Electrostatic Field" 41 (2): 232–35.

Vaid, Y. P. and Negusse, D., 1988, "Preparation of Reconstituted Sand Specimens,"  
*Advanced triaxial testing of soil and rock, ASTM STP 977*, Philadelphia, pp. 405-417.

## APPENDIX A

**Simulation of Experimental Setup in COMSOL Multiphysics**

## Simulation of Experimental Setup in COMSOL Multiphysics

### Hydraulic-Conductivity Test

Modeling Instruction: (Azad, 2013)

#### **MODEL WIZARD**

**1** Go to the **Model Wizard** window.

**2** Click **Next**.

**3** In the **Add physics** tree, select **Radio Frequency>Electromagnetic Waves, Frequency Domain (emw)**.

**4** Click **Next**.

**5** Find the **Studies** subsection. In the tree, select **Preset Studies>Frequency Domain**.

**6** Click **Finish**.

#### **GLOBAL DEFINITIONS**

To help in creating the geometry, define some parameters defining its dimensions.

##### *Parameters*

**1** In the **Model Builder** window, right-click **Global Definitions** and choose **Parameters**.

**2** In the **Parameters** settings window, locate the **Parameters** section.

**3** In the table, enter the following settings:

Name	Expression	Name	Expression
d_1	7[mm]	h_1	3[cm]
d_2	2[mm]	h-2	11[cm]
D	15.2[cm]	a	46[cm]
		f	710[MHz]

Note that as long as you specify the unit in a bracket in the table, you can use different dimensions for length. A schematic of the geometry is shown in Figure A1 to provide a better understanding of the introduced parameters.



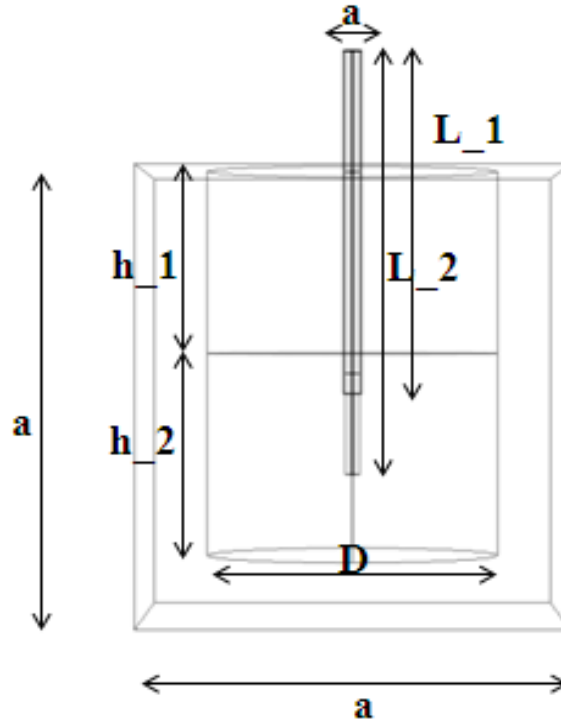


Figure A.1. Schematic of the experimental setup

### GEOMETRY 1

#### *Cylinder 1*

**1** In the **Model Builder** window, under **Model 1** right-click **Geometry 1** and choose **Cylinder**.

**2** In the **Cylinder** settings window, locate the **Size and Shape** section.

**3** In the **Radius** edit field, type  $D/2$ .

**4** In the **Height** edit field, type  $h-1$ .

**5** In the **Position** edit field, type  $x:0, y:0, z:a-h$ .

#### *Cylinder 2*

**1** In the **Model Builder** window, under **Model 1** right-click **Geometry 1** and choose **Cylinder**.

**2** In the **Cylinder** settings window, locate the **Size and Shape** section.

**3** In the **Radius** edit field, type  $D/2$ .

4 In the **Height** edit field, type h-2.

5 In the **Position** edit field, type x:0, y: 0, z:a-h-1-h-2.

*Work Plan 1*

1 In the **Model Builder** window, under **Model 1** right-click **Geometry 1** and choose **Work Plane**.

2 In the **Geometry**, under work plane right-click and choose **Circle**.

3 In the **Circle** settings window, **locate** the **Size and Shape** section.

4 In the **Radius** edit field, type d\_2/2.

5 In the **Geometry**, under work plane right-click and choose **Circle**.

6 In the **Circle** settings window, **locate** the **Size and Shape** section.

7 In the **Radius** edit field, type d\_1/2.

8 In the **Position** edit field choose **Base**: Center, and type x: 0, y: d.

9 In the **Geometry**, under work plane right-click and choose **Boolean**

**Operation>Differences.**

10 In the **Difference** settings window, **locate** the **Objects to add** and **Objects to subtract** section.

11 In the **Objects to add** setting, choose **C1**.

12 In the **Objects to subtract** setting, choose **C2**.

13 In the **Model Builder** window, under **Work Plane 1** right-click and choose **Extrude**.

14 In the **Extrude** settings window, specify the **Distances** and type: L\_1.

*Work Plan 2*

1 In the **Model Builder** window, under **Model 1** right-click **Geometry 1** and choose **Work Plane**.

2 In the **Geometry**, under work plane right-click and choose **Circle**.

3 In the **Circle** settings window, **locate** the **Size and Shape** section.

4 In the **Radius** edit field, type d-2/2.

5 In the **Model Builder** window, under **Work Plane 1** right-click and choose

**Extrude.**

6 In the **Extrude** settings window, **specify** the **Distances** and type: L\_2.

: L\_3.

*Block 1*

**1** In the **Model Builder** window, under **Model 1** right-click **Geometry 1** and choose **Block**.

**2** In the **Block** settings window, locate the **Size and Shape** section.

**3** In the **Width** edit field, type a.

**4** In the **Depth** edit field, type a.

**5** In the **Height** edit field, type a.

**6** In the **Position** edit field choose **Base: Center** and type x0, y: 0, z: a/2.

**MATERIALS**

**1** In the **Model Builder** window, under **Model 1** right-click **Materials** and choose **Open Material Browser**.

**2** In the **Material Browser** window, locate the **Materials** section.

**3** In the tree, select **Built-In>Copper**.

**4** Right-click and choose **Add Material to Model** from the menu.

**5** In the tree, select **Built-In>Acrylic Plastic**.

**6** Right-click and choose **Add Material to Model** from the menu.

**7** In the tree, select **Built-In>Water**.

**8** Right-click and choose **Add Material to Model** from the menu.

**9** In the tree, select **Built-In>Air**.

**10** Right-click and choose **Add Material to Model** from the menu.

**11** Right-click **Material** and choose **Material**.

**12** Go to the **Rename Material** dialog box and type Dielectric in the **New name** edit field.

**13** Click **OK**.

*Copper*

**1** In the **Model Builder** window, under **Model 1>Materials** click **Copper**.

**2** Select Domain 4, 5, 6, 7, and, 9.

*Acrylic Plastic*

**1** In the **Model Builder** window, under **Model 1>Materials** click **Acrylic plastic**.

**2** Select Domain 10, 11, 12, 14, 58.

*Water*

**1** In the **Model Builder** window, under **Model 1>Materials** click **Water**.

**2** Select Domain 3 only.

*Air*

**1** In the **Model Builder** window, under **Model 1>Materials** click **Air**.

**2** Select Domain 1.

*Dielectric*

**1** In the **Model Builder** window, under **Model 1>Materials** click **Dielectric**.

**2** Select Domain 8, and, 9.

**3** In the **Material** settings window, locate the **Material Contents** section.

**4** In the table, enter the following settings:

*Table A.2 Dielectric Properties*

Property	name	Value	Unit	Property group
Electric Conductivity	sigma	0	S/m	Basic
Relative Permittivity	epsilon <sub>r</sub>	2.03	1	Basic
Relative Permeability	mu <sub>r</sub>	1	1	Basic

## ELECTROMAGNETIC WAVES, FREQUENCY DOMAIN

*Electromagnetic Waves (emw)*

**1** In the **Model Builder** window, click **Electromagnetic Waves (emw)**.

**2** In the **Electromagnetic Waves** settings window, select the Domains.

**3** From the **Selection** list, choose **Manual**.

**2** Select Domain 1, 2, 3, 8, and, 10.

*Perfect Electric Conductor*

**1** In the **Model Builder** window, right-click **Electromagnetic Waves (emw)** and choose **Perfect Electric Conductor**.

**2** In the **Perfect Electric Conductor** settings window, locate the **Boundary Selection** section.

3 Select Boundaries 15, 16, 17, 18, 19, 20, 21, 24, 25, 31, 32, 34, 35, 38, 39, 41, 42, 43, 44, 45, 46, 50, 51, 53, 54, and, 57.

*Port 1*

1 In the **Model Builder** window, right-click **Electromagnetic Waves** and choose the boundary condition **Port**.

2 In the **Port** settings window, locate the **Boundary Selection** section.

3 Select boundary 37.

4 Locate the **Port Properties** section. From the **Type of port** list, choose **Coaxial**.

5 From the **Wave excitation at this port** list, choose **On**.

**MESH**

In order to control the study time and to get a good accuracy, the mesh should be especially defined by the user.

1 In the **Model Builder** window, under **Model 1** right-click **Mesh 1** and choose **Free Tetrahedral**.

*Size*

1 In the **Model Builder** window, under **Model 1>Mesh 1** click **Size**.

2 In the **Size** settings window, locate the **Element Size** section.

3 From the **Predefined** list, choose **Normal**.

*Size 1*

1 In the **Model Builder** window, under **Model 1>Mesh 1** right-click **Free Tetrahedral 1** and choose **Size**.

2 In the **Size** settings window, locate the **Geometric Entity Selection** section.

3 From the **Geometric entity level** list, choose **Domain**.

4 From the **Selection** list, choose 3.

5 Locate the **Element Size** section. From the **Predefined** list, choose **Fine**.

*Size 2*

1 In the **Model Builder** window, under **Model 1>Mesh 1** right-click **Free Tetrahedral 2** and choose **Size**.

2 In the **Size** settings window, locate the **Geometric Entity Selection** section.

3 From the **Geometric entity level** list, choose **Domain**.

**4** From the **Selection** list, choose 2, 8, and, 10.

**5** Locate the **Element Size** section. From the **Predefined** list, choose **Normal**.

### **STUDY 1**

#### *Step 1: Frequency Domain*

**1** In the **Model Builder** window, under **Study 1** click **Step 1: Frequency Domain**.

**2** In the **Frequency Domain** settings window, locate the **Study Settings** section.

**3** In the **Frequencies** edit field, type f.

**4** In the **Model Builder** window, click **Study 1**.

**5** Click the **Compute** button.

### **RESULTS**

#### *3D Plot Group 1*

**1** In the **Model Builder** window, right-click **Results** and choose **3D Plot Group**.

**2** Right-click **3D Plot Group 1** and choose **Slice**.

**3** In the **Slice** settings window, click **Replace Expression** in the upper-right corner of the **Expression** section. From the menu, choose any component of an interest. You can also simply type **abs ( $E_z$ )**.

**4** Locate the **Plane Data** section. From the **Plane** list, choose **XZ-planes**.

**5** From the **Entry method** list, choose **Coordinates**.

**6** In the **z-coordinates** edit field, type .08.

Although the component of an interest is **abs ( $E_z$ )** for this model to be compared with the experimental results, various plots of other components of the electromagnetic field can be also obtained.

## APPENDIX B

**M. File Written in MATLAB Interface to Numerically Calculate Hydraulic Head**

## M. File Written in MATLAB Interface to Numerically Calculate Hydraulic Head

(Unstimulated)

### Natural Sand

```

clc
clear all
H1=0.1; %head at the bottom of the soil

H2=0.814; %head on top of the soil
D=0.15; %diameter of the cross section of the soil
le=0.11; %total length of the soil
kxy=0; kyx=0; kzx=0; kxz=0; kyz=0; kzy=0; kyy=7.9e-5; kxx=0; kzz=0;
%hydraulic conductivity
n=15; %number of nodes in x-dir (horizontal)
m=15; %number of nodes in z-dir(depth)
L=m*n; %total number of nodes in a plane
p=15; %number of planes in y-dir (vertical)
s=m*n*p; %total number of nodes in 3-D
dx=D/(n-1);
dz=D/(m-1);
dy=le/(p-1);
a=zeros(s,s); %variable matrix
b=zeros(s,1);
%% Geometry of the domain and assigning nodes
%Define x and y coordinates for nodes in a plane
mm=1;
kk=-7;%this is a multiplication factor in x co-ordinate
for ii=1:m; %loop performing along z direction
    jj=-7; %this is a multiplication factor in z co-ordinate
    for rr=mm:n*ii; %loop performing along z direction
        cord(rr,:)=[jj*n/(n-1) kk*m/(m-1)];
        mm=mm+1;
        jj=jj+1;
    end
    kk=kk+1;
end
%Defining x and y coordinates for nodes in respective planes from plane
2
%to plane 15
for ii=1:p-1; %loop performing in y-direction
    cord(ii*L+1:ii*L+L,:)=cord(1:L,:);
end
xc=0;yc=0; %the centre of the plane is (0,0)
%% Defining normal vector
%Finding x and y component of unit normal vector for nodes

for ii=1:s;
    lve(ii)=sqrt((cord(ii,1)-xc)^2+(cord(ii,2)-yc)^2); %length of the
vector originating from (0,0) and ending at (x,y)

```



```

    xl=(cord(ii,1)-xc);yl=(cord(ii,2)-yc);
    uxy(ii,:)= [xl/lve(ii) yl/lve(ii)]; %or cos alpha and sin alpha
respectively
end
%% Defining permeability

%Putting permeability in a tensor form
for ii=1:s
    kp(:,:,ii)=[7.9244e-5 0 0
    0 7.9244e-5 0
    0 0 7.9244e-5];
end
for jj=0:p-1
    for kk=[6:10 216:220 19:27 199:207 33:34 183:184 42:43 192:193 47:48
167:168 58:59 178:179 76:15:136 90:15:150 62:15:152 74:15:164]
        kp(1,1,jj*L+kk)=0;
        kp(3,3,jj*L+kk)=0;
    end
end

%% Boundary condition

a=zeros(s,s);
b=zeros(s,1);
%Applying boundary condition to the necessary nodes
for k=1:s
    if k>=1&&k<=L
        a(k,k)=1;
        b(k,1)=H2;
    elseif k>=(p-1)*L+1 &&k<=s
        a(k,k)=1;
        b(k,1)=H1;
    elseif k>=L+n+1 &&k<=(p-1)*L-n
        a(k,k+1)=kp(1,1,k)/((dx))^2;
        a(k,k-1)=kp(1,1,k)/((dx))^2;
        a(k,k+n)=kp(3,3,k)/((dz))^2;
        a(k,k-n)=kp(3,3,k)/((dz))^2;
        a(k,k+L)=kp(2,2,k)/((dy))^2;
        a(k,k-L)=kp(2,2,k)/((dy))^2;
        a(k,k)=-
2*(kp(1,1,k)/((dx))^2+kp(3,3,k)/((dz))^2+kp(2,2,k)/((dy))^2+kp(1,2,k)/
(dx*dy)+kp(2,1,k)/(dx*dy)+kp(2,3,k)/(dy*dz)+kp(3,2,k)/(dy*dz)+kp(1,3,k)/
(dx*dz)+kp(3,1,k)/(dx*dz));
        a(k,k+L+1)=(kxy+kyx)/(dx*dy);
        a(k,k-L-1)=(kxy+kyx)/(dx*dy);
        a(k,k+L+n)=(kyz+kzy)/(dz*dy);
        a(k,k-L-n)=(kyz+kzy)/(dz*dy);
        a(k,k+n+1)=(kxz+kzx)/(dx*dz);
        a(k,k-n-1)=(kxz+kzx)/(dx*dz);
    end
end
%boundary conditon for impermeable boundary

for k=0:p-1;

```

```

    for enew=[1:15 16:15:196 211:225 30:15:210 16:15:6 17 18 28 29 32 44
182 194 197 198 208 209]
        % abcd=enew
        a(k*L+enew,:)=0;
        a(k*L+enew,k*L+enew)=1;
        b(k*L+enew,1)=0;
    end
end
for k=0:p-1;
    for anew=[7:9]
        % for anew=[1:15]
        a(L*k+anew,:)=0;
        a(L*k+anew,L*k+anew)=1;
        a(L*k+anew,L*k+anew+n)=-1;
    end
    for bnew=[217:219]
        % for bnew=[211:225]
        a(k*L+bnew,:)=0;
        a(k*L+bnew,k*L+bnew)=1;
        a(k*L+bnew,k*L+bnew-n)=-1;
    end
    for cnew=[91:15:121]
        % for cnew=[16:15:196]
        a(k*L+cnew,:)=0;
        a(k*L+cnew,k*L+cnew)=1;
        a(k*L+cnew,k*L+cnew+1)=-1;
    end
    for dnew=[105:15:130]
        % for dnew=[30:15:210]
        a(k*L+dnew,:)=0;
        a(k*L+dnew,k*L+dnew)=1;
        a(k*L+dnew,k*L+dnew-1)=-1;
    end

    for fnew=[6 19 20 33 47 62 76]
        a(k*L+fnew,:)=0;
        a(k*L+fnew,k*L+fnew)=(uxy(k*L+fnew,1)/(dx)+uxy(k*L+fnew,2)/(dz));
        a(k*L+fnew,k*L+fnew+1)=-uxy(k*L+fnew,1)/(dx);
        a(k*L+fnew,k*L+fnew+n)=-uxy(k*L+fnew,2)/(dz);
    end
    for fnew=[10 26 27 43 59 74 90]
        a(k*L+fnew,:)=0;
        a(k*L+fnew,k*L+fnew)=(uxy(k*L+fnew,1)/(dx)-uxy(k*L+fnew,2)/(dz));
        a(k*L+fnew,k*L+fnew-1)=-uxy(k*L+fnew,1)/(dx);
        a(k*L+fnew,k*L+fnew+n)=+uxy(k*L+fnew,2)/(dz);
    end
    for fnew=[136 153 167 183 199 200 216]
        a(k*L+fnew,:)=0;
        a(k*L+fnew,k*L+fnew)=(uxy(k*L+fnew,1)/(dx)-uxy(k*L+fnew,2)/(dz));
        a(k*L+fnew,k*L+fnew+1)=-uxy(k*L+fnew,1)/(dx);
        a(k*L+fnew,k*L+fnew-n)=+uxy(k*L+fnew,2)/(dz);
    end
    for fnew=[150 164 179 193 206 207 210]
        a(k*L+fnew,:)=0;
        a(k*L+fnew,k*L+fnew)=(uxy(k*L+fnew,1)/(dx)+uxy(k*L+fnew,2)/(dz));
        a(k*L+fnew,k*L+fnew-1)=-uxy(k*L+fnew,1)/(dx);
        a(k*L+fnew,k*L+fnew-n)=-uxy(k*L+fnew,2)/(dz);
    end

```

```

end

end

%% Head calculation

h=a^-1*b;
%putting head in 3d coordinate form.
H=zeros(n,p,m); %head in soil in 3-D matrix
for mmm=1:m
    jjj=1;
    for jj=1:p
        iii=1;
        for ii=(jj-1)*L+1+(mmm-1)*m:(jj-1)*L+n+(mmm-1)*m
            xy(iii,jjj,mmm)=h(ii);
            iii=iii+1;
        end
        jjj=jjj+1;
    end
end
%% Discharge calculation

ane=D^2/((n-1)*(m-1));
cne=D^2/(2*(n-1)*(m-1));
vex=zeros(s,1);
vey=zeros(s,1);
%velocity along x direction
for ii=0:p-1
    for kk=1:n
        vex(ii*L+(kk-1)*15+1,1)=(-kp(1,1,ii*L+(kk-1)*15+1)*((h(ii*L+(kk-1)*15+1)-h(ii*L+(kk-1)*15+1))/dx));
        vex(ii*L+(kk-1)*15+15,1)=(-kp(1,1,ii*L+(kk-1)*15+15)*((h(ii*L+(kk-1)*15+15)-h(ii*L+(kk-1)*15+15-1))/dx));
        mul=2+(kk-1)*15;
        for jj=[mul:mul+12]
            vex(ii*L+jj,1)=(-kp(1,1,ii*L+jj)*((h(ii*L+jj+1)-h(ii*L+jj-1))/(2*dx)));
        end
    end
end

%velocity along y direction
for ii=L+1:s-L
    vey(ii,1)=(-kp(2,2,ii)*((h(ii+L)-h(ii-L))/(2*dy)));
end
for ii=1:L
    vey(ii,1)=(-kp(2,2,ii)*((h(ii+L)-h(ii))/dy));
end
for ii=s-L+1
    vey(ii,1)=(-kp(2,2,ii)*((h(ii)-h(ii-L))/dy));
end
Qy=zeros(L,1);
Qsum=0;
for kk=(p-2)*L+1:(p-1)*L
    Qy(kk,1)=vey(kk,1)*ane;
end

```

```

mult=p-2;
for anew=[1:15 30:15:210 16:15:196 211:225]
    Qy(mult*L+anew,1)=vey(mult*L+anew,1)*cne;
end
for bnew=[1:6 10:15 16:19 27:30 31:32 44:45 46:47 59:60 61 75 151 165
166:167 179:180 181:182 194:195 196:199 207:210 211:216 220:225]
    Qy(mult*L+bnew,1)=0;
end

for kk=(p-2)*L+1:(p-1)*L
    Qsum=Qsum+Qy(kk,1);
end
Qsum

abx=linspace(-7.5,7.5,15);
aby=linspace(-5.5,5.5,15);
figure(1)
contourf(abx,aby,xy(:, :, 1)');colorbar;hold on;
newposx=ones(1,15)*2.14286;newnegx=ones(1,15)*-2.14286;
h1=plot(newposx,aby,'--k');hold on;h2=plot(newnegx,aby,'--k');hold off;
set([h1 h2], 'LineWidth',2)
title('Head on First and Fifteenth layer')
ax = gca;
set(ax, 'XTick', [-7.5,-6,-4.5,-3,-1.5,0,1.5,3,4.5,6,7.5])
set(ax, 'YTick', [-5.5,-3.5,-1.5,0,1.5,3.5,5.5])

figure(2)
contourf(abx,aby,xy(:, :, 2)');colorbar;hold on;
newposx=ones(1,15)*4.28571;newnegx=ones(1,15)*-4.28571;
h1=plot(newposx,aby,'--k');hold on;h2=plot(newnegx,aby,'--k');hold off;
set([h1 h2], 'LineWidth',2)
title('Head on Second and Fourteenth layer')
ax = gca;
set(ax, 'XTick', [-7.5,-6,-4.5,-3,-1.5,0,1.5,3,4.5,6,7.5])
set(ax, 'YTick', [-5.5,-3.5,-1.5,0,1.5,3.5,5.5])

figure(3)
contourf(abx,aby,xy(:, :, 3)');colorbar;hold on;
newposx=ones(1,15)*5.35714;newnegx=ones(1,15)*-5.35714;
h1=plot(newposx,aby,'--k');hold on;h2=plot(newnegx,aby,'--k');hold off;
set([h1 h2], 'LineWidth',2)
title('Head on Third and Thirteenth layer')
ax = gca;
set(ax, 'XTick', [-7.5,-6,-4.5,-3,-1.5,0,1.5,3,4.5,6,7.5])
set(ax, 'YTick', [-5.5,-3.5,-1.5,0,1.5,3.5,5.5])

```

figure(4)

```

contourf(abx,aby,xy(:, :, 4)');colorbar;hold on;
newposx=ones(1,15)*6.42857;newnegx=ones(1,15)*-6.42857;
h1=plot(newposx,aby,'--k');hold on;h2=plot(newnegx,aby,'--k');hold off;
set([h1 h2], 'LineWidth',2)
title('Head on Fourth and Twelfth layer')
ax = gca;
set(ax, 'XTick', [-7.5,-6,-4.5,-3,-1.5,0,1.5,3,4.5,6,7.5])
set(ax, 'YTick', [-5.5,-3.5,-1.5,0,1.5,3.5,5.5])

```

```

figure(5)
contourf(abx,aby,xy(:, :, 5)');colorbar;hold on;
newposx=ones(1,15)*6.42857;newnegx=ones(1,15)*-6.42857;
h1=plot(newposx,aby,'--k');hold on;h2=plot(newnegx,aby,'--k');hold off;
set([h1 h2], 'LineWidth',2)
title('Head on Fifth and Eleventh layer')
ax = gca;
set(ax, 'XTick', [-7.5,-6,-4.5,-3,-1.5,0,1.5,3,4.5,6,7.5])
set(ax, 'YTick', [-5.5,-3.5,-1.5,0,1.5,3.5,5.5])

```

```

figure(6)
contourf(abx,aby,xy(:, :, 6)');colorbar;
title('Head on Sixth and Tenth layer')
ax = gca;
set(ax, 'XTick', [-7.5,-6,-4.5,-3,-1.5,0,1.5,3,4.5,6,7.5])
set(ax, 'YTick', [-5.5,-3.5,-1.5,0,1.5,3.5,5.5])

```

```

figure(7)
contourf(abx,aby,xy(:, :, 7)');colorbar;
title('Head on Seventh and Ninth layer')
ax = gca;
set(ax, 'XTick', [-7.5,-6,-4.5,-3,-1.5,0,1.5,3,4.5,6,7.5])
set(ax, 'YTick', [-5.5,-3.5,-1.5,0,1.5,3.5,5.5])

```

```

figure(8)
contourf(abx,aby,xy(:, :, 8)');colorbar;
title('Head on Eighth layer')
ax = gca;
set(ax, 'XTick', [-7.5,-6,-4.5,-3,-1.5,0,1.5,3,4.5,6,7.5])
set(ax, 'YTick', [-5.5,-3.5,-1.5,0,1.5,3.5,5.5])

```

```
%% vector plot
```

```

vx=zeros(n,p,m); %velocity x component in 3d
for mmm=1:m
    jjj=1;
    for jj=1:p
        iii=1;
        for ii=(jj-1)*L+1+(mmm-1)*m:(jj-1)*L+n+(mmm-1)*m

```

```

        vx(iii,jjj,mmm)=vex(ii);
        iii=iii+1;
    end
    jjj=jjj+1;
end
end

vy=zeros(n,p,m); %velocity y component in 3d
for mmm=1:m
    jjj=1;
    for jj=1:p
        iii=1;
        for ii=(jj-1)*L+1+(mmm-1)*m:(jj-1)*L+n+(mmm-1)*m
            vy(iii,jjj,mmm)=vey(ii);
            iii=iii+1;
        end
        jjj=jjj+1;
    end
end
figure(9)
quiver(abx,aby,vx(:,:,8),vy(:,:,8))
title('Velocity vectors on eighth slice')
xlim([-8 7]);ylim([-5.5 5.5]);
figure(10)
quiver(abx,aby,vx(:,:,7),vy(:,:,7))
xlim([-8 7]);ylim([-5.5 5.5]);
figure(11)
quiver(abx,aby,vx(:,:,6),vy(:,:,6))
xlim([-8 7]);ylim([-5.5 5.5]);
figure(12)
quiver(abx,aby,vx(:,:,5),vy(:,:,5))
figure(13)
quiver(abx,aby,vx(:,:,4),vy(:,:,4))
figure(14)
quiver(abx,aby,vx(:,:,3),vy(:,:,3))
figure(15)
quiver(abx,aby,vx(:,:,2),vy(:,:,2))
figure(16)
quiver(abx,aby,vx(:,:,1),vy(:,:,1))

```

## M. File Written in MATLAB Interface to Numerically Calculate Hydraulic Head (RF-Stimulated)

### Natural sand

```

clc
clear all
H1=0.1; %head at the bottom of the soil

H2=0.814; %head on top of the soil
D=0.15; %diameter of the cross section of the soil
le=0.11; %total length of the soil

n=15; %number of nodes in x-dir (horizontal)
m=15; %number of nodes in z-dir(depth)
L=m*n; %total number of nodes in a plane
p=15; %number of planes in y-dir (vertical)
s=m*n*p; %total number of nodes in 3-D
dx=D/(n-1);
dz=D/(m-1);
dy=le/(p-1);
a=zeros(s,s); %variable matrix
b=zeros(s,1);
%% Power density, hydraulic conductivity and alpha value
powdx=xlsread('testdatax');
powdy=xlsread('testdatay');
powdz=xlsread('testdataz');
kkp=[7.925e-5 0 0
      0 7.925e-5 0
      0 0 7.925e-5];
alph=4.5e-9;
anez=D*le/((n-1)*(p-1));
anex=D*D/((n-1)*(m-1));
aney=D*D/((n-1)*(m-1));

%% Geometry of the domain and assigning nodes
%Define x and y coordinates for nodes in a plane
mm=1;
kk=-7;%this is a multiplication factor in x co-ordinate
for ii=1:m; %loop performing along z direction
    jj=-7; %this is a multiplication factor in z co-ordinate
    for rr=mm:n*ii; %loop performing along z direction
        cord(rr,:)=[jj*n/(n-1) kk*m/(m-1)];
        mm=mm+1;
        jj=jj+1;
    end
    kk=kk+1;
end
%Defining x and y coordinates for nodes in respective planes from plane
2
%to plane 15
for ii=1:p-1; %loop performing in y-direction
    cord(ii*L+1:ii*L+L,:)=cord(1:L,:);

```

```

end
xc=0;yc=0; %the centre of the plane is (0,0)
%% Defining normal vector
%Finding x and y component of unit normal vector for nodes

for ii=1:s;
    lve(ii)=sqrt((cord(ii,1)-xc)^2+(cord(ii,2)-yc)^2); %length of the
vector originating from (0,0) and ending at (x,y)
    xl=(cord(ii,1)-xc);yl=(cord(ii,2)-yc);
    uxy(ii,:)=[xl/lve(ii) yl/lve(ii)]; %or cos alpha and sin alpha
respectively
end
%% Defining permeability

%Putting permeability in a tensor form
Qst=10.78e-6;
ijk=0;
Qsum=0;
er=0.03;
for ii=1:s
    kp(:, :, ii)=kkp;
end

for jj=0:p-1
    for kk=[6:10 216:220 19:27 199:207 33:34 183:184 42:43 192:193 47:48
167:168 58:59 178:179 76:15:136 90:15:150 62:15:152 74:15:164]
        kp(1,1,jj*L+kk)=0;
        kp(3,3,jj*L+kk)=0;
    end
end
while abs((Qst-Qsum)/Qst)>er
%% Boundary condition

a=zeros(s,s);
b=zeros(s,1);
%Applying boundary condition to the necessary nodes
for k=1:s
    if k>=1&&k<=L
        a(k,k)=1;
        b(k,1)=H2;
    elseif k>=(p-1)*L+1 &&k<=s
        a(k,k)=1;
        b(k,1)=H1;
    elseif k>=L+n+1 &&k<=(p-1)*L-n
        a(k,k+1)=kp(1,1,k)/((dx))^2;
        a(k,k-1)=kp(1,1,k)/((dx))^2;
        a(k,k+n)=kp(3,3,k)/((dz))^2;
        a(k,k-n)=kp(3,3,k)/((dz))^2;
        a(k,k+L)=kp(2,2,k)/((dy))^2;
        a(k,k-L)=kp(2,2,k)/((dy))^2;
        a(k,k)=-
2*(kp(1,1,k)/((dx))^2+kp(3,3,k)/((dz))^2+kp(2,2,k)/((dy))^2+kp(1,2,k)/
(dx*dy)+kp(2,1,k)/(dx*dy)+kp(2,3,k)/(dy*dz)+kp(3,2,k)/(dy*dz)+kp(1,3,k)/
(dx*dz)+kp(3,1,k)/(dx*dz));
    end
end

```



```

a(k,k+L+1)=(kp(1,2)+kp(2,1))/(dx*dy);
a(k,k-L-1)=(kp(1,2)+kp(2,1))/(dx*dy);
a(k,k+L+n)=(kp(2,3)+kp(3,2))/(dz*dy);
a(k,k-L-n)=(kp(2,3)+kp(3,2))/(dz*dy);
a(k,k+n+1)=(kp(1,3)+kp(3,1))/(dx*dz);
a(k,k-n-1)=(kp(1,3)+kp(3,1))/(dx*dz);
end
end
%boundary conditon for impermeable boundary

for k=0:p-1;
for enew=[1:15 16:15:196 211:225 30:15:210 16:15:6 17 18 28 29 32 44
182 194 197 198 208 209]
% abcd=enew
a(k*L+enew,:)=0;
a(k*L+enew,k*L+enew)=1;
b(k*L+enew,1)=0;
end
end
for k=0:p-1;
for anew=[7:9]
% for anew=[1:15]
a(L*k+anew,:)=0;
a(L*k+anew,L*k+anew)=1;
a(L*k+anew,L*k+anew+n)=-1;
end
for bnew=[217:219]
% for bnew=[211:225]
a(k*L+bnew,:)=0;
a(k*L+bnew,k*L+bnew)=1;
a(k*L+bnew,k*L+bnew-n)=-1;
end
for cnew=[91:15:121]
% for cnew=[16:15:196]
a(k*L+cnew,:)=0;
a(k*L+cnew,k*L+cnew)=1;
a(k*L+cnew,k*L+cnew+1)=-1;
end
for dnew=[105:15:130]
% for dnew=[30:15:210]
a(k*L+dnew,:)=0;
a(k*L+dnew,k*L+dnew)=1;
a(k*L+dnew,k*L+dnew-1)=-1;
end

for fnew=[6 19 20 33 47 62 76]
a(k*L+fnew,:)=0;
a(k*L+fnew,k*L+fnew)=(uxy(k*L+fnew,1)/(dx)+uxy(k*L+fnew,2)/(dz));
a(k*L+fnew,k*L+fnew+1)=-uxy(k*L+fnew,1)/(dx);
a(k*L+fnew,k*L+fnew+n)=-uxy(k*L+fnew,2)/(dz);
end
for fnew=[10 26 27 43 59 74 90]
a(k*L+fnew,:)=0;
a(k*L+fnew,k*L+fnew)=(uxy(k*L+fnew,1)/(dx)-uxy(k*L+fnew,2)/(dz));
a(k*L+fnew,k*L+fnew-1)=-uxy(k*L+fnew,1)/(dx);
a(k*L+fnew,k*L+fnew+n)=+uxy(k*L+fnew,2)/(dz);

```

```

end
for fnew=[136 153 167 183 199 200 216]
    a(k*L+fnew,:)=0;
    a(k*L+fnew,k*L+fnew)=(uxy(k*L+fnew,1)/(dx)-uxy(k*L+fnew,2)/(dz));
    a(k*L+fnew,k*L+fnew+1)=-uxy(k*L+fnew,1)/(dx);
    a(k*L+fnew,k*L+fnew-n)=+uxy(k*L+fnew,2)/(dz);
end
for fnew=[150 164 179 193 206 207 210]
    a(k*L+fnew,:)=0;
    a(k*L+fnew,k*L+fnew)=(uxy(k*L+fnew,1)/(dx)+uxy(k*L+fnew,2)/(dz));
    a(k*L+fnew,k*L+fnew-1)=-uxy(k*L+fnew,1)/(dx);
    a(k*L+fnew,k*L+fnew-n)=-uxy(k*L+fnew,2)/(dz);
end

end
%% Head calculation

h=a^-1*b;
%putting head in 3d coordinate form.
H=zeros(n,p,m); %head in soil in 3-D matrix
for mmm=1:m
    jjj=1;
    for jj=1:p
        iii=1;
        for ii=(jj-1)*L+1+(mmm-1)*m:(jj-1)*L+n+(mmm-1)*m
            xy(iii,jjj,mmm)=h(ii);
            iii=iii+1;
        end
        jjj=jjj+1;
    end
end
%% Discharge calculation

ane=D^2/((n-1)*(m-1));
cne=D^2/(2*(n-1)*(m-1));
vex=zeros(s,1);
vey=zeros(s,1);
%velocity along x direction
for ii=0:p-1
    for kk=1:n
        vex(ii*L+(kk-1)*15+1,1)=(-kp(1,1,ii*L+(kk-1)*15+1)*((h(ii*L+(kk-1)*15+1)-h(ii*L+(kk-1)*15+15))/dx));
        vex(ii*L+(kk-1)*15+15,1)=(-kp(1,1,ii*L+(kk-1)*15+15)*((h(ii*L+(kk-1)*15+15)-h(ii*L+(kk-1)*15+15-1))/dx));
        mul=2+(kk-1)*15;
        for jj=[mul:mul+12]
            vex(ii*L+jj,1)=(-kp(1,1,ii*L+jj)*((h(ii*L+jj+1)-h(ii*L+jj-1))/(2*dx)));
        end
    end
end
end
%velocity along y direction
for ii=L+1:s-L
    vey(ii,1)=(-kp(2,2,ii)*((h(ii+L)-h(ii-L))/(2*dy)));
end

```

```

for ii=1:L
    vey(ii,1)=(-kp(2,2,ii)*(h(ii+L)-h(ii))/dy));
end
for ii=s-L+1
    vey(ii,1)=(-kp(2,2,ii)*(h(ii)-h(ii-L))/dy));
end
Qy=zeros(L,1);
Qsum=0;
for kk=(p-2)*L+1:(p-1)*L
    Qy(kk,1)=vey(kk,1)*ane;
end
mult=p-2;
for anew=[1:15 30:15:210 16:15:196 211:225]
    Qy(mult*L+anew,1)=vey(mult*L+anew,1)*cne;
end
for bnew=[1:6 10:15 16:19 27:30 31:32 44:45 46:47 59:60 61 75 151 165
166:167 179:180 181:182 194:195 196:199 207:210 211:216 220:225]
    Qy(mult*L+bnew,1)=0;
end

for kk=(p-2)*L+1:(p-1)*L
    Qsum=Qsum+Qy(kk,1);
end
Qsum
ijk=ijk+1
for ii=1:s

kp(:, :, ii)=kkp+sqrt(alph*(powdx(ii)*anex+powdy(ii)*aney+powdz(ii)*anez)
);

kp(1,2,ii)=0;kp(2,1,ii)=0;kp(1,3,ii)=0;kp(3,1,ii)=0;kp(2,3,ii)=0;kp(3,2
,ii)=0;
end
for jj=0:p-1
    for kk=[6:10 216:220 19:27 199:207 33:34 183:184 42:43 192:193 47:48
167:168 58:59 178:179 76:15:136 90:15:150 62:15:152 74:15:164]
        kp(1,1,jj*L+kk)=0;
        kp(3,3,jj*L+kk)=0;
    end
end
alph=alph+4e-9;
end

%% Plotting of head

abx=linspace(-7.5,7.5,15);
aby=linspace(-5.5,5.5,15);
figure(1)
contourf(abx,aby,xy(:, :, 1)');colorbar;hold on;
newposx=ones(1,15)*2.14286;newnegx=ones(1,15)*-2.14286;
h1=plot(newposx,aby,'--k');hold on;h2=plot(newnegx,aby,'--k');hold off;
set([h1 h2], 'LineWidth', 2)
title('Head on First and Fifteenth Slices')
ax = gca;
set(ax, 'XTick', [-7.5,-6,-4.5,-3,-1.5,0,1.5,3,4.5,6,7.5])
set(ax, 'YTick', [-5.5,-3.5,-1.5,0,1.5,3.5,5.5])

```

```

figure(2)
contourf(abx,aby,xy(:,:,2)');colorbar;hold on;
newposx=ones(1,15)*4.28571;newnegx=ones(1,15)*-4.28571;
h1=plot(newposx,aby,'--k');hold on;h2=plot(newnegx,aby,'--k');hold off;
set([h1 h2],'LineWidth',2)
title('Head on Second and Fourteenth Slices')
ax = gca;
set(ax,'XTick',[-7.5,-6,-4.5,-3,-1.5,0,1.5,3,4.5,6,7.5])
set(ax,'YTick',[-5.5,-3.5,-1.5,0,1.5,3.5,5.5])

```

```

figure(3)
contourf(abx,aby,xy(:,:,3)');colorbar;hold on;
newposx=ones(1,15)*5.35714;newnegx=ones(1,15)*-5.35714;
h1=plot(newposx,aby,'--k');hold on;h2=plot(newnegx,aby,'--k');hold off;
set([h1 h2],'LineWidth',2)
title('Head on Third and Thirteenth Slices')
ax = gca;
set(ax,'XTick',[-7.5,-6,-4.5,-3,-1.5,0,1.5,3,4.5,6,7.5])
set(ax,'YTick',[-5.5,-3.5,-1.5,0,1.5,3.5,5.5])

```

```

figure(4)
contourf(abx,aby,xy(:,:,4)');colorbar;hold on;
newposx=ones(1,15)*6.42857;newnegx=ones(1,15)*-6.42857;
h1=plot(newposx,aby,'--k');hold on;h2=plot(newnegx,aby,'--k');hold off;
set([h1 h2],'LineWidth',2)
title('Head on Fourth and Twelfth Slices')
ax = gca;
set(ax,'XTick',[-7.5,-6,-4.5,-3,-1.5,0,1.5,3,4.5,6,7.5])
set(ax,'YTick',[-5.5,-3.5,-1.5,0,1.5,3.5,5.5])

```

```

figure(5)
contourf(abx,aby,xy(:,:,5)');colorbar;hold on;
newposx=ones(1,15)*6.42857;newnegx=ones(1,15)*-6.42857;
h1=plot(newposx,aby,'--k');hold on;h2=plot(newnegx,aby,'--k');hold off;
set([h1 h2],'LineWidth',2)
title('Head on Fifth and Eleventh Slices')
ax = gca;
set(ax,'XTick',[-7.5,-6,-4.5,-3,-1.5,0,1.5,3,4.5,6,7.5])
set(ax,'YTick',[-5.5,-3.5,-1.5,0,1.5,3.5,5.5])

```

```

figure(6)
contourf(abx,aby,xy(:,:,6)');colorbar;
title('Head on Sixth and Tenth Slices')
ax = gca;
set(ax,'XTick',[-7.5,-6,-4.5,-3,-1.5,0,1.5,3,4.5,6,7.5])
set(ax,'YTick',[-5.5,-3.5,-1.5,0,1.5,3.5,5.5])

```

```

figure(7)
contourf(abx,aby,xy(:,:,7)');colorbar;
title('Head on Seventh and Ninth Slices')
ax = gca;

```

```
set(ax, 'XTick', [-7.5, -6, -4.5, -3, -1.5, 0, 1.5, 3, 4.5, 6, 7.5])
set(ax, 'YTick', [-5.5, -3.5, -1.5, 0, 1.5, 3.5, 5.5])
```

```
figure(8)
contourf(abx, aby, xy(:, :, 8)'); colorbar;
title('Head on Eighth Slices')
ax = gca;
set(ax, 'XTick', [-7.5, -6, -4.5, -3, -1.5, 0, 1.5, 3, 4.5, 6, 7.5])
set(ax, 'YTick', [-5.5, -3.5, -1.5, 0, 1.5, 3.5, 5.5])
```

```
% vector plot
```

```
vx=zeros(n,p,m); %velocity x component in 3d
for mmm=1:m
    jjj=1;
    for jj=1:p
        iii=1;
        for ii=(jj-1)*L+1+(mmm-1)*m:(jj-1)*L+n+(mmm-1)*m
            vx(iii, jjj, mmm)=vex(ii);
            iii=iii+1;
        end
        jjj=jjj+1;
    end
end
```

```
vy=zeros(n,p,m); %velocity y component in 3d
for mmm=1:m
    jjj=1;
    for jj=1:p
        iii=1;
        for ii=(jj-1)*L+1+(mmm-1)*m:(jj-1)*L+n+(mmm-1)*m
            vy(iii, jjj, mmm)=vey(ii);
            iii=iii+1;
        end
        jjj=jjj+1;
    end
end
```

```
figure(9)
quiver(abx, aby, vx(:, :, 7), vy(:, :, 7))
title('Velocity vectors on eighth slice')
xlim([-8 7]); ylim([-5.5 5.5]);
figure(10)
quiver(abx, aby, vx(:, :, 7), vy(:, :, 7))
xlim([-8 7]); ylim([-5.5 5.5]);
figure(11)
quiver(abx, aby, vx(:, :, 6), vy(:, :, 6))
xlim([-8 7]); ylim([-5.5 5.5]);
figure(12)
quiver(abx, aby, vx(:, :, 5), vy(:, :, 5))
figure(13)
quiver(abx, aby, vx(:, :, 4), vy(:, :, 4))
figure(14)
quiver(abx, aby, vx(:, :, 3), vy(:, :, 3))
figure(15)
```

```

quiver(abx, aby, vx(:, :, 2), vy(:, :, 2))
figure(16)
quiver(abx, aby, vx(:, :, 1), vy(:, :, 1))

% For permeability
for mmm=1:m
    jjj=1;
    for jj=1:p
        iii=1;
        for ii=(jj-1)*L+1+(mmm-1)*m:(jj-1)*L+n+(mmm-1)*m
            khd(iii, jjj, mmm)=(kp(2, 2, ii)-kcp(2, 2)); %/kcp(2, 2)-7.925e-5;
            iii=iii+1;
        end
        jjj=jjj+1;
    end
end
khd=khd(:, :, 7)/max(max(khd(:, :, 7)));
figure(1)
contourf(abx, aby, khd', 12); colorbar; hold on;
newposx=ones(1, 15)*6.42857; newnegx=ones(1, 15)*-6.42857;
h1=plot(newposx, aby, '--k'); hold on; h2=plot(newnegx, aby, '--k'); hold off;
set([h1 h2], 'LineWidth', 2)
title('Contour of Kyy on the Seventh Slice')
ax = gca;
set(ax, 'XTick', [-7.5, -6, -4.5, -3, -1.5, 0, 1.5, 3, 4.5, 6, 7.5])
set(ax, 'YTick', [-5.5, -3.5, -1.5, 0, 1.5, 3.5, 5.5])

%For power plot
for mmm=1:m
    jjj=1;
    for jj=1:p
        iii=1;
        for ii=(jj-1)*L+1+(mmm-1)*m:(jj-1)*L+n+(mmm-1)*m

powdxii(iii, jjj, mmm)=powdx(ii)*anex+powdy(ii)*aney+powdz(ii)*anez;
            iii=iii+1;
        end
        jjj=jjj+1;
    end
end
powdxii=powdxii(:, :, 7)/max(max(powdxii(:, :, 7)));
figure(2)
contourf(abx, aby, powdxii', 12); colorbar; hold on;
% newposx=ones(1, 15)*6.42857; newnegx=ones(1, 15)*-6.42857;
% h1=plot(newposx, aby, '--k'); hold on; h2=plot(newnegx, aby, '--k'); hold
off;
% set([h1 h2], 'LineWidth', 2)
title('Contour of Power on the Seventh Slice')
ax = gca;
set(ax, 'XTick', [-7.5, -6, -4.5, -3, -1.5, 0, 1.5, 3, 4.5, 6, 7.5])
set(ax, 'YTick', [-5.5, -3.5, -1.5, 0, 1.5, 3.5, 5.5])

abex=linspace(-7.5, 7.5, 15);
abey=linspace(-5.5, 5.5, 14);

```

```
%for velocity on the eighth slice
figure(3)
vy7=vy(:,1:14,7)/max(max(vy(:,1:14,7)));
contourf(abex,abey,vy7',12);colorbar;hold on;
% newposx=ones(1,15)*6.42857;newnegx=ones(1,15)*-6.42857;
% h1=plot(newposx,aby,'--k');hold on;h2=plot(newnegx,aby,'--k');hold
off;
% set([h1 h2],'LineWidth',2)
title('Contour of Velocity on the Seventh Slice')
ax = gca;
set(ax, 'XTick', [-7.5,-6,-4.5,-3,-1.5,0,1.5,3,4.5,6,7.5])
set(ax, 'YTick', [-5.5,-3.5,-1.5,0,1.5,3.5,5.5])
```